Title
Radiation Transport Modeling of Kilonovae and Broad-lined Ic Supernovae

Author
Barnes, Jennifer Lynn

Publication Date
2017

Radiation Transport Modeling of Kilonovae and Broad-lined Ic Supernovae

by

Jennifer Barnes

A dissertation submitted in partial satisfaction of the

requirements for the degree of

Doctor of Philosophy

in

Physics

in the

Graduate Division

of the

University of California, Berkeley

Committee in charge:

Associate Professor Daniel Kasen, Chair
Professor Eliot Quataert
Professor Joshua Bloom

Summer 2017

Radiation Transport Modeling of Kilonovae and Broad-lined Ic Supernovae

Abstract

Radiation Transport Modeling of Kilonovae and Broad-lined Ic Supernovae

by

Jennifer Barnes

Doctor of Philosophy in Physics

University of California, Berkeley

Associate Professor Daniel Kasen, Chair

This thesis presents models of the radiative signatures of two unusual electromagnetic transients: radioactive transients ("kilonovae") associated with the merger of a neutron star with a second neutron star or a black hole, and broad-lined Type Ic supernovae. The first portion of the thesis focuses on improving inputs for radiation transport simulations of kilonovae. I first address opacity. I present new calculations of the opacities of elements synthesized in the kilonova ejecta, and carry out radiation transport simulations of kilonovae using these new opacities. Next, I develop detailed models of the radioactive heating of the kilonova ejecta and explore its effects on kilonova light curves. These two projects advanced our understanding of the expected emission from kilonovae, and will inform efforts to find and analyze these elusive transients. The final part of this thesis considers broad-lined Type Ic supernovae. I use multidimensional hydrodynamics and radiation transport simulations to investigate the validity of the single-engine model for broad-lined superonva Ic/gamma-ray burst systems. I demonstrate that a jet engine injected into a stripped-envelope progenitor star can produce both a supernova with broad spectral features and a long-duration gamma-ray burst.

I dedicate this dissertation to my parents.

Contents

Acknowledgments **iv**

1 Introduction **1**
- 1.1 Compact object mergers and their electromagnetic counterparts 2
  - 1.1.1 Modeling kilonovae 4
- 1.2 Broad-lined Type Ic supernovae 6
- 1.3 Monte Carlo radiation transport in expanding atmospheres 7
- 1.4 Thesis outline 10

2 Effect of a high opacity on the light curves of radioactively-powered transients from compact object mergers **11**
- 2.1 Introduction 12
- 2.2 Opacity of r-process ejecta 13
- 2.3 Light curves of r-process transients 16
  - 2.3.1 Ejecta Model 16
  - 2.3.2 Light Curves 18
  - 2.3.3 Uncertainties in the Opacities 24
  - 2.3.4 A ^{56}Ni-powered transient 25
- 2.4 Conclusion 28

3 Radioactivity and thermalization in the ejecta of compact object mergers and their impact on kilonova light curves **31**
- 3.1 Introduction 32
- 3.2 Properties of the kilonova ejecta 33
  - 3.2.1 Ejecta model 33
  - 3.2.2 Magnetic fields 34
  - 3.2.3 Composition 35
  - 3.2.4 Radioactivity 36
  - 3.2.5 Emission Spectra of Decay Products 38
- 3.3 Thermalization Physics 43
  - 3.3.1 Gamma-rays 43
  - 3.3.2 Beta particles 44

- 3.3.3 Alpha-particles . . . 46
- 3.3.4 Fission fragments . . . 48
- 3.4 Analytic Results . . . 49
  - 3.4.1 Analytic estimates of thermalization timescales . . . 49
  - 3.4.2 Summary of thermalization timescales . . . 52
  - 3.4.3 Analytic thermalization model . . . 52
- 3.5 Numerical Results . . . 54
  - 3.5.1 Thermalization efficiencies . . . 54
  - 3.5.2 Total heating efficiency . . . 57
- 3.6 Effect on Kilonova Light curves . . . 62
  - 3.6.1 Analytic fit to thermalization efficiency . . . 64
  - 3.6.2 Light curves . . . 65
  - 3.6.3 Implications for the kilonova accompanying GRB 130603B . . . 66
  - 3.6.4 Late-time light curve . . . 69
- 3.7 Conclusion . . . 71

4 A GRB and Broad-lined Type Ic Supernova from a Single Central Engine 74

- 4.1 Introduction . . . 74
- 4.2 Numerical Methods . . . 77
- 4.3 Progenitor and Engine Models . . . 79
- 4.4 Gas Dynamics . . . 81
- 4.5 Supernova Observables . . . 85
  - 4.5.1 Bolometric Light Curves . . . 85
  - 4.5.2 Spectra . . . 87
- 4.6 Discussion and Conclusion . . . 92

Bibliography 94

A Transport Methods for Radioactive Decay Products 100

- A.1 Grid . . . 100
- A.2 Gamma rays . . . 100
- A.3 Massive particles . . . 101
  - A.3.1 Influence of magnetic fields . . . 102
  - A.3.2 Fission fragment transport . . . 103

Acknowledgments

Like all dissertations, mine has been a collaborative effort, and I recognize with gratitude the contributions of the many people who have helped me along the way.

Much credit is due to my advisor, Dan Kasen, whose guidance and mentorship I have relied on for the past six years. I am also indebted to my groupmates, Nathan Roth and János Botyánszki, who I consider friends as well as colleagues.

I have been fortunate to have dedicated and insightful collaborators. I feel especially lucky to have worked with Paul Duffel, who taught me everything I know about computational hydrodynamics, and Samaya Nissanke, whose support and encouragement have been unwavering and invaluable.

I am grateful to my parents, Jay and Karen, my sisters, Kelly and Lisa, and my partner Patrick; their faith in me reminded me to have faith in myself.

Lastly, I am thankful for friends both inside and outside the department whose company made the last seven years more joyful and whose support made the Ph.D. grind less daunting.

This dissertation was typeset using the ucastrothesis LaTeX template.

Chapter 1

Introduction

The answers to several open questions in astrophysics research lie in understanding stellar life-cycles, in particular stellar deaths. Violent stellar deaths like supernova explosions and stellar mergers are some of the most energetic events in the Universe, and are thought to be the furnaces where the heaviest elements are forged. In their demise, stars can also form ultra-dense neutron stars or black holes. In certain cases—core collapse supernovae and compact object mergers—stellar destruction may produce gravitational radiation: ripples in the fabric of spacetime that have only recently been observed. The study of explosive systems is a means for understanding physics in the extreme energy, gravity, temperature, and velocity regimes that apply to these systems.

Detailed and accurate models of explosive astrophysical transients are essential for understanding the explosions themselves, their progenitor systems, and the physical processes at play in their evolution. Radiation transport calculations are an important component of modeling efforts because they serve as a bridge between theory and observation, allowing astronomers to link particular observational fingerprints to the underlying physical features or processes that produce them, and therefore to test explosion and progenitor models.

My thesis research focuses on two types of astrophysical explosions: radioactive transients associated with compact object (CO) mergers, and broad-lined Ic supernovae (SNe Ic-BL). These two types of transients are, in some ways, distinct. The former accompany the deaths of young, massive stars; the latter are triggered by the coalescence of two stellar corpses that have spent hundreds of millions or billions of years circling each other in a stellar danse macabre. Broad-lined Ic supernova have a composition similar to other explosive systems; in contrast, merger-driven explosions are expected to synthesize and draw their power from an exotic cocktail of heavy, radioactive nuclei. And while SNe Ic-BL are relatively bright and long-lived, transients from mergers are believed to be short and dim. (Another difference: transients from mergers have not been definitely identified, while observers have identified a sizable catalog of SNe Ic-BL.)

However, there are also similarities. Both explosions are associated with gamma-ray bursts, whether short, in the case of CO mergers, or long, as for SNe Ic-BL. Both are impacted by the physics of compact objects: SNe Ic-BL because they produce them, and

CO mergers because they violently disrupt them. Each event is also a claimed formation channel for magnetars. Fundamentally, they are both non-standard explosions with masses or energies than set them apart from their better-sampled, more uniform cousins (e.g. SNe Ia, or classical novae). Modeling these two transients, which seemingly represent opposite extrema in the distribution of explosive transient properties, is important for understanding the full range of physical processes that give rise to astrophysical explosions.

1.1 Compact object mergers and their electromagnetic counterparts

It has long been known that most massive stars in the Universe spend their main sequence lifetimes in binary pairs. However, whether these stellar binaries could evolve out of the main sequence together and become CO binaries—binaries in which each component is either a neutron star (NS) or a black hole (BH)—remained an open question until the discovery in 1975 of the Hulse-Taylor pulsar (Hulse & Taylor 1975). An analysis of systematic variations in the timing of the bursts of electromagnetic energy emanating from the pulsar revealed it to be in orbit around a second body, which was later determined to be a NS. This was the first such system ever detected.

Further monitoring of the Hulse-Taylor pulsar (Weisberg & Taylor 1981, 2005) revealed that its orbit was shrinking. The orbital evolution was found to conform with extremely high precision (Taylor et al. 1992) to the theory of general relativity (GR), which predicts that a system emits gravitational radiation in response to the acceleration of its quadrupole moment. Gravitational waves carry away energy and angular momentum, causing a binary's orbital period and separation to decrease (Peters & Mathews 1963).

The discovery of the Hulse-Taylor Pulsar was a major advance on two fronts. The near-perfect agreement between the prediction of general relativity and the observed orbital decay was strong evidence in favor of GR's theory of gravitational radiation, and served as a first, indirect detection of gravitational waves. Moreover, the mere existence of the Hulse-Taylor Pulsar hinted at the possibility of *directly* detecting gravitational waves with ground-based interferometers.

Gravitational wave signals from mergers will be strongest, and thus easiest to detect, in the moments just before the binary coalesces, when the orbital separation is small and the velocities of the component stars approach the speed of light. However, such signals will only be produced if two conditions are met. First, massive star binaries must survive the supernova explosions of their component stars without becoming gravitationally unbound. Second, the post-supernovae binaries must have an orbital separation small enough that they will merge on timescales less than a Hubble time.

The Hulse-Taylor Pulsar provided conclusive evidence that at least some stellar binaries live on as small-orbit compact object binaries. A handful of additional binaries have been discovered since; there are now four double NS systems in the galactic plane with merger times less than the Hubble time (Kim et al. 2015). These discoveries helped motivate the construction of large-scale gravitational wave interferometers that aimed to directly detect gravitational waves from coalescing compact object binaries.

Multiple observations of mergers of various binary types would yield a deeper understanding of how stars interact with their binary companions over the course of their lifetimes, and provide important observational constraints for population synthesis models. A NSNS or NSBH observation would also be an opportunity to study merger-associated events unique to systems containing a NS. Binary black hole mergers are pure, general relativistic events. The merger of a NS with a NS or BH brings matter into the picture; a NS may be disrupted during inspiral and merger, and the disrupted material can drive a host of astrophysical phenomena, each with a corresponding electromagnetic (EM) signal. Immediately after the merger, a short-lived ultra-relativistic jet may be launched; its radiation would manifest as short-duration gamma-ray burst (GRB; Paczynski 1986; Eichler et al. 1989a; Narayan et al. 1992). Much later (months or years after the merger), the collision of unbound material with the interstellar medium should produce a radio signal (Nakar & Piran 2011; Hotokezaka & Piran 2015) . On intermediate timescales, the decay of unstable elements synthesized in the material torn off component NSs as the system merges could power a transient that would shine at optical or infrared wavelengths (Li & Paczyński 1998; Metzger et al. 2010; Roberts et al. 2011).

Any EM counterpart detected in concert with a GW signal would give us a much fuller picture of the merger and its aftermath than GWs alone. For example, measurements of the mass ejected from the system, via optical or radio signals, could be combined with measurements of the component star masses from the gravitational waveform to constrain the NS equation of state (Pannarale & Ohme 2014). An EM signal would also allow a much more precise localization of the merger than the gravitational wave signal—especially in the early days of two or three GW detectors (Kasliwal & Nissanke 2014); if an EM counterpart identified the merger's host galaxy, the host's redshift could be combined with the luminosity distance obtained from gravitational waves to yield a new measurement of the Hubble Constant (Nissanke et al. 2013a). Perhaps most intriguingly, a radioactively-powered transient could allow us to directly observe the formation site of some of the heaviest elements in the Universe, and constrain their origin.

Rapid neutron capture (r-process) nucleosynthesis is responsible for forging roughly half of the elements heavier than Fe. Over the course of the r-process, seed nuclei capture free neutrons at a rate so high there is insufficient time to undergo β-decay between captures. Once the free neutron reservoir has been depleted, the nuclei, which by this point populate a heavy, neutron-rich region of the periodic table far from the valley of stability, begin to decay, releasing radioactive energy as they settle into their final, stable abundance pattern.

Because a high free neutron flux is required, the astrophysical site of r-production has long been debated. Core-collapse supernovae were proposed on the theory that neutrino-driven winds blown off the proto-neutron star created by the collapse would be sufficiently neutron-rich to host an r-process (Meyer et al. 1992; Woosley et al. 1994). Lattimer & Schramm (1974) suggested NSNS/NSBH mergers as sources of the r-process; the dynamical shredding of the NS that occurs during a merger naturally produces the high neutron flux and lowentropy conditions required for a successful r-process (see also Lattimer & Schramm 1976; Eichler et al. 1989b; Freiburghaus et al. 1999; Korobkin et al. 2012). Observing radioactive transients following NSNS or NSBH mergers could confirm mergers as an astrophysical site of the r-process, and constrain the amount of r-process-rich material ejected in a typical merger. This information, along with improved rate estimates from GW surveys, would reveal whether CO mergers are sufficient to explain the entirety of the r-process content of the Universe, or whether additional formation channels must be invoked.

The chance to constrain the formation of the heavy elements is strong theoretical motivation for seeking out radioactive transients accompanying to CO mergers. However, practical considerations supply additional incentives (Metzger & Berger 2012). Unlike short GRBs, whose emission is highly beamed, radioactive transients will shine more or less isotropically. They will also rise to peak on timescales favorable for EM follow-up: days to weeks versus months or years for a radio afterglow. This makes radioactive transients compelling EM counterparts. Seeking them out and rigorously analyzing their radiative signatures will vital for fulfilling the goals of multi-messenger astronomy.

1.1.1 Modeling kilonovae

Successfully detecting radioactive transients (henceforth referred to as “kilonovae”) and interpreting their signals requires the construction of detailed and accurate models of their emission; given the large LIGO error-boxes and the many contaminants in the transient sky, defining the expected character of the EM signatures will be crucial for kilonova detection efforts, whether blind or following a LIGO trigger.

Li & Paczyński (1998) were the first to study the electromagnetic emission from an r-process-powered transient. Lacking detailed models of the relevant masses, energetics, and radioactive decay, they based their predictions on parametrized, analytic, one-dimensional models. (Impressively, the simple but elegant arguments used to analytically derive the rate at which r-process decay releases energy yielded a prediction not far from that found years later by sophisticated nuclear network calculations.) Their work suggested that an r-process “mini-supernova” would be a short, bright, optical transient. Since then, models of the expected radiation have improved. This has required a coordinated efforts over multiple subfields of physics, because kilonovae’s ultimate radiative signatures depend on several factors that are governed by a wide array of physical processes.

To first order, a transient’s photometry can be described by the time it takes to rise to peak, $t_{\rm pk}$, and its peak luminosity, $L_{\rm pk}$. Rough scalings for these quantities are given by Arnett’s Law (Arnett 1982),

$$t_{\rm pk} \sim \left(\frac{M_{\rm ej}\kappa}{v_{\rm ej}c}\right)^{1/2} \tag{1.1}$$

$$L_{\rm pk} \sim \dot{E}_{\rm rad}(t_{\rm pk}), \tag{1.2}$$

where $M_{\rm ej}$ and $v_{\rm ej}$ are the mass and characteristic velocity of the ejected material, κ is its opacity, c is the speed of light, and $\dot{E}_{\rm rad}$ is the time-dependent rate of energy generation by radioactive decay. Though simple, these two equations identify the essential ingredients for predicting the properties of a transient's emission.

The ejected mass and the velocity of the outflow determine the ease with which radiation diffuses through the ejecta. Because CO mergers are expected to produce ejecta composed entirely of r-processed, unstable nuclei, the mass ejected will also set the radioactive energy scales for the system ($\dot{E}_{\rm rad} \propto M_{\rm ej}$). The mass and velocity will depend on the binary type (NSNS v. NSBH) and mass ratio (Oechslin et al. 2007; Sekiguchi et al. 2016; Kyutoku et al. 2015). Defining a reasonable range of expected masses therefore requires understanding what a typical binary looks like, which in turn requires a detailed knowledge of stellar binary evolution. The dynamics of mass ejection are also extremely complicated: the entire process plays out in a strong gravity regime in which, since NSs are highly magnetized, magnetic fields are likely to be dynamically important (Price & Rosswog 2006). General relativistic magnetohydrodynamics simulations are needed to fully capture the physics of inspiral, merger, and mass ejection. An additional unknown is the NS equation of state, which controls how easily a merging NS can be tidally shredded, or disrupted upon impact (e.g. Bauswein et al. 2013; Hotokezaka et al. 2013a).

Kilonovae's radioactive power source adds an additional uncertainty. Unlike Type Ia supernovae, which are powered predominantly by a single decay chain, kilonova draw their power from the decays of the large and diverse ensemble of elements produced by the r-process. Each decay chain proceeds on its own timescale and is characterized by a unique energy spectrum. The precise half lives, branching ratios, and decay spectra are often unknown, because the r-process synthesizes exotic nuclei, and experimental data for these neutron-rich species is limited.

The nuclear mass models used to describe these unmeasured nuclei predict both their neutron capture cross-sections and the properties of their radioactive decay; the choice of nuclear mass model thus influences the distribution of heavy nuclei synthesized when the free neutron flux is high, and the properties of the subsequent radioactive decays. Nuclear mass models are calibrated to measured nuclei in or near the valley of stability, but can diverge substantially in their predictions of the behavior of heavy, neutron-rich nuclei produced by the r-process, making the final r-process abundance pattern sensitive to the choice of mass model (Eichler et al. 2015; Mendoza-Temis et al. 2015).

The abundance pattern of r-processed material, and thus the radioactivity, also depend on initial conditions, namely the neutron-richness at the onset of the r-process. The more neutron rich the initial composition is, the more easily the r-process can assemble heavy elements and the more prominent the third r-peak will be in the final abundance distribution. In contrast, a less neutron-rich mixture will choke the r-process limiting the production of third-peak nuclei and restricting the final abundance yields to lighter nuclei (Lippuner & Roberts 2015).

A final challenge is modeling the propagation of radiation within the kilonova. The predictions of radiation transport simulations depend on the (ideally three-dimensional) density profile of the ejecta, as well as the radioactivity. Radiation transport simulations thus inherit all of the uncertainties of the hydrodynamical and nuclear calculations described above.

Radiation transport must also contend with one additional unknown: the cross-sections—most commonly formulated in terms of opacity κ ($[\kappa] = \mathrm{cm\ g}^{-1}$)—for the interactions of photons with the heavy ions created in the r-process. The wavelength-dependent opacities of the r-process composition have a strong effect on the light curves and colors of the resulting transient. Understanding the opacities is therefore vital for the construction of reliable kilonova models. This will be addressed in a fair amount of detail in subsequent chapters.

1.2 Broad-lined Type Ic supernovae

Broad-lined Ic supernovae are a subset of core-collapse supernovae (CCSNe) unusual in the breadth of the emission and absorption features in their spectra. The extreme Doppler broadening evident in the spectra of SNe Ic-BL imply photospheric velocities of $\sim 0.1c$, and kinetic energies ($\sim 10^{52}$ ergs) much higher that what is inferred for typical CCSNe. SNe Ic-BL are also linked to long-duration GRBs; since SN 1998bw was detected emerging from the afterglow of GRB 980425B (Galama et al. 1998), every supernova linked to a GRB has been classified as Type Ic-BL (Woosley & Bloom 2006; Modjaz 2011).

These properties introduce two important questions about SNe Ic-BL. First, what is the relationship between GRBs and SNe Ic-BL? While all GRB-SNe are Type Ic-BL, the inverse is not true. The existence of SNe Ic-BL without an observed coincident GRB can in part be explained by viewing angle effects: an observer located far off the jet axis would not see the gamma-rays from the GRB. However, such an observer could infer the presence of highly relativistic material by detecting more isotropic, late-time radio signals produced by jet as it decelerates and spreads, becoming visible along new lines of sight. Radio follow-up of at least some GRB-absent SNe Ic-BL have failed to detect such signals (Berger et al. 2002; Soderberg et al. 2006b; Corsi et al. 2016), evidence that GRBs are not a universal feature of energetic supernovae.

The second question is the nature of the central engine capable of driving such energetic explosions. The similarity of the inferred kinetic energies of SNe Ic-BL to the maximum kinetic energy of a rotating neutron star led Mazzali et al. (2014) to propose that SNe Ic-BL draw their energy from rapidly spinning magnetars. (A theoretical argument explaining the means by which a magnetar's rotational energy could be extracted and used to power a supernova was provided by Thompson et al. 2004.) Others (MacFadyen & Woosley 1999) have suggested that the supernova ejecta is unbound from an accretion disk surrounding the central black hole created by collapse of the stellar progenitor (the "collapsar" scenario.) A third argument holds that the SN is launched by the same jet engine that produces the GRB (Maeda & Nomoto 2003). Recent studies (Sobacchi et al. 2017b; Piran et al. 2017) have advocated an extreme version of this theory, claiming that jets—or at least jet engines–operate in *all* Type Ibc supernovae, but emerge from the stellar envelope as GRBs only for certain combinations of jet and progenitor properties.

The problem of the central engine behind SNe Ic-BL is complicated by the question of how reliably we are able to infer the kinetic energies of these supernovae from observations.

Kinetic energies are generally estimated by comparing observed light curves and spectra to parametrized, one-dimensional models. These models may be poorly calibrated if the ejecta of SNe Ic-BL are significantly aspherical. The fact that SNe Ic-BL with coincident GRB have broader features than those without (Modjaz et al. 2016) may point to systemic asymmetries in the structure of the ejecta; if the ejecta is prolate, for example, the photosphere may have a higher velocity near the pole (i.e., the jet axis) than near the equator, which would cause spectral features to appear broader to observers on the pole, who would also see the GRB. The ability to produce explosions with kinetic energies of $\sim 10^{52}$ ergs has traditionally been the primary criterion for assessing Ic-BL engines. If spherical symmetry is a poor approximation, this will have implications for the viability of various central engine models.

The possibility that SNe Ic-BL explosions are significantly anisotropic has been discussed extensively in the literature (Tanaka et al. 2007; Maeda et al. 2006). It has been invoked in the interest of recalibrating the inferred parameters of seemingly extreme supernovae, like SN 1998bw (Höflich et al. 1999), or resolving the apparent contradiction between many SNe Ic-BL's rapid rises and sustained late-time luminosity (Dessart et al. 2017). (The former requires radioactive ^{56}Ni to lie at high velocities, while the the later implies a high-density, low-velocity region rich in ^{56}Ni; it is difficult to satisfy both these constraints with a one-dimensional model; see e.g. Maeda et al. 2003.)

To make progress on the questions surrounding SNe Ic-BL, it is necessary to develop multidimensional models of various engines, the explosions they induce, and the nature of the radiation emitted by these explosions. Ideally, these models will be calculated using fully relativistic hydrodynamics, in order to better capture the physics underlying the formation and propagation of the relativistic GRB jet, and the effect of the jet on other components of the outflow. Relativistic, multi-dimensional models may enable a keener understanding of the degree of anisotropy that characterizes the ejecta and the effect of that anisotropy on the resultant light curves and spectra. It may also lead to the development of more accurate methods for diagnosing supernova parameters from observational data. Ultimately, such calculations will form part of a toolkit that will allow astronomers to more accurately evaluate competing central engine theories, and give us insight into what drives these (apparently) hyperenergetic explosions.

1.3 Monte Carlo radiation transport in expanding atmospheres

Much of the research contained in this thesis uses Monte Carlo (MC) radiation transport (RT) calculations to study the light curves and spectra generated by various electromagnetic transients. A brief description of the methods employed and the relevant physics is presented here. The discussion of radiation transport generally draws from the classic textbook of Rybicki & Lightman (1986), while the description of MC methods, and the particulars of solving the RT equations in expanding atmospheres, adhere closely to Kasen et al. (2006).

The goal of radiation transport is to calculate the monochromatic specific intensity I_ν for a particular system. The specific intensity varies with position, direction, and wavelength, and is related to the luminosity by

$$L = \frac{\mathrm{d}E_{\mathrm{rad}}}{\mathrm{d}t} = \iiint I_\nu \, \mathrm{d}\nu \, \mathrm{d}A \, \mathrm{d}\Omega, \tag{1.3}$$

where frequency ν runs over the electromagnetic spectrum, A is area, and Ω is solid angle.

RT calculations determine I_ν by integrating the transport equation,

$$\frac{\mathrm{d}I_\nu}{\mathrm{d}s} = -\alpha_\nu I_\nu + j_\nu. \tag{1.4}$$

Above, s measures distance, and α_ν and j_ν are the monochromatic extinction and emission coefficients. The extinction coefficient (units cm^{-1}) specifies the amount of radiation lost to scattering and absorption as a function of the distance a photon travels. It is related to other common variables quantifying extinction via

$$\alpha_\nu = n\sigma_\nu = \rho\kappa_\nu, \tag{1.5}$$

where σ_ν is the cross-section for a particular interaction, n is the number density of scatterers or absorbers for that interaction, κ is the monochromatic opacity, and ρ is mass density. Common sources of opacity for optical photons in supernovae and similar systems are electron scattering, bound-free opacity (photoionization), and bound-bound or "line" opacity (photoexcitation).

The emission coefficient, j_ν, represents the addition of radiation energy (per time per volume per frequency per solid angle) to I_ν. For a system in thermal equilibrium, emission balances absorption to preserve the local temperature T, in which case the emission coefficient is related to the Planck function B_ν by $j_\nu = \alpha_{\nu,\mathrm{abs}} B_\nu(T)$, where $\alpha_{\nu,\mathrm{abs}}$ is the absorptive component of the opacity

SEDONA, which I have used in service of my dissertation research, is a time-dependent, Monte Carlo radiation transport code that assumes local thermodynamic equilibrium and employs the expansion opacity formalism to treat photon propagation in an expanding medium. The details of its implementation are described fully in Kasen et al. (2006).

Monte Carlo methods solve the transfer equation by diffusing discrete photon "packets" through a medium. The probabilities for various outcomes associated with the transport are calculated, and random number sampling is employed to select among these outcomes. Sampling is used to determine, for example, the outcome of a photon-ion interaction, the direction into which a Compton-scattering gamma-ray reorients, and the wavelength at which an absorbed photon is re-emitted.

Most fundamentally, random sampling is used to determine the size of the steps packets take as they advance through the medium. A particular photon packet can only be absorbed or scattered, so the relevant description is Equation 1.4 with j_ν set to 0, which has a simple solution,

$$\frac{\mathrm{d}I_\nu}{\mathrm{d}s} = -\alpha_\nu I_\nu \longrightarrow I_\nu(s) = I_{\nu,0} \exp[-\alpha_\nu s]. \tag{1.6}$$

In MC, Equation 1.6 must be reinterpreted probabilistically. Unlike a beam whose intensity can be incremented or decremented by arbitrarily small amounts, MC photon packets are discrete; they either undergo an interaction, or they survive unchanged. The ratio $I(s_1)/I(s_2)$ represents not the fraction of energy lost from a beam of radiation, but the probability that photon originating at s_1 will interact at some position $s_1 < s \leq s_2$. In MC transport, this probability is randomly selected from the interval $(0, 1]$, and Equation 1.6 is inverted to determine the corresponding distance. The randomly selected value z then corresponds to a step size of

$$\Delta s = -\frac{1}{\alpha_\nu} \log z. \tag{1.7}$$

Calculating opacity is clearly vital for accurately solving the transport equation. However, the question of opacity becomes more complicated in the expanding atmospheres of explosive systems. This is because opacity is wavelength-dependent, and the wavelength of the photon depends on the local fluid velocity. For homologous expansion ($v_{\text{fluid}} = r/t$; an appropriate assumption for supernovae and kilonovae on timescales relevant for RT) a photon's energy, as measured in the co-moving frame, will continually decrease as it moves through the fluid, and the opacity it experiences will change.

This is particularly important for the calculation of bound-bound opacities. A photon can only excite a bound-bound transition if it has an energy approximately equal to the energy difference between the initial and final bound atomic states. A Doppler-shifting photon will move into and out of resonance with lines as it slips ever-redward, which must be accounted for when tabulating bound-bound opacity. The Sobolev/Expansion Opacity formalism was engineered to appropriately model this effect. The Sobolev approximation assumes that the resonance region for a given line is physically small. For homologous flows, the Sobolev optical depth (Sobolev 1960) in the resonance region is

$$\tau = \frac{K_\lambda c t_{\text{exp}}}{\lambda_0}, \tag{1.8}$$

where K_λ is the integrated line strength, t_{exp} is the expansion time, and λ_0 is the wavelength of line center. (In non-homologous systems, the Soblolev τ will depend on the velocity gradient in the direction of a photon's motion.)

An effective continuum opacity can then be defined using the expansion opacity procedure of Karp et al. (1977) (later reformulated by Eastman & Pinto 1993), which averages individual lines in bins in wavelength space,

$$\alpha_{\text{exp}}(\lambda_{\text{c}}) = \frac{1}{c t_{\text{exp}}} \sum_i \frac{\lambda_{\text{i}}}{\Delta \lambda_{\text{c}}} (1 - e^{-\tau_{\text{i}}}). \tag{1.9}$$

Here, λ_{c} is the wavelength of the center of the bin, τ_{i} is the Sobolev optical depth of line i, and the sum runs over all lines within the bin.

1.4 Thesis outline

The first two chapters of this thesis focus on kilonovae. In Chapter 2, I investigate the opacities of r-process elements. I argue that, due to the complexity of certain elements synthesized by the r-process, the material ejected in CO mergers will have opacities much higher than originally believed. I also present radiation transport calculations of kilonovae using the updated estimates of opacity, and find that including more realistic r-process opacities causes light curves to be broader and dimmer and colors to be redder than earlier models suggested. These results are a qualitative departure from previous work, which predicted that kilonovae would be short, fairly bright, optical transients.

In Chapter 3, I study the effect of radioactive heating on the kilonova light curves. Earlier kilonova calculations assumed that the suprathermal charged particles and gamma-rays emitted by r-process decay thermalize efficiently in the ejecta; the energy they transfer to the background gas would therefore be immediately available to supply luminosity and power the light curve. I calculate the heating cross-sections for the full range of radioactive particles created by r-process decay, and present the transport code I developed to propagate charged particles and gamma-rays through the ejecta. I use this code to explicitly determine the rate of heating. I find that heating becomes inefficient fairly early, which results in lower-luminosity kilonovae. I also explore how heating efficiency varies with different r-process models, and determine that nuclear mass models that predict significant amounts of α-decay heat the ejecta more efficiently, and produce higher luminosities for otherwise comparable kilonova models. This work thus identified a direct link between the details of the r-process and observable properties of r-process-powered transients.

In Chapter 4, I consider the engines broad-lined Type Ic supernovae. I present multidimensional hydrodynamics calculations showing that a single jet engine injected into a stripped-envelope star can produce two high-energy events: a narrow, highly relativistic GRB, and a more isotropic supernova explosion. The jet has an energy, Lorentz factor, and duration typical of long gamma-ray bursts, while the supernova acquires a kinetic energy comparable to those inferred for SNe Ic-BL. Radiation transport calculations reveal that the supernova spectrum has the broad emission and absorption features that define the Ic-BL category.

Chapter 2

Effect of a high opacity on the light curves of radioactively-powered transients from compact object mergers

The content of this chapter is drawn from Barnes & Kasen (2013), with permission from the co-author and the AAS.

The coalescence of compact objects are promising astrophysical sources of detectable gravitational wave signals. The ejection of r-process material from such mergers may lead to a radioactively-powered electromagnetic counterpart signal which, if discovered, would enhance the science returns of a gravitational wave detection. As very little is known about the optical properties of heavy r-process elements, previous light curve models have adopted opacities similar to those of iron group elements. Here we consider the effect of heavier elements, particularly the lanthanides, which increase the ejecta opacity by several orders of magnitude. We include these higher opacities in time dependent, multi-wavelength radiation transport calculations to predict the broadband light curves of one-dimensional models over a range of parameters (ejecta masses $\sim 10^{-3} - 10^{-1} M_{\odot}$ and velocities $\sim 0.1 - 0.3c$). We find that the higher opacities lead to much longer duration light curves which can last a week or more. The emission is shifted toward the infrared bands due to strong optical line blanketing, and the colors at later times are representative of a blackbody near the recombination temperature of the lanthanides ($T \sim 2500$ K). We further consider the case in which a second mass outflow, composed of ^{56}Ni, is ejected from a disk wind, and show that the net result is a distinctive two component spectral energy distribution, with a bright optical peak due to ^{56}Ni and an infrared peak due to r-process ejecta. We briefly consider the prospects for detection and identification of these transients.

2.1 Introduction

A deeper understanding of compact object binary mergers has the potential to shed light on several important and unresolved questions in astrophysics. Merging neutron star or neutron star-black hole binaries may be the engines of short-duration gamma ray bursts (Paczynski 1986; Narayan et al. 1992), and heavy element nucleosynthesis in merger ejecta decompressing from nuclear densities (Lattimer & Schramm 1974, 1976) may contribute to the production of r-process elements in the Universe (e.g. Eichler et al. 1989b; Rosswog et al. 1998; Freiburghaus et al. 1999; Rosswog et al. 2000; Rosswog 2005; Goriely et al. 2005). The gravitational wave (GW) interferometer LIGO has recently successfully detected the GW signatures of merging binary black holes (Abbott et al. 2016c,a), and the detection of a signal from a NSNS or NSBH binary is likely in the upcoming years. A merger involving at least one NS (henceforth referred to as a "neutron star merger" or NSM) should produce an electromagnetic (EM) signal, in addition to GWs. Identifying coincident EM counterparts would enhance the science returns from GW detections (e.g. Schutz 1986, 2002; Stubbs 2008; Bloom et al. 2009).

Metzger & Berger (2012) consider several possible EM transients associated with compact object mergers – short-duration gamma ray bursts, orphan radio and optical afterglows, and optical "kilonovae" light curves – and conclude that the last of these offers perhaps the best opportunity for localizing GW signals. The kilonovae are optical transients powered by the radioactive decay of material ejected in the merger. Simulations suggest that somewhere in the range of $10^{-4} - 10^{-1}\ M_\odot$ may be ejected either by tidal stripping during the merger itself, or later by a disk wind driven in the evolution of a post-merger remnant. The tidally ejected material is very neutron rich and should form heavy elements via the r-process, while the subsequent outflows could be less neutron rich, in which case nucleosynthesis may not extend much beyond the iron peak. In either case, the brightness of the resulting light curves will be set by the mass of radioisotopes ejected, while the duration depends on the effective diffusion time through the ejecta, and hence on mass, velocities, and opacities. While the nucleosynthesis and radioactive heating has been modeled with a fair degree of detail (Metzger et al. 2010; Roberts et al. 2011; Goriely et al. 2011), the unknown opacities of r-process elements remain a major challenge to predicting kilonova light curves and spectra.

Li & Paczyński (1998) were the first to study the r-process transients from NSM. Their simplified one-zone model assumed spherical symmetry and a blackbody spectrum, and absorbed much of the physical complexity of the system into a set of input parameters. Assuming opacities on the order of the electron scattering opacity, they predicted that the light curves would peak in the optical/ultraviolet and rise to peak bolometric luminosities of $10^{42} - 10^{44}$ ergs s^{-1} on a timescale of a day. More recent, more detailed, models (Metzger et al. 2010; Roberts et al. 2011) have used nuclear reaction networks to determine the radioactive heating rate and Monte Carlo radiation transport to calculate merger light curves, under the assumption that the opacities of heavy r-process elements could be approximated by those of iron. These newer models found qualitatively similar results, with peak bolometric luminosities $\sim 10^{41} - 10^{42.5}$ ergs s^{-1} and rise times around one day, with the colors rapidly reddening post-peak.

In this paper, we show that using more realistic opacities of r-process material has a dramatic effect on the predicted kilonova light curves. We use improved estimates of the atomic data and opacities of heavy elements derived from *ab initio* atomic structure models (Kasen et al. 2013, hereafter K13). The r-process opacities are orders of magnitudes higher than those of iron group elements; as a consequence, we predict light curves that are longer, dimmer, and redder than previously thought. Rather than peaking sharply at $t \simeq 1$ day, the duration of the bolometric light curves can last ~ 1 week. The spectral energy distribution (SED) is highly suppressed in the optical, with the bulk of the energy emitted in the infrared. Such findings can inform observational searches for an EM counterpart to a GW trigger by clarifying the transient timescales, the bands in which EM emission will be strongest (or have the most distinct signature), and the distances out to which we might expect a successful EM detection.

2.2 Opacity of r-process ejecta

Supernova calculations suggest that at blue wavelengths bound-bound transitions from complex iron group elements dominate other forms of opacity, such as electron scattering, free-free, and photoionization (see e.g. Pinto & Eastman 2000). Literally millions of lines, Doppler-broadened by the remnant's differential velocities, contribute to a psuedo-continuum bound-bound opacity. Photons traveling through the ejecta are continually Doppler-shifted with respect to the comoving frame, and come into resonance with multiple transitions one by one. The velocity gradient of the remnant thus enhances the effective line opacity, an idea introduced by Karp et al. (1977) and further developed in subsequent studies (Friend & Castor 1983; Eastman & Pinto 1993; Hoeflich et al. 1993). We use here the formalism given by Eastman & Pinto (1993) where the extinction coefficient is given by

$$\alpha_{\rm exp}(\lambda_{\rm c}) = \frac{1}{ct_{\rm exp}} \sum_i \frac{\lambda_i}{\Delta\lambda_{\rm c}} (1 - e^{-\tau_i}). \tag{2.1}$$

This formula represents an average over discrete wavelength bins, where $t_{\rm exp}$ is the time since mass ejection, λ_c is the central wavelength of the bin, $\Delta\lambda_c$ is the bin width, τ_i is the Sobolev optical depth of a line (Sobolev 1960), and the sum runs over all lines in the bin. The extinction coefficient is related to the expansion opacity by $\kappa_{\rm exp} = \alpha_{\rm exp}/\rho$, where ρ is the gas density. In applying the Sobolev formalism, we make two important assumptions: first, that the intrinsic (Doppler) width of lines is small compared to the velocity scale over which the ejecta properties vary, and second, that the intrinsic profiles of strong lines do not overlap with other lines. While the first condition is easily satisfied in rapidly expanding NSM ejecta, the second may not be (see K13), and a non-Sobolev treatment may ultimately be necessary for a fully rigorous treatment of the radiation transport.

To calculate Sobolev line optical depths, we assume that the atomic level populations are set by local thermodynamic equilibrium (LTE). This approximation should be reasonable in the optically thick regions of ejecta, where the radiation field tends towards a blackbody distribution. Baron et al. (1996), for example, show that in Type Ia SN models the atomic level populations acquire their LTE values near and below the SN photosphere. Jack et al. (2011) have quantified the impact of non-LTE (NLTE) effects on the theoretical light curves of Type Ia SNe in the ∼month following explosion. They find moderate ($\lesssim 30\%$) differences in the broadband fluxes in the optical U, B,V, and R bands (wavelengths for which the ejecta is optically thick) and larger effects ($\sim 50\%$) in the longer wavelength I-band (at which the ejecta becomes transparent). While the density of NSM ejecta is lower than that of ordinary SNe, the opacity is much higher in both the optical and the infrared; we therefore expect that errors in our predicted fluxes due to NLTE effects will also be at similarly moderate levels, at least during the optically thick phases that we focus on here (i.e., before and just after the light curve peak). Such errors, while deserving of further study, are likely less significant than the uncertainties related to the atomic line data and ejecta model geometry. At later times, (~ 1 week after peak) when the remnant becomes optically thin, LTE breaks down completely and our predicted colors become unreliable.

The expansion opacity takes a simplified form in atmospheres where most lines are extremely optically thick ($\tau \gg 1$). As τ_i increases, the dependence of $\kappa_{\rm exp}$ on optical depth is eliminated ($1 - e^{-\tau_i} \simeq 1$), and the expression for expansion opacity simplifies to a sum of optically thick lines. The dependence on density and other determinants of optical depth are concomitantly reduced. Under these conditions, the number of distinct optically thick lines in each bin becomes the most important predictor of ejecta opacity. An exhaustive tally of lines is therefore essential to accurately modeling ejecta opacity. Unfortunately, there is relatively little line data available for the heavy elements ($Z > 28$) expected to be synthesized in NSM ejecta. We compiled the line data calculated by the Mons group (Biémont et al. 1999; Palmeri et al. 2000; Quinet & Biémont 2004) and included in the VALD database (Heiter et al. 2008), which includes moderately extensive data for a couple heavy ions (e.g. CeII, CeIII), but very little for most other species.

On theoretical grounds, we expect the lanthanides (atomic numbers $Z = 58 - 72$) to contribute significantly to ejecta opacity, due to the complicated structure of their valence f-shells. This argument is illustrated with a simple combinatorics heuristic. The number of substates corresponding to a given electron orbital is roughly

$$C = \frac{g!}{n!(g-n)!} \quad \text{with } g = 2(2l+1), \tag{2.2}$$

where n is the number of valence electrons and l is the angular momentum quantum number of the valence shell. The number of lines should scale as C^2, and will be much greater for ions with electrons in an open f ($l = 3$) shell. Assuming lines from the two species are equally likely to be optically thick, we expect atmospheres containing lanthanides to have a much higher opacity than atmospheres of pure iron. A similar argument could be applied to elements of the actinide series, which may also be produced in the merger ejecta. However, the mass fractions of most actinides are predicted to be low, and can likely be ignored.

Our calculations of opacities using line data from VALD demonstrate that the lanthanides have a much higher expansion opacity than iron, as shown in Figure 2.1. However, the limited line data available in the VALD database is inadequate for calculating r-process opacities over the wavelength and temperature range needed for a realistic transport calculation. For example, VALD includes virtually no line data for ionization states greater than doubly ionized. Thus, at early times (1 or 2 days after the merger) when the ejecta is rather hot and highly ionized, the VALD data severely underestimates the opacity and results in unrealistic light curves and colors. A more serious and persistent issue is that VALD contains almost no lines with wavelengths greater than 1 μm, and so can not be used at any epoch to calculate a sensible infrared opacity or emissivity. We will find that most of the emission from NSMs is in fact radiated at wavelengths $\gtrsim 1$ μm, which means that more extensive infrared line data is needed to reliably predict the broadband light curves and colors.

Give the limitations of the VALD line data, we use instead the theoretical lanthanide line data of K13 derived from the atomic structure modeling code Autostructure (Badnell 2011). This supplies approximate radiative data for neodymium ($Z = 60$) and a few other elements over the entire wavelength range of interest ($\sim$ 100 - 100,000 Å). We tested the reliability of the Autostructure data by comparing predicted expansion opacities of select species, including Fe and Ce, to those calculated using existing line data in VALD. Overall, the results from both data sets are found to be in good agreement, as Figure 2.1 demonstrates

Until Autostructure models for all lanthanides are calculated, we use an averaging scheme to predict ejecta opacities based on a few representative species. We recast the ejecta composition computed by Roberts et al. (2011) in terms of two groups of elements: iron-like elements (i.e., the d-block of the periodic table) and neodymium-like elements (i.e., the lanthanides). The line data for iron is taken from Kurucz & Bell (1995a), while that of Nd is derived from Autostructure calculations. We take the mass fraction of Nd (Fe) to be equal to the average mass fraction of the lanthanides (d-block elements). The remainder of the composition is taken to be calcium, which serves as a low-opacity filler with an appropriate ionization potential.

Since each ion species in the ejecta has a unique set of strong lines, and since $\kappa_{\rm exp}$ increases with the number of strong lines, mixtures with a greater diversity of elements will have higher opacity. Since both Nd and Fe both have intermediate complexity for their respective blocks, their opacities can presumably be taken as representative of other elements in the same region of the period table. We therefore assume that each lanthanide or d-block element in the original compositions provides an opacity equal to that of Nd or Fe, respectively, and arrive at a generalized expression for the extinction coefficient

$$\alpha_{exp} = \frac{1}{ct_{\rm exp}} \sum_{\rm Z} N_{\rm Z} \sum_i \frac{\lambda_i}{\Delta\lambda_{\rm c}} \left(1 - e^{-\tau_i(\rho_{\rm Z})}\right), \tag{2.3}$$

where Z runs over the representative elements (here Fe and Nd), $N_{\rm Z}$ is the number of elements in the block represented by Z, and $\rho_{\rm Z} = \chi_{\rm Z}\rho$, with $\chi_{\rm Z}$ the mean mass fraction of the representative elements. Since lanthanide contributions dominate the opacity, the boosting procedure effectively increases the opacity by a factor of 14, the number of lanthanide species.

Figure 2.1 shows the expansion opacity calculated for typical parameters of NSM ejecta ($\rho = 10^{-13}$ g cm^{-3}, $T = 5 \times 10^3$ K, and $t_{\rm exp} = 1$ day). The values vary with temperature and density, but in general our calculations indicate r-process opacities many orders of magnitude higher than those calculated for iron group elements. The r-process elements also have a greater density of strong lines at long wavelengths; thus, the the bound-bound opacity in NSM ejecta remains relatively high even in the infrared, and provides the dominate source of opacity over the relevant range of the electromagnetic spectrum.

2.3 Light curves of r-process transients

The surprisingly high opacity of r-process material, discussed in §2.2, has important implications for the EM emission from NSMs. In this section, we present radiation transport calculations using our refined opacity estimates to determine the bolometric and broadband light curves of r-process outflows. Our predictions diverge from those of earlier studies, which assumed that the opacities were similar to those of iron.

2.3.1 Ejecta Model

We model the NSM ejecta as a spherically symmetric outflow undergoing homologous expansion. In reality, the ejecta may have a highly asymmetric, "tidal tail" geometry (Rosswog 2005). 3-D transport calculations suggest that this asphericity makes the emission moderately anisotropic, but does not qualitatively change the shape of the light curves (Roberts et al. 2011). We describe the density of the ejecta using the broken power law profile introduced by Chevalier & Soker (1989), in which density decreases as $r^{-\delta}$ in the inner layers of the atmosphere and as r^{-n} (with $n > \delta$) in the outer layers. The shift from n to δ occurs at the transition velocity

$$v_t = 7.1 \times 10^8 \zeta_v \left(E_{51}/M\right)^{1/2} \text{ cm s}^{-1}, \tag{2.4}$$

where E_{51} is the explosion energy $E/10^{51}$ ergs, M is the ejecta mass $M_{\rm ej}$ in units of $M_\odot$, and ζ_v is a numerical constant. For $v < v_t$, the density is given by

$$\rho(r,t) = \zeta_\rho \frac{M_{\rm ej}}{v_t^3 t^3} \left(\frac{r}{v_t t}\right)^{-\delta}, \tag{2.5}$$

and an analogous expression describes the outer layers. The constants ζ_v and ζ_ρ satisfy the requirement that the density profile integrates to the specified mass and energy. We also tried using an exponentially decreasing density profile, but found that the light curves were mostly insensitive to the details of the density structure. The results presented here were generated using the broken power law profile with $(\delta, n) = (1, 10)$.

The mass and velocities of the matter ejected during compact object mergers is still uncertain. Simulations of NSMs (e.g. Rosswog et al. 1999; Oechslin et al. 2007; Goriely et al. 2011; Bauswein et al. 2013; Hotokezaka et al. 2013b) and of neutron star-black hole mergers (e.g. Janka et al. 1999; Lee 2001; Rosswog 2005) have found that the amount of material

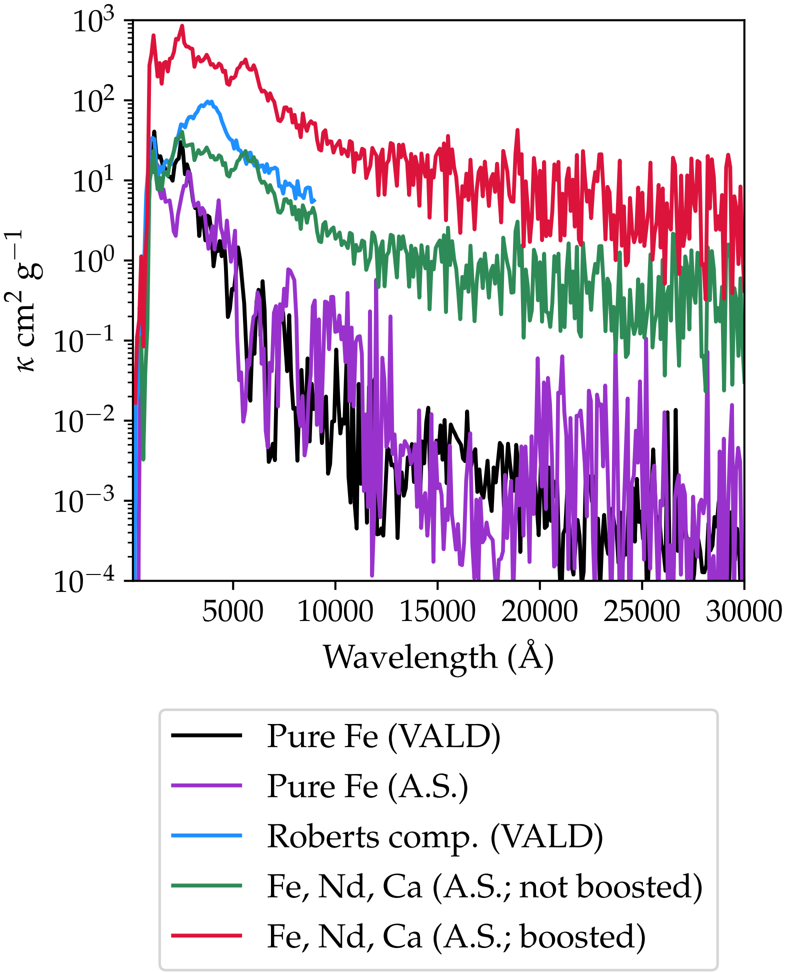

Figure 2.1: Wavelength dependent expansion opacities for ejecta with $\rho = 10^{-13}$ g cm^{-3}, $T = 5000$ K, and $t_{\rm exp} = 1$ day. The opacity of iron is calculated using both the VALD and Autostructure linelists to demonstrate the reliability of the latter approach. The r-process opacity calculated using Autostructure data for Nd is in fairly good agreement with that using the VALD linelist (which includes extensive line data for only a few heavy elements). The *boosted* r-process opacity takes into account the diversity of species in an r-process mixture by assuming that all lanthanides have an opacity comparable to Nd.

ejected is sensitive to binary type, mass ratio, nuclear equation of state, and the treatment of gravity (Newtonian v. general relativistic). However, taken in aggregate, simulations suggest NSM may eject $\sim 10^{-2}\ M_\odot$ of material with velocities on the order of $\beta = v/c \sim 0.1$. We adopt these parameters as our fiducial model, but vary the mass and velocity scales over the range $M_{\rm ej} = 10^{-3} - 10^{-1} M_\odot$, and $\beta_{\rm char} = 0.1 - 0.3$, where we define the characteristic velocity by

$$E = \frac{1}{2} M_{\rm ej} \left(\beta_{\rm char} c\right)^2 . \tag{2.6}$$

We assume the ejecta to be homogenous, and composed of either pure r-process material or pure ^{56}Ni. For models with r-process elements, all zones are assumed to have the same radioactive decay rate given by Roberts et al. (2011). Of the decay energy, 10% is taken to be in fission fragments, and 90% in beta decays. Of the beta decay energy, 25% is assumed to be lost to neutrinos, with the remaining 75% split equally between leptons and gamma-rays. Leptons and fission fragments are assumed to thermalize promptly and locally, while we use a radiation transport scheme to follow the propagation and absorption of gamma rays. This approximate apportioning of the decay energy is based on the physical considerations given in Metzger et al. (2010).

2.3.2 Light Curves

We generate synthetic observables of our ejecta models using the time-dependent multi-wavelength radiation transport code SEDONA (Kasen et al. 2006). Beginning at an initial time of 0.1 days after mass ejection, the code follows the temperature and density evolution of the expanding ejecta, taking into account radiative and radioactive heating as well as cooling by expansion. The wavelength dependent r-process and iron opacities are calculated in each zone using the Autostructure and Kurucz & Bell (1995a) line data, respectively. The ionization and excitation state of the gas are assumed to be set by LTE, and lines are taken to be completely absorbing. SEDONA synthesizes the emergent spectral time series, from which we construct bolometric and broadband light curves. Table 2.1 summarizes the EM properties of the models we investigated.

In Figure 2.2, we plot the bolometric light curves of r-process transients for a subset of the parameter grid. For comparison, we also show a light curve calculated using iron-like opacities. Introducing more realistic r-process opacities clearly changes the picture significantly – the light curves have slower rise times and broader, dimmer peaks than those calculated with iron-like opacities. Notably, the r-process transients do not in general have the ~ 1 day duration thought to be a distinguishing feature of these events, and instead may last a week or longer.

That higher opacities give broader, dimmer light curves is expected theoretically. The duration of radioactively powered bolometric light curves is set by the effective diffusion time through the ejected material (Arnett 1979),

$$t_{\rm d} \simeq \left(\frac{M_{\rm ej}\kappa}{vc}\right)^{\frac{1}{2}} , \tag{2.7}$$

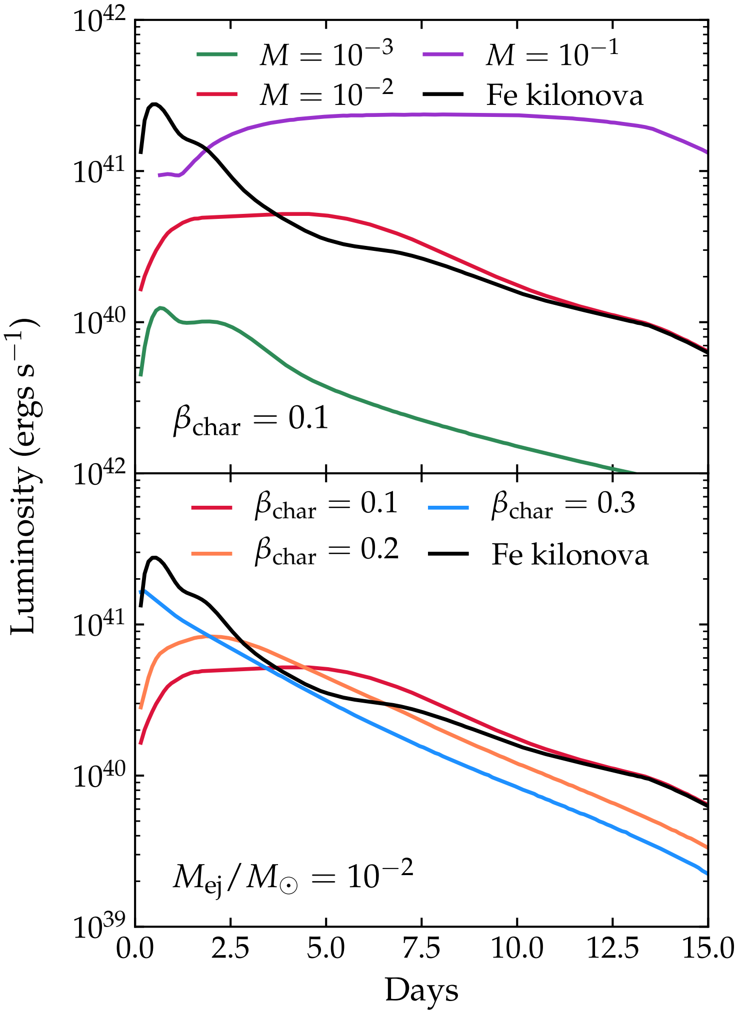

Figure 2.2: Synthetic bolometric light curves of r-process transients with different ejecta masses $M = M_{\rm ej}/M_\odot$ (top panel) and velocities (bottom panel). For comparison, we also show the light curve of a model with fiducial ejecta parameters ($M_{\rm ej} = 10^{-2}\ M_\odot$, $\beta_{\rm char} = 0.1$) but calculated assuming iron-like opacities (black lines). The higher opacities of r-process ejecta lead to significantly broader light curves. The models with higher ejecta velocities correspond to shorter rise times and steeper declines, while those with higher masses have greater luminosities and longer durations.

Table 2.1: Peak magnitudes and light curve properties of r-process transients

$M_{\rm ej}(M_\odot)$	β	composition	$L_{\rm p,bol}$[a]	$t_{\rm p,bol}$[b]	$M_{\rm B}$	$M_{\rm R}$	$M_{\rm I}$	$M_{\rm H}$
10^{-3}	0.1	r-proc	1.2×10^{40}	0.65	-9.3	-11.2	-12.0	-14.0
10^{-3}	0.2	r-proc	1.6×10^{40}	0.75	-9.1	-11.3	-12.6	-14.1
10^{-3}	0.3	r-proc	3.5×10^{40}	0.15	-9.3	-12.4	-13.6	-14.7
10^{-2}	0.1	r-proc	5.2×10^{40}	4.25	-11.2	-12.7	-13.3	-15.8
10^{-2}	0.2	r-proc	8.5×10^{40}	1.85	-11.4	-12.8	-14.0	-15.9
10^{-2}	0.3	r-proc	1.7×10^{41}	0.25	-11.8	-14.1	-15.2	-16.5
10^{-1}	0.1	r-proc	2.4×10^{41}	8.65	-12.9	-14.1	-14.6	-17.5
10^{-1}	0.2	r-proc	4.1×10^{41}	4.35	-13.4	-14.3	-15.4	-17.5
10^{-1}	0.3	r-proc	7.2×10^{41}	0.25	-14.0	-15.5	-16.7	-18.1
10^{-3}	0.1	^{56}Ni	3.5×10^{40}	0.25	-13.0	-12.6	-12.6	-11.8
10^{-2}	0.1	^{56}Ni	3.7×10^{41}	0.75	-15.4	-14.9	-14.5	-14.8

[a] Peak bolometric luminosity, in ergs s^{-1}

[b] Rise time to bolometric light curve peak, in days

where v is a characteristic ejecta velocity and κ an appropriately wavelength-averaged opacity. Because the r-process opacities are $10-100$ times larger than those of iron, the diffusion time is significantly lengthened. The longer diffusion time also leads to a dimmer luminosity at peak, as a greater fraction of the radioactive energy is lost due to expansion before it can be radiated. The models roughly obey Arnett's law – i.e., the emergent luminosity and instantaneous radioactive energy input are approximately equal at peak (Arnett 1979, 1982).

The r-process powered bolometric light curves vary with the ejecta properties in predictable ways. Higher mass ejections give a greater luminosity and longer duration, due to their larger radioactive mass. Ejecta models with higher kinetic energies have shorter rise times, reach greater peak luminosities, and decline more rapidly than their lower energy analogues. Over the reasonable range of ejecta parameters considered here, the light curves exhibit significant diversity – the peak luminosities vary by more than an order of magnitude, and the durations range for $\lesssim 1$ day to as long as two weeks.

The broadband magnitudes of the models also differ significantly from previous expectations. Figure 2.3 shows that, compared to a model that uses iron-like opacities, r-process transients output much more energy in red and infrared bands, with a strong suppression of the optical emission. We find bright, broad peaks in the J, H, and K bands, while the U, B, and V bands are heavily line blanketed and decline sharply at early times. Figure 2.4 shows that the colors of the fiducial r-process model redden rapidly over the first day or two, and afterwards become remarkably constant, with the SED peaking in the infrared at around $\sim 1\ \mu$m. Other than the very red color, the spectra at these phases resemble those of other high-velocity SNe, with a pseudo blackbody continuum and broad (~ 200 Å) spectral features (see K13 for further discussion).

The behavior of the broadband light curves can be understood by examining the photospheric properties of r-process transients, since the observed SED roughly corresponds to a

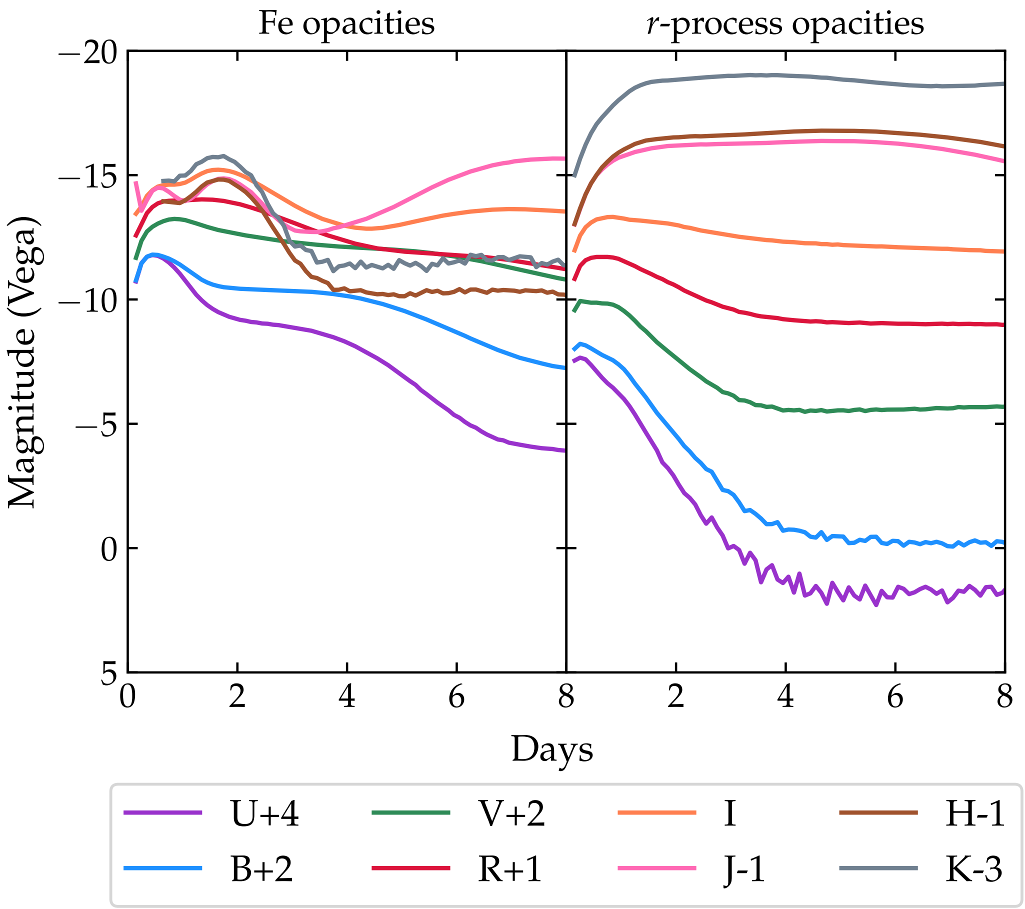

Figure 2.3: Synthetic broadband light curves for the fiducial ejecta model calculated using iron-like opacities (left) and r-process opacities (right). The effect of r-process opacities is to suppress the optical emission and shift the radiation toward redder bands, in particular the infrared J, H and K bands.

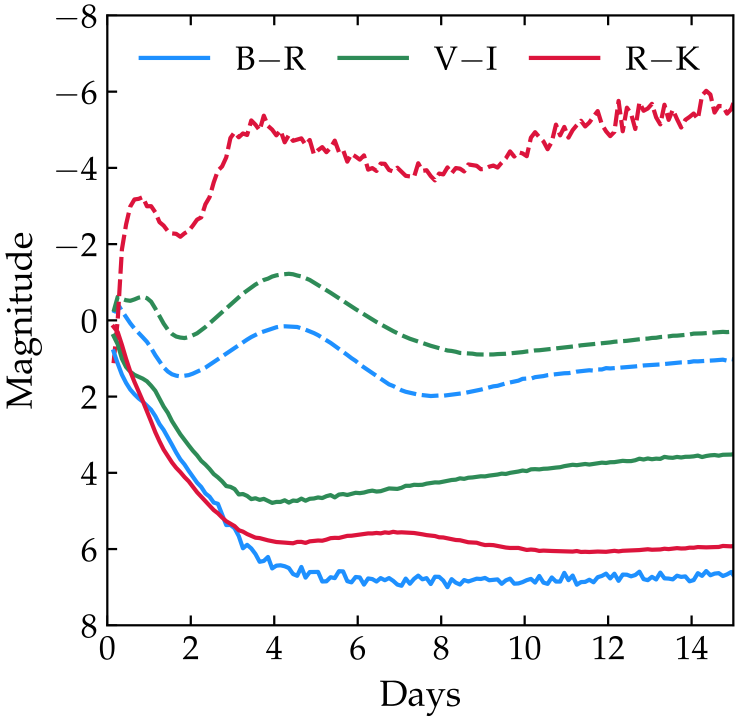

Figure 2.4: Select colors for the fiducial model calculated using r-process (solid lines) and iron-like (dashed lines) opacities. The colors of r-process transients initially redden rapidly, then reach a phase of constant color characterized by a blackbody at $T \approx 2500$ K.

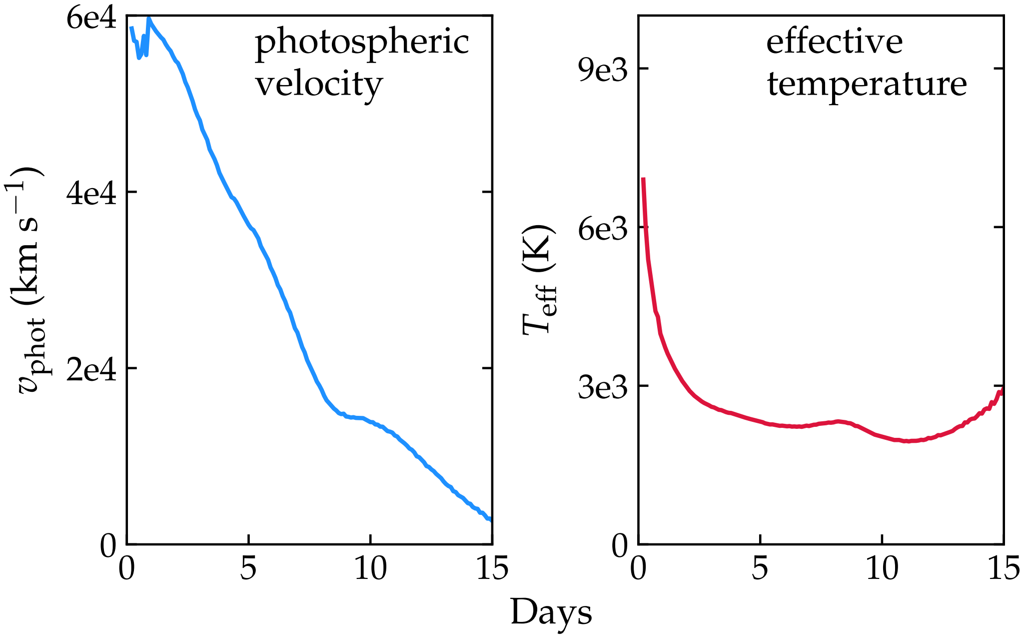

Figure 2.5: Evolution of the photospheric temperature and velocity in the fiducial model, using r-process opacities. The photospheric temperature initially declines rapidly, but at times $\gtrsim 2$ days settles to a fixed value near the recombination temperature of the lanthanides.

blackbody at the photospheric temperature and radius. In Figure 2.5, we plot the velocity and temperature evolution of the photosphere, the surface defined by

$$\tau(r_{\rm phot}) = -\int_{\infty}^{r_{\rm phot}} \overline{\kappa}_P(r)\rho(r){\rm d}r = 1, \tag{2.8}$$

where $\overline{\kappa}_P(r)$ is the Planck mean opacity, computed from our r-process line data.

In the initial phases, the photospheric velocity and temperature decline steadily, reflecting the decrease in density and the cooling of the ejecta due to expansion. At around ~ 2 days, however, the photospheric temperature stabilizes at $T \simeq 2500$ K. Since this is close to the first ionization temperature of the lanthanides, this plateau probably reflects the sharp drop in opacity that occurs when these elements recombine to neutral (K13). Recombination occurs in the cooler outer layers first, and a sharp ionization front forms in the ejecta. Photons pass easily through the cooler, neutral outer layers, but are trapped in the ionized inner regions – the photosphere thus forms at the ionization front. During this phase, the emergent colors are roughly constant in time and resemble those of a blackbody at the lanthanide recombination temperature. Over time, the recombination front recedes inward, reaching the center at around 14 days. At this point, the ejecta is nearly entirely neutral and transparent.

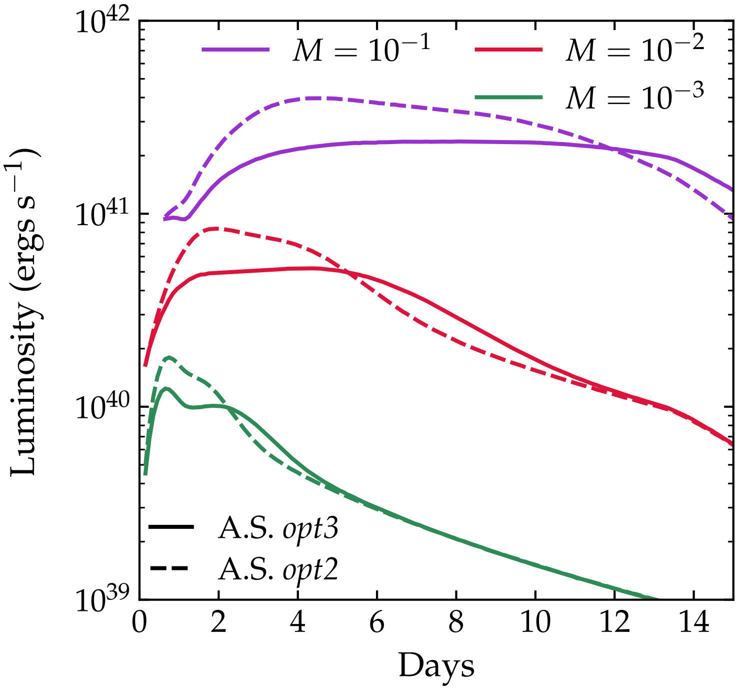

Figure 2.6: Bolometric light curves for $\beta_{\rm char} = 0.1$ and a range of ejecta masses, calculated using line data with from two different Autostructure models of Nd, each with a somewhat different energy level structure. Solid curves correspond to our preferred Autostructure model (*opt3*), while dashed curves show results from an alternative model (*opt2*). The moderate differences can be taken as a rough estimate of the error resulting from uncertainties in the Nd structure models.

2.3.3 Uncertainties in the Opacities

Though our r-process opacities represent an improvement over previously available data, the Autostructure models of Nd are subject to uncertainties. In particular, the structure models rely on an *ab-initio* optimization, such that the predicted atomic level energies and line wavelengths generally differ from the experimental values. To explore the effects of these uncertainties, we calculated bolometric and broadband light curves using two different Autostructure models of Nd (*opt2* and *opt3* from K13) each with a somewhat different energy level structure. The *opt3* model reproduces the low lying energy levels of NdII quite well, while the *opt2* model has generally higher excitation energies which are harder to populate under our assumption of LTE. The result is fewer strong lines and a lower overall opacity for the *opt2* case.

In Figure 2.6, we plot bolometric light curves for ejecta models with $\beta_{\rm char} = 0.1$ and a variety of masses. The light curves calculated using the *opt2* line data have somewhat sharper, more luminous peaks and swifter declines, consistent with the expected lower opacities. The differences, however, are fairly modest, and the bolometric luminosity never differs by more than a factor of ~ 3. The effects are more noticeable in the broadband light curves (Figure

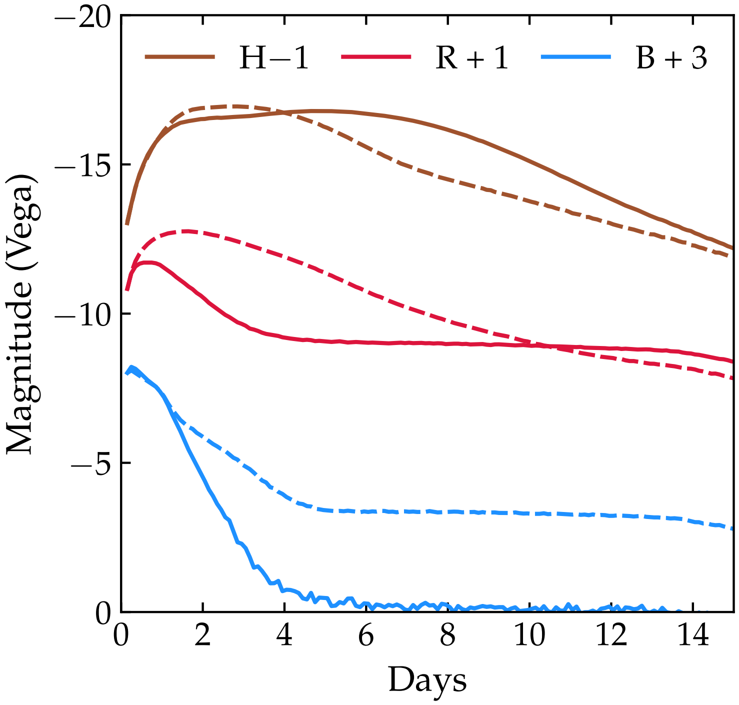

Figure 2.7: A comparison of broadband curves of the fiducial model, calculated using line data with from two different Autostructure models of Nd, each with a somewhat different energy level structure. Calculations using the *opt2* line data (dashed lines) predicts higher magnitudes for the optical B-, and R-bands than those with the *opt3* line data (solid lines)

2.7). In particular, the R-band light curves are $\sim 1-2$ magnitudes brighter for the *opt2* data, which could have important implications for detectability. Based on comparison to experiment, we expect the *opt3* data to be more reliable, however further work refining the opacities is clearly warranted.

In addition to errors inherent in the individual structure models, a perhaps larger uncertainty in our r-process opacities arrises from the fact that we represent all lanthanides with the radiative data of Nd. In fact, the lanthanides with a nearly half open f-shell (in particular gadolinium) will be significantly more complex, with perhaps ~ 10 times as many lines of Nd. We therefore suspect that our current calculations underestimate the true opacity. The light curves we present here suggest that increasing the opacity further will lead to an even greater suppression of optical emission.

2.3.4 A ^{56}Ni-powered transient

Given that the radioactive light curves of NSMs depend strongly on the composition of the ejecta, it is worth considering whether any elements lighter than the lanthanides may be produced in these events. While the material dynamically ejected in the merger itself (the tidal tails) is thought to undergo robust r-process nucleosynthesis, it is plausible that a comparable amount of mass may subsequently be blown off in winds from an accretion disk surrounding the merged remnant. Though the physical properties of the disk winds remain uncertain, neutrino irradiation may drive the electron fraction to $Y_\mathrm{e} \gtrsim 0.4$, in which case the nucleosynthesis may not extend past $Z \sim 50$ (Surman et al. 2006, 2008; Metzger et al. 2008; Darbha et al. 2010). If Y_e is very close to 0.5, the composition will be primarily ^{56}Ni. In this case, the EM signature of a merger may be a superposition of a ^{56}Ni- and an r-process-powered transient.

To address this possibility, we consider a simplified scenario where $10^{-3} - 10^{-2} M_\odot$ of pure ^{56}Ni is blown off in a wind immediately post-merger. Consistent with our use of spherical symmetry thus far, we model this wind as a spherical outflow, with $\beta_\mathrm{char} = 0.1$ and the same broken power law density profile with $(n, \delta) = (1, 10)$. We consider the tidal tails and disk wind to be two separate, non-interacting components, which is perhaps not unreasonable given that the winds are likely collimated in the polar regions, while the tidal tails are largely confined to the orbital plane. Ignoring viewing angle effects, we take the two component light curve to simply be the superposition of the individual ^{56}Ni-powered and the r-process powered light curves.

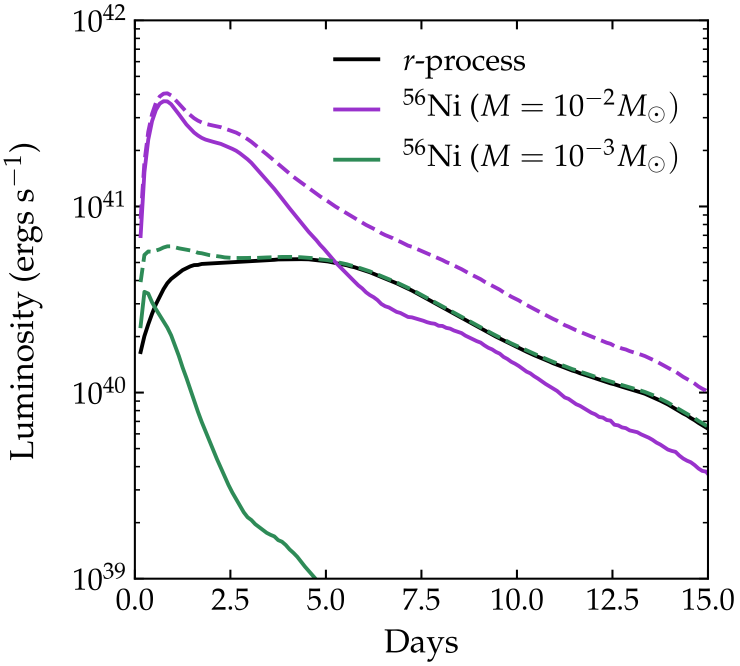

Figure 2.8: Bolometric light curves for models that include two components: r-process material (from tidal tails) and ^{56}Ni (from a disk wind.) We show the fiducial model r-process light curve, and light curves for two different masses of ejected ^{56}Ni in solid lines.

Figure 2.8 shows the two component light curves, for two different ratios of the ^{56}Ni wind mass (M_ni) to the r-process tidal tail mass (M_rp). For $M_\mathrm{ni} \ll M_\mathrm{rp}$, the primary effect of the ^{56}Ni wind is to raise the early-time luminosity, creating a very short peak at $t \sim 1$ day, which blends into long, flat, r-process light curve. The cumulative light curve thus appears to have a faster rise time and longer plateau. If $M_{\rm ni} \approx M_{\rm rp}$, the ^{56}Ni emission dominates the r-process emission for the first ~ 5 days post merger, with the two components contributing roughly equally thereafter. The net effect is a gradually declining light curve, with the long r-process plateau obscured by the ^{56}Ni-powered light curve.

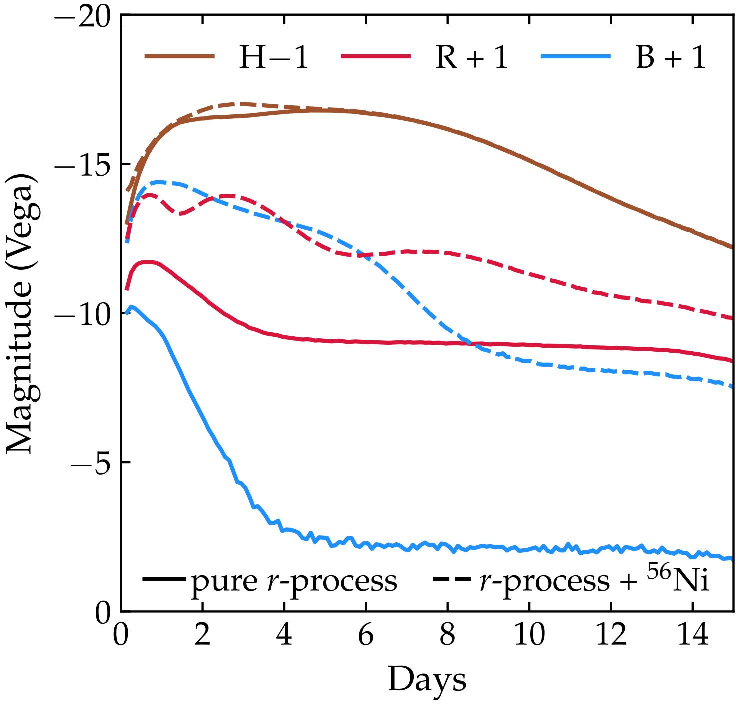

Figure 2.9: A comparison of select broadband light curves for a pure r-process transient (solid lines) and an r-process transient occurring in concert with a ^{56}Ni-powered outflow (dashed lines). The bluer SED from the ^{56}Ni shifts the magnitudes of the bluer bands of the combined SED upward relative to a pure r-process model. This plot is for $M_{\rm ni} = M_{\rm rp} = 10^{-2} M_\odot$.

The addition of a ^{56}Ni component also affects the SED of the transient, as shown in Figure 2.9 for the case $M_{\rm ni} = M_{\rm rp} = 10^{-2} M_\odot$. Given the much lower iron group opacities, the SED of the ^{56}Ni ejecta is much bluer than that of the r-process ejecta. The emission in the optical bands (U,B,V,R) is relatively bright and set by ^{56}Ni mass, while the r-process material establishes the behavior in the infrared bands. Such an unusual SED may serve as an EM fingerprint that could improve the prospects for positively identifying a NSM. In particular, as shown in Figure 2.10, the spectrum of a two component outflow is, to first approximation, the superposition of two blackbodies – a sharply peaked bluer blackbody, corresponding to the ^{56}Ni ejecta, and a lower, redder one, corresponding to the r-process material.

The aggregate light curve model we present here glosses over some of the more complex

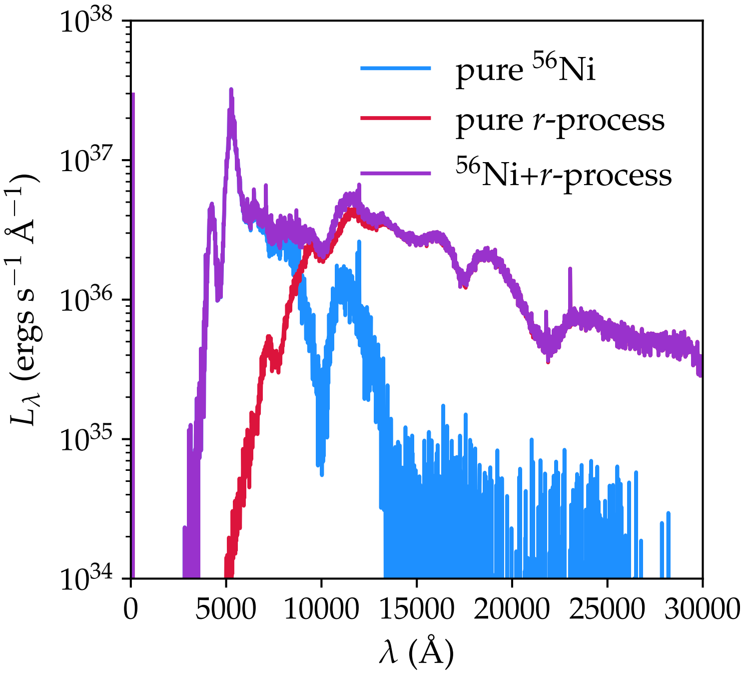

Figure 2.10: A combined ^{56}Ni and r-process spectrum at $t = 7$ days, taking $M_{\rm ni} = M_{\rm rp} = 10^{-2} M_\odot$. The peak at blue wavelengths is due to the ^{56}Ni, while the r-process material supplies the red and infrared emission. The best fit blackbody curves to the individual spectra are overplotted in dashed black lines ($T_{\rm ni} \simeq 5700$ K, $T_{\rm rp} \simeq 2400$ K). The combined spectrum generally resembles asuperposition of two blackbodies at different temperatures.

physical processes. Our model assumes spatially distinct regions of pure ^{56}Niand pure r-process material. In reality, the nucleosynthetic yields are highly sensitive to the conditions in the wind, and it is possible that disk outflows contain some elements heavier than ^{56}Ni. Contamination of the outflows with even a small mass fraction of lanthanides ($\sim 10^{-3}$) can significantly increase the opacities and the optical line blanketing. Even if our simplified compositions turn out to be reasonable, our model does not account for the geometry of the ejecta and any possible mixing of the wind and tidal tail components. Given the presumably high level of asymmetry, the net (tails + wind) EM output may depend heavily on orientation, making our simple superposition procedure valid only along certain lines of sight.

2.4 Conclusion

We have shown that the radioactive powered light curves associated with NSMs are greatly modified when more realistic values for the opacities of r-process material are taken into account. The r-process opacities are much higher than those of iron, due to both the complexity of heavy elements (in particular the lanthanides) and the diversity of atomic species present. Refining our understanding of the atomic structure of these elements is an important step toward a more rigorous model of transients from merging compact objects.

In accordance with theoretical expectations, the extremely high r-process opacities result in bolometric light curves that are broader and dimmer than those calculated assuming iron-like opacities. Our calculations indicate that the light curves are likely to last at least a few days, and may endure as long as a week or two in certain cases. The broadband magnitudes are also significantly impacted; we find heavy line blanketing in the optical and UV bands, with most of the radiation emitted in the near infrared. The colors at later times are fairly constant, and regulated to be similar to a blackbody at $T \approx 2500$ K, the recombination temperature of the lanthanides.

These findings have important, if mixed, consequences for the detectability of EM counterparts to NSMs. On the one hand, we predict dimmer bolometric luminosities and SEDs largely shifted into the infrared, both of which pose serious challenges to observational surveys at optical wavelengths. On the other hand, the light curves are of longer duration, and so may not require quite as a high cadence of observations. Perhaps more importantly, the uniquely high opacity of r-process ejecta provides signatures that may allow us to distinguish NSMs from other sorts of dim transients. In particular, the SED of r-process ejecta peaks in the infrared, with a color temperature set by lanthanide recombination. If the merger ejects two separate mass components — r-process tidal tails and a ^{56}Ni wind – the dual spectrum may be quite distinctive, with discernible infrared and optical components.

The SEDs we predict can be used to roughly estimate the detectability, given the varying depths and wavelength coverage of different observing facilities (e.g. Nissanke et al. 2013b). For example, Pan-STARRS (see http://pan-starrs.ifa.hawaii.edu) and PTF (Law et al. 2009) achieve an R-band depth of $M_R \sim 21$ magnitudes, while LSST reaches a depth of $M_{\rm R} \sim 24$ (LSST Science Collaborations 2009). We find that an r-process transient with fiducial model parameters will peak at $M_{\rm R} = -13$, which under ideal observing conditions, would be observable to Pan-STARRS or PTF out to a distance of ~ 60 Mpc. This is an interesting, but rather small fraction of the volume probed by advanced LIGO/VIRGO. The case with LSST is more promising, with sensitivity in the R-band out to ~ 250 Mpc. Discovery of r-process ejecta in the U or B bands with any facility would appear to be quite difficult, given the heavy line blanketing at these wavelengths.

Given that our models predict that most of the emission is at longer wavelengths, improving detection capabilities in the near infrared may greatly aid in future searches for EM counterparts. Ground based facilities with sensitivity in the I or Y bands ($0.8 - 1.1\mu$m) may want to make use of these capabilities, as the r-process transients are generally ~ 1 magnitude brighter in these bands than in R-band. The construction of space based facilities such as WFIRST (Green et al. 2012) and Euclid (Amendola et al. 2012) would be of particular interest. WFIRST is proposed to have an H-band depth of ~ 25 magnitudes, with Euclid achieving a similar sensitivity. As our fiducial model is much brighter in the infrared ($M_{\rm H} \simeq$ -15) than in the optical bands, such facilities could potentially make a detection out to a distance of ~ 1000 Mpc, encompassing the entire LIGO/VIRGO volume.

Discovering the EM counterparts to NSMs would be made significantly easier if, in addition to r-process elements, these events also separately eject some significant amount of ^{56}Ni or lower mass ($Z < 58$) radioactive isotopes. Our models predict that such "lanthanide-free" light curves are reasonably bright in the optical bands ($M_{\rm B} \approx M_{\rm R} \approx -15$) and would be within range for many upcoming optical transient surveys. It is possible that winds from a post-merger accretion disk may produce such lighter element outflows, although more detailed simulations are needed to constrain the mass and composition of the material ejected. Clearly any detection of a short-lived optical transient should, if possible, be immediately followed up at infrared wavelengths to look for a coincident r-process transient from the tidal tails. Discovery of such a two component light curve and spectrum would be a very strong signature of a NSM. It would also provide insight into the merger and post-merger physics by constraining the mass ejected by different mechanisms.

The work we have presented here is an important step towards improving our predictions of the radioactive transients from NSMs. However, much remains to be done. The opacities we have used, while more realistic than previous estimates, are still subject to important uncertainties. In particular, we need comprehensive structure calculations to derive radiative data for all lanthanides. In addition, more detailed simulations of the dynamics and nucleosynthesis of the mass ejection are needed to better predict the mass, composition, and geometry of the ejecta. Of special interest are the properties of the disk wind and any mixing of these outflows with the tidal tail material. Finally, 3-dimensional radiative transfer calculations will be needed to predict the light curves of multi-component mass ejections and to determine their dependence on viewing angle. Such theoretical work should improve our understanding of the EM counterparts to gravitational wave sources, and the heavy elements they produce.

Chapter 3

Radioactivity and thermalization in the ejecta of compact object mergers and their impact on kilonova light curves

This chapter reproduces material previously published in Barnes, Kasen, Wu, & Martínez-Pinedo (2016), with permission from all co-authors and the AAS.

One promising electromagnetic signature of compact object mergers are kilonovae: approximately isotropic radioactively-powered transients that peak days to weeks post-merger. Key uncertainties in kilonova modeling include the emission profiles of the radioactive decay products—non-thermal β-particles, α-particles, fission fragments, and γ-rays—and the efficiency with which their kinetic energy is absorbed by the ejecta. The radioactive energy emitted, along with its thermalization efficiency, sets the luminosity budget and is therefore crucial for predicting kilonova light curves. We outline uncertainties in the radioactivity, describe the processes by which the decay products transfer energy to the ejecta, and calculate time-dependent thermalization efficiencies for each particle type. We determine the net thermalization efficiency and explore its dependence on r-process yields—in particular, the production of α-decaying translead nuclei—and on ejecta mass, velocity, and magnetic fields. We incorporate our results into detailed radiation transport simulations, and calculate updated kilonova light curve predictions. Thermalization effects reduce kilonova luminosities by a factor of roughly 2 at peak, and by an order of magnitude at later times (15 days or more after explosion). We present analytic fits to time-dependent thermalization efficiencies, which can be used to improve light curve models. We revisit the putative kilonova that accompanied gamma ray burst 130603B, and estimate the mass ejected in that event. We find later-time kilonova light curves can be significantly impacted by α-decay from translead isotopes; data at these times may therefore be diagnostic of ejecta abundances.

3.1 Introduction

In addition to producing kilohertz gravitational waves (GW) detectable by ground-based interferometers (Abadie et al. 2010), compact object (CO) mergers involving a neutron star (NS) are likely to emit a variety of electromagnetic (EM) signals. Immediately post-merger, the accretion of disrupted NS material onto the central black hole (BH) or hypermassive NS may drive a short gamma ray burst (Paczynski 1986; Eichler et al. 1989a; Narayan et al. 1992). Mergers may also produce optical/infrared transients (Li & Paczyński 1998; Metzger et al. 2010; Roberts et al. 2011; Barnes & Kasen 2013) powered by the radioactive decay of heavy elements synthesized via rapid neutron capture (the r-process; Arnould et al. 2007). The r-process is expected to operate in material ejected from the system dynamically (Lattimer & Schramm 1974, 1976; Freiburghaus et al. 1999; Korobkin et al. 2012; Rosswog et al. 1999; Goriely et al. 2011), or unbound from a remnant accretion disk (Fernández & Metzger 2013; Perego et al. 2014; Just et al. 2015). On much longer timescales, the interaction of the ejecta with the interstellar medium will generate a radio signal (Nakar & Piran 2011).

Observing an EM counterpart will enhance the science returns of a GW detection (Metzger & Berger 2012) by identifying the host galaxy and the position of the merger within the host (Nissanke et al. 2013b; Kasliwal & Nissanke 2014; Holz & Hughes 2005; Dalal et al. 2006), constraining the neutron star equation of state (Bauswein et al. 2013; Hotokezaka et al. 2013b; Bauswein et al. 2015), and confirming low signal-to-noise GW events (Kochanek & Piran 1993; Harry & Fairhurst 2011). Among possible counterparts, the radioactive transients—known as "kilonovae"—are especially promising. Kilonova emission is roughly isotropic (Roberts et al. 2011; Bauswein et al. 2013), and peaks on timescales of days–weeks post-merger (Barnes & Kasen 2013; Tanaka & Hotokezaka 2013; Grossman et al. 2014), making it ideal for EM follow-up of a GW trigger. Because kilonovae derive their energy from radioactive decay, they probe nucleosynthesis in the merger in a way other counterparts cannot, and may therefore constrain the astrophysical origin of r-process element production.

Accurate models of kilonova photometry are crucial for dual detection efforts. Unfortunately, the exotic composition of the heavy element ejecta, and uncertainties in r-process nucleosynthesis and decay, pose challenges to radiation transport simulations required to build these models. Recent work (Kasen et al. 2013) clarified the opacity of r-process material, reducing a major uncertainty in kilonova radiation transport simulations, but other key inputs remain relatively unconstrained.

Any rigorous kilonova model must address the following aspects of radioactivity: *i*) the total amount of radioactive energy released; *ii*) the decay channels that dominate the energy production during different phases of kilonova evolution; and *iii*) the efficiency with which suprathermal radioactive decay products— β-particles, α-particles, γ-rays, and fission fragments—transfer their energy to the thermal background. Once thermalized, the energy is re-radiated as thermal emission, powering the kilonova light curve.

Although thermalization determines the kilonova's luminosity, and is thus essential for light curve modeling, no detailed calculation of thermalization efficiencies has been attempted. Metzger et al. (2010) presented analytic estimates of thermalization, but focused on timescales shorter than those now believed to characterize kilonova light curves. Hotokezaka et al. (2016) studied γ-ray deposition in kilonovae, but did not investigate the thermalization of charged particles, which carry a large fraction of the radioactive energy.

Modeling the thermalization of r-process decay energy in the kilonova ejecta is challenging. Thermalization rates are sensitive to the ejecta's mass, velocity, and composition, as well as its magnetic field structure, which has not been definitively determined by magnetohydrodynamic simulations. The broad range of elements synthesized by the r-process, and the often unknown properties of the heaviest of those elements, complicates the situation, as does the complexity of the net emission spectrum, which is a sum over several decay chains, each evolving on its own timescale.

This paper addresses the issues outlined above, with special emphasis on the key physical processes influencing the thermalization of r-process decay products in kilonovae. In §3.2, we describe our ejecta model and its uncertainties. Section 3.3 defines energy loss rates for β-particles, α-particles, γ-rays, and fission fragments, and explores their sensitivity to ejecta parameters. Analytic estimates and analytic expressions for thermalization efficiencies are developed in §3.4. In §3.5, we present detailed numerical calculations of time-dependent thermalization efficiencies $f(t)$ for individual species and for the system as a whole, and discuss the sensitivity of $f(t)$ to properties of the ejecta. Finally, §3.6 evaluates the effect of thermalization on kilonova light curves, and uses improved light curve models to estimate the mass ejected by the claimed kilonova associated with GRB 130603B.

3.2 Properties of the kilonova ejecta

3.2.1 Ejecta model

Predictions of kilonova outflows vary, due to natural diversity in the merging systems (e.g. different mass ratios, BHNS v. NS^2) and uncertainties in the NS EOS. Recent hydrodynamic simulations (Bauswein et al. 2013; Hotokezaka et al. 2013b; Kyutoku et al. 2015; Sekiguchi et al. 2016) suggest that mergers dynamically eject between $\sim 10^{-4}$ and a few $\times 10^{-2}$ $M_\odot$ of material, with bulk velocities of a few tenths the speed of light. Additional material ($\sim 10^{-3} - 10^{-2} M_\odot$) can exit the system at slightly lower velocities ($0.05c - 0.1c$) as a wind from an accretion torus (Fernández & Metzger 2013; Perego et al. 2014; Fernández et al. 2015; Just et al. 2015).

We adopt as our fiducial model a system with $M_{\rm ej} = 5 \times 10^{-3}$ $M_\odot$ and $v_{\rm ej} = 0.2c$, where $v_{\rm ej}$ is defined in terms of the explosion kinetic energy, $E_{\rm k} = M_{\rm ej} v_{\rm ej}^2/2$. Since denser ejecta configurations thermalize more efficiently than diffuse systems, we vary these parameters over the ranges $M_{\rm ej}/M_\odot \in [10^{-3}, 5 \times 10^{-2}]$ and $v_{\rm ej}/c \in [0.1, 0.3]$.

We assume the ejecta is spherical and expanding homologously, and that the density profile follows a broken power-law, declining with velocity coordinate $v = r/t$ as $v^{-\delta}$ in the inner regions of the ejecta, and v^{-n}, $n > \delta$, in the outer regions. We set $\delta = 1$ and $n = 10$.

Barnes & Kasen (2013) provides a complete mathematical description of the density profile.

3.2.2 Magnetic fields

Kilonova ejecta contain a residual magnetic field, either inherited directly from the parent neutron star(s), or seeded by amplified fields produced by turbulence during the merger or in the resultant accretion disk (Kiuchi et al. 2014, 2015). Though weakened by expansion, the fields remain strong enough to influence charged particle motion. In a sufficiently strong field, charged particles have Larmor radii smaller than the coherence length of the magnetic field, and their motion is confined to "flux tubes" that trace the field lines.

If magnetic flux is frozen into the homologously-expanding ejecta, the field strength is related to the ejecta radius $R_{\rm ej} = v_{\rm ej}t$ by

$$B(t) \approx \frac{B_0 R_0^2}{R_{\rm ej}^2} \approx 3.7 \times 10^{-6} B_{12} R_6^2 v_2^{-2} t_{\rm d}^{-2} \text{ G}, \tag{3.1}$$

where $v_2 = v/0.2c$, $t_{\rm d}$ is the elapsed time in days, and B_0 and R_0 are the magnetic field and radius at the time of mass ejection. The quantities $B_{12} = B_0/10^{12}$ G and $R_6 = R_0/10^6$ cm have been scaled to typical values; $R_0 \approx 10^6 - 10^7$ cm is characteristic of the size of NSs or the post-merger accretion disk, and B_0 may range from $10^9 - 10^{15}$ G, depending on the initial NS fields and the efficiency of magnetic field amplification.

A relativistic particle of mass m, charge q, kinetic energy E, and velocity v in a magnetic field B has a maximum Larmor radius (when $\mathbf{v} \perp \mathbf{B}$) of

$$r_{\rm L,max} = \frac{(E + mc^2)v}{qBc},$$

Assuming typical emission energies of $E_{\beta,0} = 0.5$ MeV for β-particles, $E_{\alpha,0} = 10$ MeV for α-particles, and $E_{\rm ff,0} = 150$ MeV for fission fragments, and assuming fission fragments are singly ionized and have masses of $\sim 130\ m_{\rm u}$, with $m_{\rm u}$ the atomic mass unit, the Larmor radii are

$$\frac{r_{\rm L,max}(t)}{R_{\rm ej}(t)} = \begin{cases} 1.5 \times 10^{-6}\ v_2 t_{\rm d} B_{12}^{-1} R_6^{-2} & \beta\text{-particles} \\ 2.4 \times 10^{-4}\ v_2 t_{\rm d} B_{12}^{-1} R_6^{-2} & \alpha\text{-particles} \\ 1.0 \times 10^{-2}\ v_2 t_{\rm d} B_{12}^{-1} R_6^{-2} & \text{fiss. fragments.} \end{cases} \tag{3.2}$$

We will adopt the flux tube approximation for all particles. This is clearly appropriate for α- and β-particles, which have $r_{\rm L}/R_{\rm ej} \ll 1$ for the duration of the kilonova. Fission fragments may, at later times, have $r_{\rm L}$ large enough that they jump from field line to field line. We discuss this possibility in A.3.2, but do not employ models of fission fragment transport beyond the flux tube approximation in this work.

The magnetic field structure determines charged particle trajectories and so affects thermalization. Radial fields can escort fast charged particles straight out of the ejecta, reducing thermalization. In contrast, toroidal or tangled fields trap charged particles, and so enhance thermalization. We consider three types of configurations here: radial ($\mathbf{B} \propto \hat{\mathbf{r}}$), which may be produced by the outward motion of the ejecta "combing" out the field lines; toroidal ($\mathbf{B} \propto \hat{\boldsymbol{\phi}}$), perhaps created by the spiral motion of neutron stars shedding mass through tidal stripping; and random, which may be generated by turbulent motions in the material during mass ejection. To model the latter case, we assume field lines re-orient on a length scale $\lambda R_{\rm ej}$, where the dimensionless parameter $\lambda < 1$.

3.2.3 Composition

The ejecta composition impacts thermalization in two ways. First, it determines the partition of radioactive energy among different decay channels, and the energy spectra of the decay products. Second, it sets the properties of the background material (e.g., isotope mass, atomic number, and ionization energy) which influence the energy loss rates of the decay products.

To determine the ejecta composition, we calculate r-process nucleosynthesis on a set of smoothed-particle hydrodynamics (SPH) trajectories extracted from a relativistic simulation of an equal-mass ($1.35\ M_\odot$-$1.35\ M_\odot$) NS^2 merger (Goriely et al. 2011). At the start of the nucleosynthesis calculation, all trajectories had temperatures of 6 GK, densities set by their hydrodynamical histories, compositions determined by nuclear statistical equilibrium, and initial electron fractions $Y_{\rm e,0}$ between 1.5×10^{-2} and 5.5×10^{-2}. These quantities were then evolved according to the reaction network, which tracks charged particle reactions, neutron capture, photo-dissociation, β- and α-decay, and fission, for more than 7300 nuclei. (For a detailed description of the network, see Mendoza-Temis et al. 2015).

The hydrodynamical model predicts two classes of trajectories that produce two distinct compositions: "slow" trajectories, where all free neutrons are depleted by neutron-capture, and "fast" trajectories, where early rapid expansion precludes the capture of all neutrons by seed nuclei (see also: Just et al. 2015; Goriely et al. 2014; Metzger et al. 2015; Mendoza-Temis et al. 2015). The slow trajectories comprise $\sim 90\%$ of the ejecta, and robustly produce r-process elements up to the third peak. The fast ejecta r-pattern is different from the slow component due to the longer neutron-capture timescale. In constructing our ejecta model, we assume that at times relevant for thermalization, material from slow trajectories will be located in the ejecta's interior regions (henceforth "inner ejecta"), while material from the fast trajectories occupies the outer regions ("outer ejecta"). We sum the trajectories in each class to construct mass-integrated inner and outer compositions. We also select a representative case from the set of inner trajectories, which typifies conditions in the merger ejecta. We use this representative trajectory to study the details of the radioactivity.

The top panel of Figure 3.1 shows the inner ejecta composition at $t = 1$ day, based on neutron-capture and photodissociation rates computed using the statistical model for four different nuclear mass models: the Finite Range Droplet Model (FRDM; Möller et al. 1995), the Hartree-Fock-Bogoliubov model HFB21 (Goriely et al. 2010), the Weizsäcker-Skyrme model (WS3; Liu et al. 2011), and the Duflo-Zucker model with 31 parameters (DZ31; Duflo

& Zuker 1995). We find that although the abundance pattern is similar for different mass models, particularly around $A \sim 130$ due to fission cycling, the position of the peak at $A \sim 195$ and the abundances for $A \gtrsim 195$ depend on the mass model. The differences in the translead abundances impact the late time kilonova light curves, as will be discussed in §3.6.4.

The abundances are also influenced by the electron fraction $Y_{\rm e,0}$ at the onset of the r-process; neutron scarcity (high $Y_{\rm e,0}$) suppresses the assembly of the heaviest r-process elements. Our SPH trajectories are all initially very neutron rich; however, weak interactions in the aftermath of a merger could raise $Y_{\rm e,0}$ substantially (Wanajo et al. 2014; Sekiguchi et al. 2015; Goriely et al. 2015). To explore this effect, we artificially increased the initial $Y_{\rm e,0}$ of our representative trajectory from its value of 0.04, and reran the nuclear reaction network. As expected, higher initial electron fractions produce fewer heavy elements (bottom panel of Figure 3.1) and for $Y_{\rm e,0} \gtrsim 0.2$ the r-process fails to reach the third peak, instead producing material with $A \sim 70 - 110$.

The ejecta composition evolves with time as neutron-rich isotopes gradually decay to stability. However, on timescales relevant for kilonova light curves ($t \sim 0.1 - 10$ days), this evolution is fairly slow, and driven primarily by α- and β-decays, which do not dramatically change the abundance-averaged properties of the composition. For the purpose of calculating energy loss rates, we therefore assume that the abundance-averaged properties are constant in time, but vary in space, with the inner 90% (outer 10%) of the mass described by the average abundance pattern of the inner (outer) trajectories, calculated at $t = 1$ day using the FRDM mass model. The outer ejecta differs from the inner ejecta primarily in its high abundance of hydrogen, produced by the decay of remnant free neutrons to protons.

3.2.4 Radioactivity

The energy generation rate from r-process decay has been shown to approximately follow $\dot{\epsilon} = \epsilon_0 t_{\rm d}^{-\eta}$, with $\epsilon_0 \approx 10^{11}$ ergs s^{-1}g^{-1} and $\eta = 1.1 - 1.4$ (Metzger et al. 2010; Roberts et al. 2011; Goriely et al. 2011; Korobkin et al. 2012). However, the fraction of the energy supplied by each decay channel, and the emission spectra for each decay product, are less clear.

Though r-process radioactivity is most commonly associated with β-decay, any translead nuclei synthesized will decay by α-emission, and heavier ($A \gtrsim 250$) nuclei may undergo fission, trends which have implications for thermalization. Radioactive emission in kilonovae will at all times be dominated by isotopes with half-lives $\tau_{1/2}$ of order $t_{\rm exp}$, the time since explosion. For any particular decay channel, $\tau_{1/2}$ is strongly correlated with the energy Q emitted when a nucleus decays. However, this is not true across decay channels; for a given $\tau_{1/2}$, β-decay has lower Q than α-decay, which has lower Q than fission. As a result, α-decay can generate a substantial fraction of the r-process radioactive energy, even though r-process yields are dominated by nuclei that β-decay. Fission could, in principle, also be an important source of energy, but we find almost all fissioning nuclei have $\tau_{1/2}$ less than a day, suggesting that fission supplies a negligible amount of energy after very early times. Since energy from α-decay thermalizes with a different efficiency than β-decay energy, thermalization depends

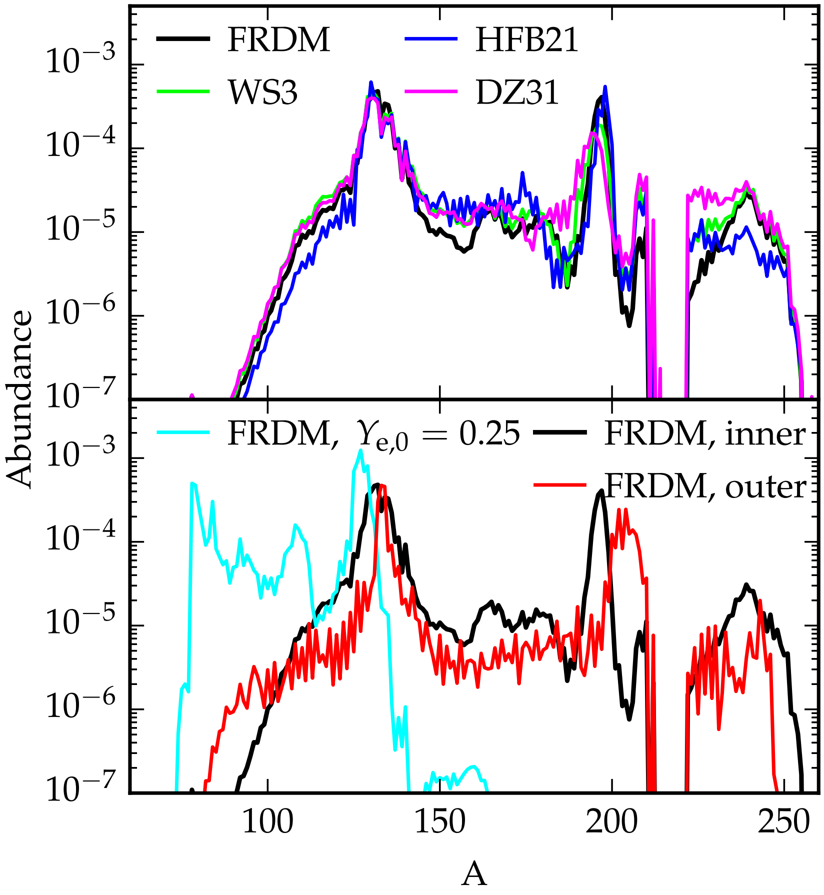

Figure 3.1: Abundance yields from our nuclear network calculations at $t = 1$ day. *Top panel:* Mass-integrated abundances from the "inner" ejecta ($\sim$ 90% of the ejected mass) for four nuclear mass models. The r-process proceeds past the third peak, and strong fission cycling reduces differences among nuclear mass models. *Bottom panel:* An illustration of major factors affecting the final abundances. The red curve shows mass-integrated abundances for the "outer" ejecta, using the FRDM mass model. Rapid expansion hinders free neutron capture, decreasing heavy element production, and creating a substantial amount of H as uncaptured neutrons decay to protons. The cyan curve shows the abundance yield of a representative inner ejecta trajectory, whose initial electron fraction has been artificially increased to $Y_{e,0} = 0.25$, leading to limited production of nuclei with $A > 130$.

on the relative importance of these decay channels, and thus on the yields of translead nuclei.

The top panel of Figure 3.2 shows the fraction of radioactive energy produced by α-decay, β-decay, and fission, for the representative trajectory introduced in 3.2.3, calculated for four nuclear mass models. Beta-decay is the primary source of energy for all mass models out to late times. Fission, including β-delayed, neutron-induced, and spontaneous fission, contributes $\sim 10\%$ of the energy at times $\lesssim 1$ day, and α-decay becomes significant within a few hours. The fractions for the different nuclear mass models generally agree with each other, but the estimates of energy generated by α-decay differ by a factor of almost ten, with DZ31 predicting the largest contribution from α-decay and FRDM predicting the least. Since α-decays release more energy, per decay, than β-decay, the enhanced role of α-decay predicted by the DZ31 model also results in an increase in the total energy generated by the decay of r-process isotopes. The increase is modest early on (a factor of $\lesssim 1.2$ for $t \leq 1$ day) but becomes more important at late times (a factor of $\gtrsim 2$ by $t = 1$ month.)

The bottom panel of of Figure 3.2 explores the effect of electron fraction on the decay channels. Fission and α-decay are significant sources of energy for $t \lesssim 1$ day and $t \gtrsim 1$ day, respectively, for ejecta with $Y_{\rm e,0} \lesssim 0.2$, but become negligible at higher $Y_{\rm e,0}$ because the reduced number of free neutrons chokes the production of the heaviest nuclei.

3.2.5 Emission Spectra of Decay Products

Modeling the energy spectra of r-process radioactive decay products is complicated by the large number of decay chains and the uncertain nuclear data. However, we can construct approximate spectra by considering emission from a range of contributing decays. We calculate emission spectra using the time-dependent composition of our representative inner SPH trajectory. The decay energies for α- and β-decay were determined from experimental mass excesses (AME 2012; Audi et al. 2012; Wang et al. 2012) when available, and theoretical (FRDM) mass excesses otherwise. Decay data, including β endpoint energies, γ-spectra, and half-lives for β- and α-decay, were retrieved from the Nuclear Science References database (Pritychenko et al. 2011), accessed via the website of the International Atomic Energy Agency.

Beta decay

Energy from β-decay takes the form of energetic β-particles, γ-rays, and neutrinos. (Beta-delayed fission is treated as part of fission, and we neglect β-delayed neutron- and α-emission, as they are expected to be negligible for nuclei with lifetimes longer than a day.) Following β-emission, nuclear de-excitation can also emit low-energy atomic electrons, delayed neutrons, and $\sim$ keV X-rays, but we found that these secondary processes were negligible.

We constructed β- and γ-spectra using selected isotopes that dominated the β-decay energy production. The energy generation rate of an isotope i was estimated as $\dot{\epsilon}_{\beta,\rm i} = Y_{\rm i} Q_{\beta,\rm i}/\tau_{1/2,\rm i}$, where $Y_{\rm i}$ is the number abundance of the isotope, $Q_{\beta,\rm i}$ the decay energy, and $\tau_{1/2,\rm i}$ the half life. We used experimental values for Q_β and $\tau_{1/2}$ when available, and theoretical

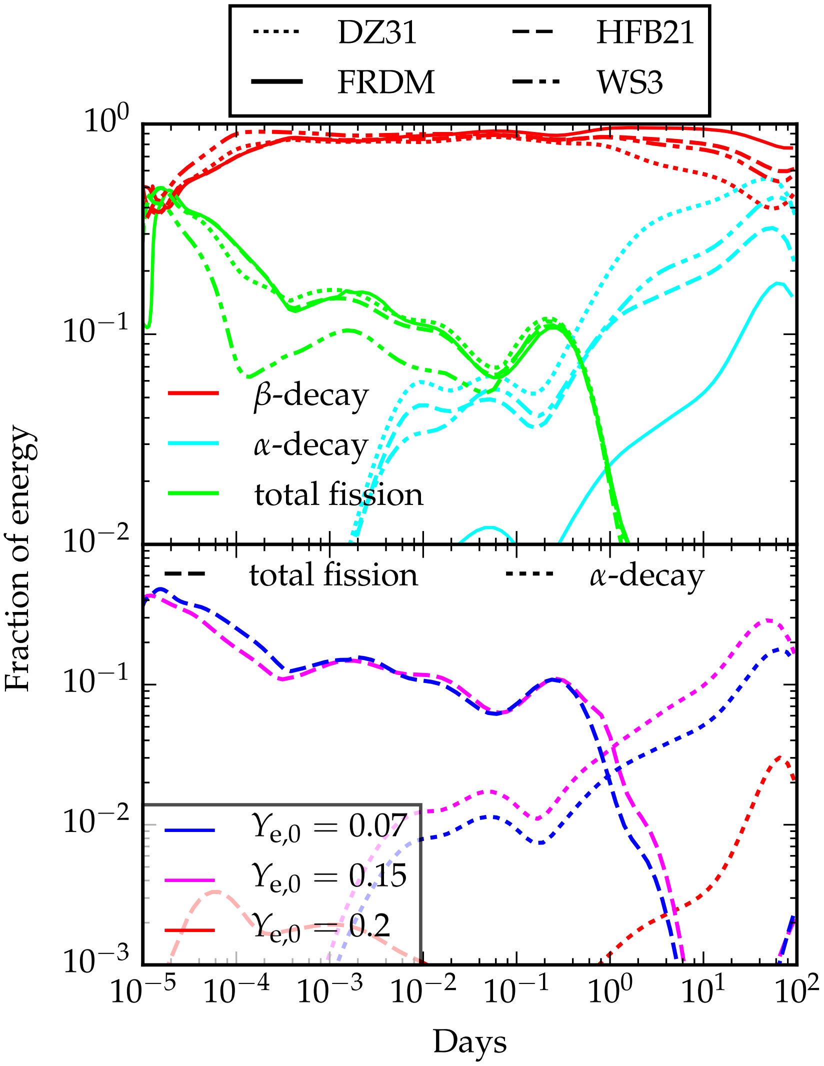

Figure 3.2: *Top panel:* The fraction of the total radioactive energy produced by β-decays, α-decays, and fission in our representative trajectory, for four nuclear mass models. While β-decay dominates, fission (α-decay) can be important at early (late) times. Agreement between the four mass models studied is within an order of magnitude. *Bottom panel:* Energy released in α-decays and fission, for the FRDM mass model, for a range of $Y_{e,0}$. Lower electron fractions favor the assembly of the heavy elements that later decay by fission and α-emission. As $Y_{e,0}$ increases, these processes become less important, and are negligible for $Y_{e,0} > 0.2$.

values otherwise. We excluded isotopes lacking decay data and those with heating rates less than 1% of the maximum single-isotope heating rate. The excluded β-decays account for only 5-7% of the total β-decay energy at all times. The γ-ray intensities were taken directly from nuclear measurements, while β-spectra were constructed from endpoint energies and intensities assuming all decays had an allowed spectral shape and using the simplified Fermi formula fit proposed by Schenter & Vogel (1983).

We find that roughly 20% of the β-decay energy emerges as β-particles, 45% as γ-rays and 35% as neutrinos. The energy lost to neutrinos, which escape the ejecta without depositing any energy, sets an upper limit of $\sim 65\%$ on the β-decay thermalization efficiency. The top two panels of Figure 3.3 show the β- and γ- spectra for the composition of our neutron-rich representative SPH trajectory for $t = 1 - 30$ days. The γ-ray spectra peak at several hundred keV and the β-spectra at around 0.5 MeV.

The β-spectrum was found to be consistent across mass models, which is not surprising since β-decay energy is very sensitive to half-life, and β-emission at all times is dominated by nuclei with half-lives of order the time since explosion. However, we did find the spectrum depends mildly on electron fraction, with higher $Y_{\rm e,0}$ slightly enhancing the spectrum's high-energy tail.

This is due to differences in how β-decay energy is divided among β-particles, γ-rays, and neutrinos. Compositions evolved from higher initial $Y_{\rm e}$ impart a greater *fraction* of the total β-decay energy Q_β to β-particles, at the expense of γ-rays (see the lower three panels of Figure 3.4). As shown in Figure 3.1, higher electron fractions yield compositions with lower A. The β-decays for these lighter nuclei tend to be dominated by one or a few transitions to low-lying nuclear energy states; the energy carried away by the β-particle and the neutrino is close to Q_β, and the energy released in γ-rays during nuclear de-excitation is reduced. In contrast, for more massive nuclei, the excitation energy of the daughter nucleus after emission of the β-particle and neutrino is more likely to be a significant fraction of Q_β, and a greater portion of the energy takes the form of γ-rays. Therefore, despite having similar Q_β, nuclei synthesized in high-$Y_{\rm e,0}$ conditions generate more energetic β-particles. We found these effects to be independent of mass model.

Alpha decay

While the majority of species produced by the r-process stabilize through β-decay, some heavier isotopes ($A \gtrsim 200$) undergo α-decay. Unlike β-particles, α-particles are ejected from nuclei at discrete energies that fall within the fairly narrow range $E_\alpha \sim 5 - 9$ MeV. Due to the fact that alpha decay is a tunneling process, α-particles carry all of the decay energy in the majority of decays, and the incidence of γ-emission is vanishingly low.

We determined the most important sources of α-emission using the procedure detailed above for β-decays. The α-spectrum as a function of time is given in the bottom panel of Figure 3.3. The energy is fairly evenly distributed in the range 5 MeV $< E_\alpha <$ 9 MeV.

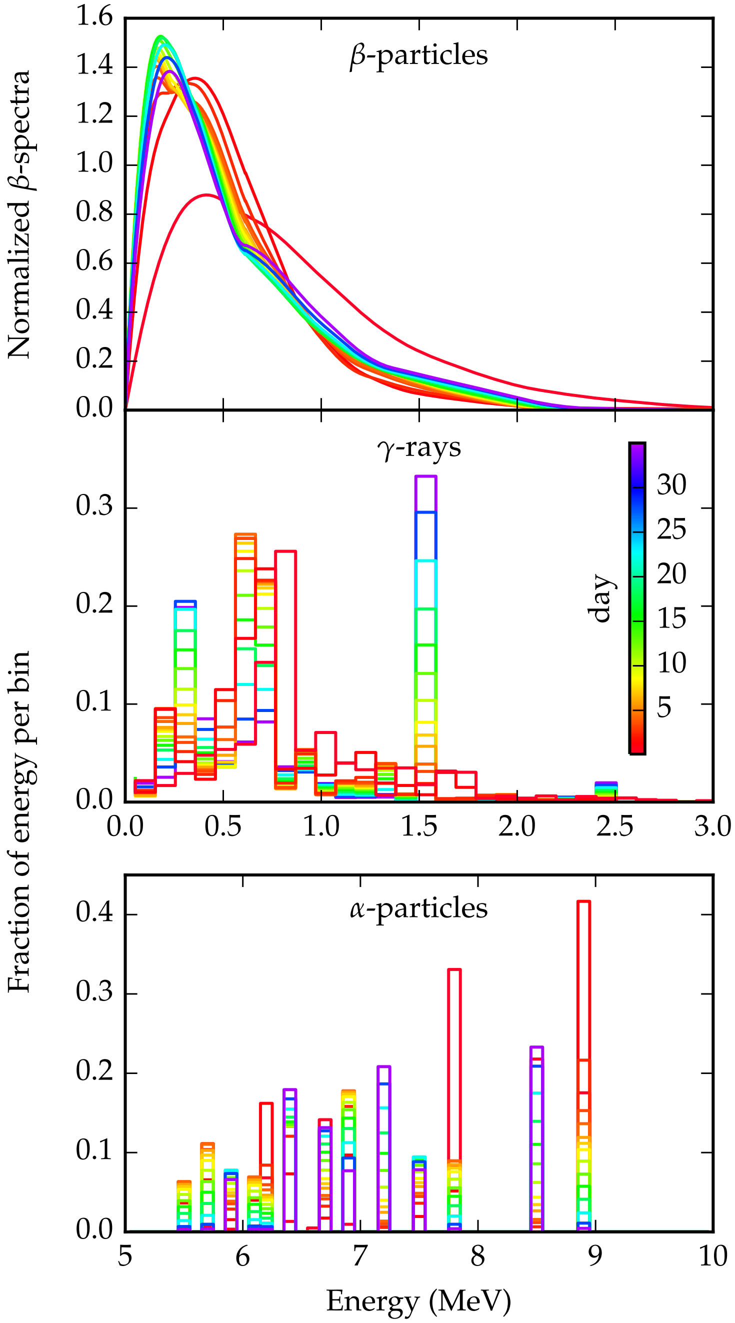

Figure 3.3: The emission spectra for β-particles (top panel), γ-rays (middle panel), and α-particles (bottom panel) as a function of time.

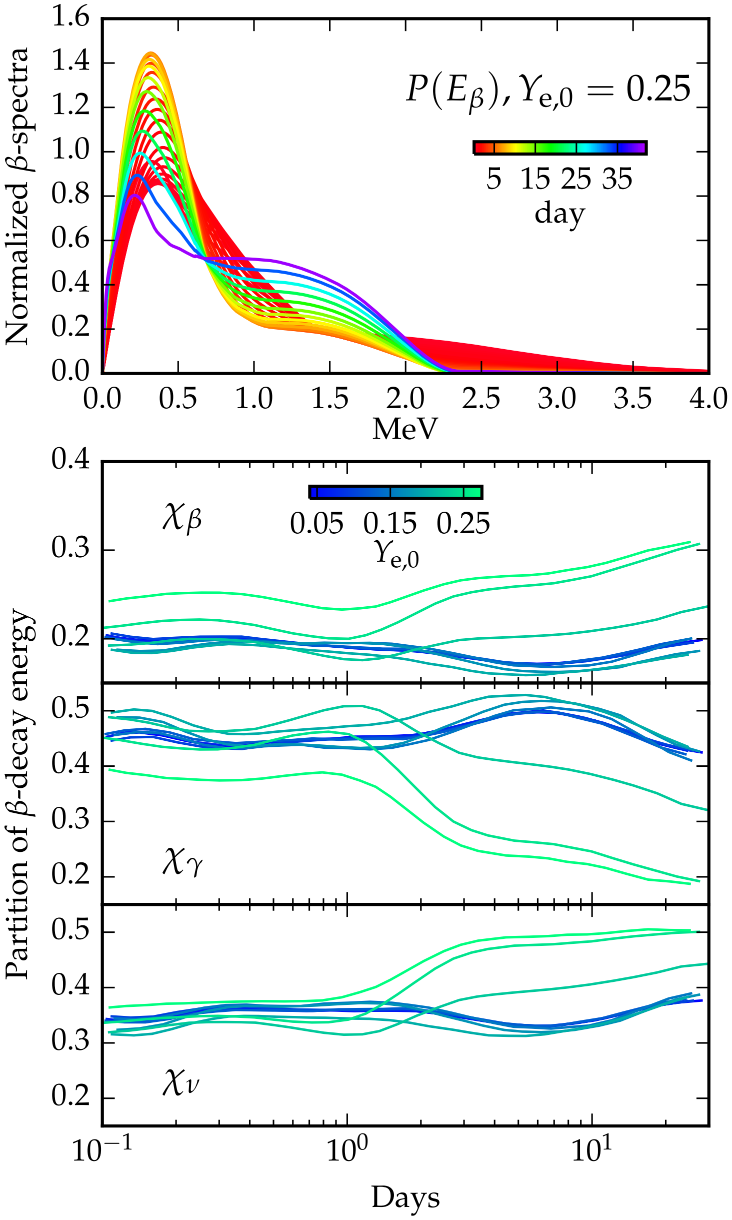

Figure 3.4: The effect of electron fraction $Y_{e,0}$ on β-decay for the FRDM nuclear mass model. (Other nuclear mass models studied showed similar trends). *Top panel:* The β-spectrum for a composition with $Y_{e,0} = 0.25$. The spectrum is shifted to higher energies, relative to the low-$Y_{e,0}$ case (Figure 3.3). *Bottom panels:* The fraction of Q_β, χ, imparted to β-particles, γ-rays, and neutrinos, for different values of $Y_{e,0}$. As $Y_{e,0}$ increases, a greater fraction of Q_β goes to β's and neutrinos, while χ_γ shrinks. This effect is particularly pronounced at late times.

Fission

Spontaneous, neutron-induced, and β-delayed fission of heavy nuclei ($A \gtrsim 250$) contribute a few percent of the total r-process radioactive decay energy at times $\lesssim 1$ day. The mass distribution and energy spectra of the fission fragments depend sensitively on the nuclear physics models, and a thorough exploration of these parameters is beyond the scope of this work. We can, however, estimate the final kinetic energy of fission as equal to the repulsive Coulomb energy between the daughter nuclei immediately after fission occurs:

$$E_{\mathrm{K,tot}} = E_{\mathrm{Coul}} = \frac{Z_1 Z_2 e^2}{r_0 \left(A_1^{1/3} + A_2^{1/3}\right)}, \tag{3.3}$$

where e is the elementary charge, (A_1, Z_1) and (A_2, Z_2) are the masses and atomic numbers of the daughter nuclei, and the nuclear radius is given by $r_0 A^{1/3}$. For deformed post-scission nuclei, $r_0 \simeq 1.8$ fm.

Fission favors the production of nuclei at or near the doubly-magic nucleus $(A, Z) = (132, 50)$. Assuming a typical parent isotope has mass and atomic numbers $A_p = 250$ and $Z_p = 100$, and that $(A_1, Z_1) = (132, 50)$, the fission daughters will have kinetic energies of order 100 MeV. We assume the fission fragment spectrum is flat, and ranges from 100–150 MeV. Given the limited role of fission at times later than 1 day, a more detailed treatment is unnecessary.

3.3 Thermalization Physics

In this section, we discuss the processes by which energetic decay products thermalize in the kilonova ejecta, and present energy loss rates for β-particles, α-particles, and fission fragments.

3.3.1 Gamma-rays

Gamma-rays lose energy through photoionization and Compton scattering. We calculated the Compton opacity from the Klein-Nishina formula and the photoionization opacity using the Photon Cross Section Database (*XCOM*; Berger et al. 2010) published by the National Institute of Standards and Technology (NIST).

The total γ-ray opacity for our fiducial composition at $t = 1$ day is shown in Figure 3.5. The high-Z elements produced in the r-process have higher ionization thresholds (~ 100 keV) than do the metals in typical astrophysical mixtures, so the photoionization cross-section in kilonovae dominates out to ~ 1 MeV, above which Compton scattering takes over. The opacity varies little between the inner and outer ejecta, and changes over time are minor, so we assume the γ-ray opacity to be constant.

Both photoionization and Compton scattering events produce a non-thermal electron, which loses energy by the physical processes described in the next section.

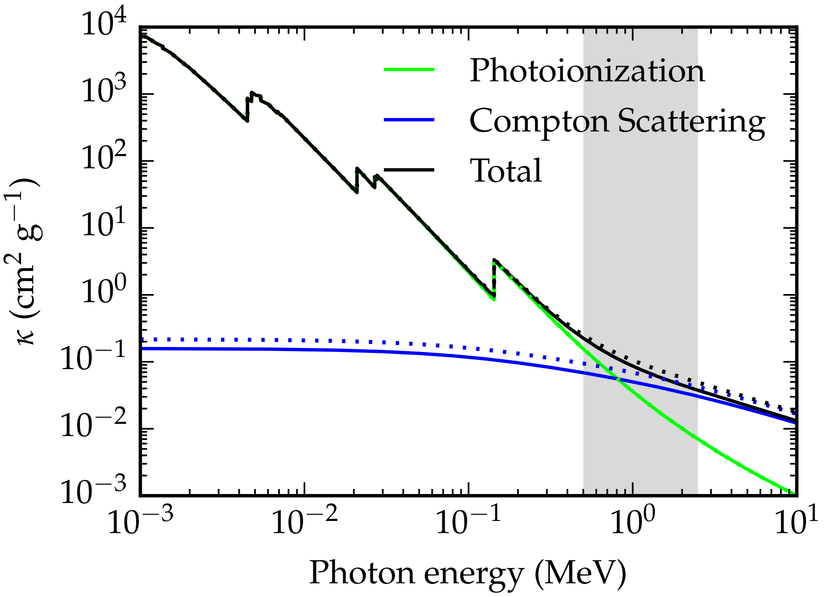

Figure 3.5: The γ-ray opacity, κ, in the inner (solid lines) and outer (dotted lines) ejecta. Photoionization opacity is plotted in green, Compton opacity in blue, and total opacity in black. Differences between the inner and outer ejecta compositions have a negligible impact on κ. The gray bar indicates the energies at which most γ-rays are emitted.

3.3.2 Beta particles

Suprathermal β-particles lose energy primarily through Coulomb interactions with free thermal electrons (plasma losses), and by exciting or ionizing bound atomic electrons. Bremsstrahlung (free-free) emission is important for very high-energy β-particles. While earlier studies of thermalization assumed plasma interactions dominated the energy loss, we find β-particles lose most of their energy to ionization and excitation.

In the limit that the β-particle energy far exceeds that of thermal electrons, the plasma energy loss per unit time is (Huba, J. D. 2013)

$$\dot{E}_{\beta}^{\rm pl} = 7.7 \times 10^{-15} E_{\beta}^{-1/2} \tag{3.4}$$

$$\times \left(\frac{n_{\rm e}}{1\ {\rm cm}^{-3}}\right) \lambda_{\rm ee} \left(1.0 - \frac{3.9}{7.7}\frac{T}{E_{\beta}}\right)\ {\rm MeV\ s}^{-1} \tag{3.5}$$

where E_{β} is the β-particle's kinetic energy in MeV, T is the ejecta temperature in MeV, $\lambda_{\rm ee} \sim 10$ is the Coulomb logarithm for electron-electron scattering, and $n_{\rm e}$ is the free electron number density. Radioactive β-particles have $E_{\beta} \sim 1$ MeV whereas $k_{\rm B}T \sim 1$ eV in kilonova ejecta, so the assumption that $E_{\beta} \gg k_{\rm B}T$ holds. We determine $n_{\rm e}$ assuming that all elements heavier than hydrogen are singly ionized, as expected for kilonova ejecta near peak brightness (Kasen et al. 2013). The outer ejecta contains a substantial quantity of hydrogen, which we assume to be neutral given the low temperatures ($T \lesssim 5000$ K) expected in the ejecta periphery.

We calculate energy losses due to ionization and excitation of atomic electrons using the well-established formula (Heitler 1954; Berger & Seltzer 1964; Gould 1975; Blumenthal & Gould 1970; see also Chan & Lingenfelter (1993) and Milne et al. 1999)

$$\dot{E}_\beta^{\rm IE} = \frac{2\pi r_{\rm e}^2 m_{\rm e} c^3 n_{\rm e,b}}{v_\beta/c} \times \left\{ 2\ln\left(\frac{E_\beta}{\bar{I}}\right) + \ln\left(1+\frac{\tau}{2}\right) + \left(1-\frac{v_\beta^2}{c^2}\right) g(\tau) \right\}, \tag{3.6}$$

$$g(\tau) = 1 + \frac{\tau^2}{8} - (2\tau+1)\ln 2, \tag{3.7}$$

where $r_{\rm e}$ is the classical electron radius, $m_{\rm e}$ is the electron mass, $n_{\rm e,b}$ is the number density of bound electrons, v_β is the β-particle's speed, and $\tau = E_\beta/m_{\rm e}c^2$. The quantity $\bar{I}$ is an average ionization and excitation potential which can be approximated for an element of atomic number Z as (Segré 1977)

$$\bar{I} = 9.1Z\left(1 + \frac{1.9}{Z^{2/3}}\right)\ \text{eV}. \tag{3.8}$$

Following Chan & Lingenfelter (1993), we use averaged quantities for $n_{\rm e,b}$ and $\bar{I}$,

$$\langle n_{\rm e,b} \rangle = \frac{\rho}{m_{\rm u}}\left\langle \frac{Z}{A} \right\rangle, \tag{3.9}$$

$$\left\langle \ln\frac{\bar{I}}{\rm eV} \right\rangle = \left\langle \frac{Z}{A} \right\rangle^{-1} \sum_{\rm j} \left(\frac{Z}{A}\right)_{\rm j} X_{\rm j} \ln\left(\frac{\bar{I}_{\rm j}}{\rm eV}\right), \tag{3.10}$$

$$\text{where} \quad \left\langle \frac{Z}{A} \right\rangle = \sum_{\rm j} \left(\frac{Z}{A}\right)_{\rm j} X_{\rm j}, \tag{3.11}$$

where $m_{\rm u}$ is the nuclear mass unit, $X_{\rm j}$ is the mass fraction of element j, and the sum runs over all species in the composition. For the inner (outer) ejecta, we find $\langle \ln \bar{I}/{\rm eV}\rangle = 6.4$ (4.9), and $\langle Z/A \rangle = 0.4$ (0.55).

Plasma and ionization/excitation losses are the cumulative results of many distant interactions that individually transfer very little energy. The thermal and bound electrons energized by β-particles through these channels have very low kinetic energies, and thermalize rapidly. Instead of tracking secondary electrons explicitly, we assume their kinetic energy is transferred directly to the thermal pool.

Bremsstrahlung (free-free) and synchrotron emission are other possible means of β-particle energy loss. The rate of cooling due to synchrotron emission in a magnetic field B is

$$\dot{E}_\beta^{\rm syn} = \frac{4}{9} r_{\rm e}^2 c \gamma^2 \left(\frac{v_\beta}{c}\right)^2 B^2, \tag{3.12}$$

where γ is the β-particle's Lorentz factor. Neglecting logarithmic terms (which only increase $\dot{E}_\beta^{\rm IE}$), and assuming $\langle Z/A \rangle = 0.4$ and $\gamma^2(v_\beta/c)^3 \approx 10$, we estimate the ratio of synchrotron to ionization/excitation losses as

$$\frac{\dot{E}_\beta^{\rm syn}}{\dot{E}_\beta^{\rm IE}} \sim 1.6 \times 10^{-15} \left(\frac{B_{\rm d}}{3.7 \times 10^{-6}\ {\rm G}} \right)^2 M_5^{-1} v_2^{-1} t_{\rm d}^{-1}, \tag{3.13}$$

where $M_5 = M_{ej}/(5 \times 10^{-3} M_\odot)$ and $B_{\rm d}$ is the magnetic field at 1 day. This is much less than unity for all parameters of interest, so we neglect synchrotron losses.

In contrast, Bremsstrahlung contributes, albeit modestly, to β energy loss for $E_\beta \gtrsim 1$ MeV. From Seltzer & Berger (1986),

$$\dot{E}_\beta^{\rm Brem} = n_{\rm i} v_\beta (E_\beta + m_{\rm e} c^2) Z^2 r_0^2 \alpha \phi_{\rm rad} \tag{3.14}$$

where n_i is the number density of the scattering species, α is the fine-structure constant, and $\phi_{\rm rad}$ are energy-dependent empirical fitting constants, also from Seltzer & Berger (1986). We model Bremsstrahlung losses in the inner ejecta using characteristic values $Z = 60$ and $A = 144$, similar to the average values of the inner composition. For the outer ejecta, we use a two component composition, with $(Z, A) = (1, 1)$ accounting for the high amount of hydrogen, and $(Z, A) = (55, 133)$ representing elements with $Z > 1$.

Bremsstrahlung may produce high-energy photons that do not thermalize promptly in the ejecta, an effect of order $\lesssim 10\%$ at typical β-particle energies. Our treatment of Bremsstrahlung is discussed in more detail in §A.3.

We plot the total energy loss rate in the inner and outer ejecta, normalized to mass density, in the top panel of Figure 3.6. While the lower degree of ionization in the outer ejecta makes plasma and Bremsstrahlung losses less efficient, this is more than compensated for by enhanced ionization and excitation losses due to the greater number of bound electrons per nucleon, and to the lower average ionization potential. Overall, thermalization rates in the outer ejecta are higher by a factor of a few.

3.3.3 Alpha-particles

Suprathermal α-particles thermalize by interacting with free and bound electrons. Long-range interactions with ions and short-range interactions with atomic nuclei do not significantly contribute to α-particle energy loss.

Alpha particles scattering off of free, thermal electrons lose energy at a rate given by Huba, J. D. (2013) for fast ions in a plasma,

$$\begin{aligned} \dot{E}_{\rm i}^{\rm pl} &= 1.7 \times 10^{-13} E_{\rm i}^{-1/2} \mu_{\rm i}^{1/2} Z_{\rm i}^2 \left(\frac{n_{\rm e}}{1\ {\rm cm}^{-3}} \right) \lambda_{\rm ie} \\ &\times \left(2 - \frac{1.1 \times 10^{-3}}{\mu_{\rm i}} - \frac{T}{E_{\rm i}} \right)\ {\rm MeV\ s}^{-1}, \end{aligned} \tag{3.15}$$

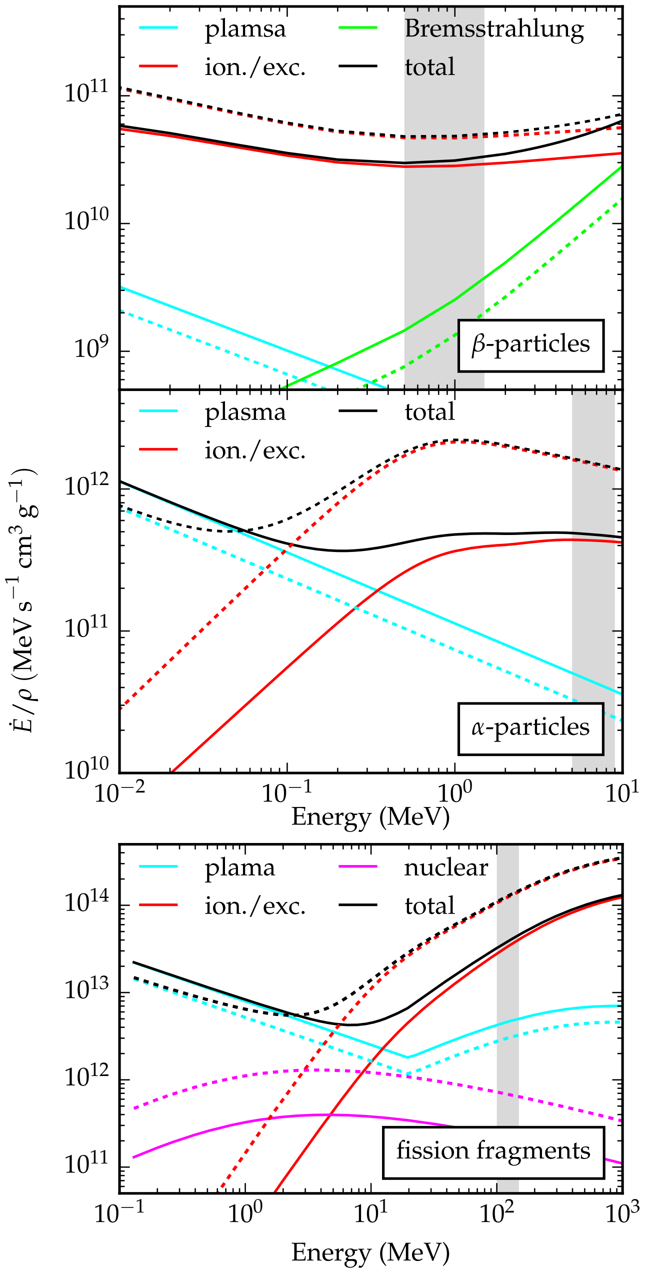

Figure 3.6: *All panels*: Energy loss rates in the inner (outer) ejecta are plotted in solid (dashed) lines. Gray bars indicate typical particle energies at emission. *Top panel:* The total energy loss rate for fast β-particles, normalized to the mass density ρ. Thermalization rates are higher in the outer ejecta by a factor of a few. *Middle panel:* The energy loss rates for α-particles in simplified r-process mixtures standing in for the full inner and outer ejecta compositions (see Figure 3.7), normalized to density. Alpha particle thermalization is a few to $\sim 10\times$ more efficient in the outer ejecta. *Bottom panel:* The energy loss rate for fission fragments, normalized to density and assuming most atoms in the ejecta are singly ionized. Thermalization is more efficient in the outer ejecta.

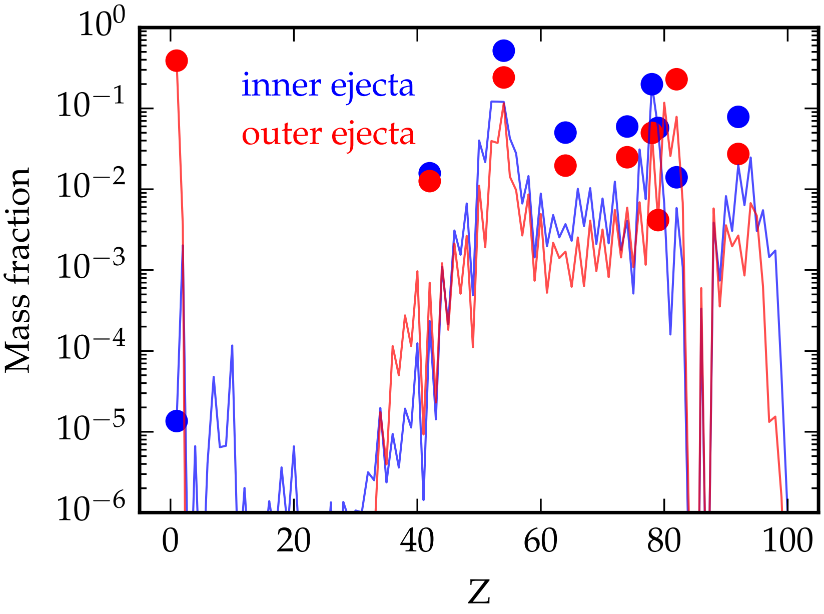

Figure 3.7: The simplified composition (circles) used to calculate the electronic stopping for α-particles and fission fragments. The full compositions, shown in solid lines, were mapped onto a composition of elements for which α- and proton stopping data were available through NISTS's *ASTAR* database.

where E_{i} is the ion's kinetic energy in MeV, μ_{i} is the ion mass in m_{u}, Z_{i} is the charge in units of the elementary charge, and $\lambda_{\mathrm{ie}} \sim 5 - 10$ is the Coulomb logarithm for ion-electron scattering. For α-particles, $Z_{\mathrm{i}} = 2$ and $\mu_{\mathrm{i}} = 4$.

The rates of α-particle energy loss due to interactions with bound electrons are taken from NIST's *ASTAR* database (Berger et al. 2005). Lacking α-particle stopping data for all elements in our r-process mixture, we map the full inner and outer compositions onto a reduced set of elements for which α-stopping powers are available (see Figure 3.7). The middle panel of Figure 3.6 shows the total α-particle energy loss rates. Plasma losses dominate for $E_{\alpha} \lesssim 1$ MeV, while interactions with bound electrons are important at higher energies. The thermalization rate in the outer ejecta is greater than in the inner ejecta by up to an order of magnitude.

3.3.4 Fission fragments

Interactions with free and bound electrons, and with atomic nuclei all contribute to fission fragment thermalization. The energy loss to thermal free electrons is described by Eq. 3.15, where Z_{i} depends on the ionization state of the fission fragment and the length scale of the collision. For impact parameters greater than the size of the interacting particles, the relevant charge is the total charge carried by the fragment, $Z_{\mathrm{ff,ion}} = Z_{\mathrm{nuc}} - N_{\mathrm{e^-,b}}$, where

$Z_{\rm nuc}$ is the fragment's atomic number and $N_{\rm e^-,b}$ is the number of bound electrons. At lower impact parameters, more of the nuclear charge is felt.

We calculate $Z_{\rm ff,ion}$ as a function of fission fragment energy $E_{\rm ff}$ using the formula of Schiwietz & Grande (2001) for ion charge state in a gaseous medium. Since fragments with $Z_{\rm ff,ion} \gtrsim 7$ deflect thermal electrons at impact parameters greater than the fission fragment radius, we set $Z_{\rm i} \rightarrow \max\{Z_{\rm ff,ion}(E_{\rm ff}), 7\}$. Fission fragments can scatter off thermal *ions* at much lower impact parameters, in which case the full nuclear charge is felt. The energy loss from these interactions is given by the nuclear stopping formula of Ziegler (1980).

To model the stopping of heavy particles by bound electrons, we adopt the technique of Ziegler (1980), in which the stopping power of a heavy particle in any material is proportional to the stopping power of a proton in the same material, with the constant of proportionality given by $Z^2_{\rm ff,ion}$. We calculate the stopping power for the same simplified composition used to model α-particle energy loss, using proton stopping powers extracted from NIST's *PSTAR* database (Berger et al. 2005).

The total energy loss rate for fission fragments is presented in the bottom panel of Figure 3.6. Interactions with bound electrons dominate the rate at high energies, while losses to free electrons become important at energies less than ~ 10 MeV. Thermalization rates in the outer composition are a factor of a few higher than in the inner composition.

3.4 Analytic Results

Before moving to detailed numerical calculations of kilonova thermalization, we consider simple analytic estimates of the relevant timescales and time evolution. This work extends the analytic treatments proposed by Metzger et al. (2010); Hotokezaka et al. (2016). Unless stated otherwise, our estimates describe thermalization in the "inner" composition, which typically makes up $\sim 90\%$ or more of the ejected mass.

3.4.1 Analytic estimates of thermalization timescales

The net thermalization of the energy from the radioactive decay of r-process material depends on the relative importance of each decay channel and on how efficiently the decay products thermalize in the ejecta. Energy loss rates depend on the density of the medium, so thermalization is also a function of $M_{\rm ej}$ and $v_{\rm ej}$. If we approximate the ejecta as a uniform density sphere of mass $M_{\rm ej}$ and kinetic energy $E_{\rm k} = M_{\rm ej} v_{\rm ej}^2/2$, the density is

$$\rho(t) \approx 7.9 \times 10^{-15} M_5 \, v_2^{-3} \, t_{\rm d}^{-3} \text{ g cm}^{-3}, \tag{3.16}$$

where again, $M_5 = M_{\rm ej}/5.0 \times 10^{-3} M_\odot$ and $v_2 = v_{\rm ej}/0.2c$. Thermalization becomes inefficient at a time, $t_{\rm ineff}$, when the timescale for a particle to thermalize becomes similar to the ejecta expansion timescale, $t_{\rm exp}$. The inefficiency time can be compared to the peak of the kilonova light curve,

$$t_{\rm peak} \sim \left(A \frac{M_{\rm ej}\kappa}{v_{\rm ej} c} \right)^{1/2} \simeq 4.3\; M_5^{1/2}\; v_2^{-1/2}\;\text{days}, \tag{3.17}$$

where κ is the opacity for optical/infrared light (we take $\kappa = 10$ cm^2 g^{-1}, appropriate for an r-process medium) and $A = 0.32$ is a scaling factor we estimate from kilonova radiation transport simulations (e.g. Barnes & Kasen 2013). If $t_{\rm ineff} < t_{\rm peak}$, thermalization will impact the kilonova light curve significantly.

γ-rays: Gamma rays stop thermalizing efficiently when they can escape the ejecta without undergoing any scatters or absorptions. This occurs when the optical depth $\tau \approx \rho \kappa_\gamma R_{\rm ej}$ falls below unity. For γ-rays with energies $E_\gamma \gtrsim 1$ MeV, the relevant opacity is the Compton opacity, $\kappa_{\rm C} \approx 5 \times 10^{-2}$ cm^2 g^{-1} while the photoionization opacity, $\kappa_{\rm PI} \gtrsim 1$ cm^2 g^{-1}, dominates for lower-energy photons. The ejecta becomes transparent ($\tau < 1$) to γ-rays at a time

$$t_{\rm ineff} \approx \begin{cases} 0.5\; M_5^{1/2}\; v_2^{-1}\;\text{days} & \text{for } E_\gamma \gtrsim 1\text{ MeV} \\ 2.3\; M_5^{1/2}\; v_2^{-1}\;\text{days} & \text{for } E_\gamma \lesssim 1\text{ MeV} \end{cases} \tag{3.18}$$

In both cases, inefficiency sets in before the kilonova light curve peaks,

$$\frac{t_{\rm ineff}}{t_{\rm peak}} \simeq \begin{cases} 0.12\; v_2^{-1/2} & E_\gamma \gtrsim 1\text{ MeV} \quad (3.19\text{a}) \\ 0.5\; v_2^{-1/2} & E_\gamma \lesssim 1\text{ MeV}. \quad (3.19\text{b}) \end{cases}$$

β -particles: The energy loss rate for β-particles, modulo mass density, has a fairly constant value $\dot{E}_\beta \simeq 4 \times 10^{10} \rho$ MeV s^{-1} over a broad range of energies (see Fig. 3.6). The thermalization time for β-particles is

$$\begin{aligned} t_{\rm th} &\approx \frac{E_{\beta,0}}{\dot{E}_{\beta,0}} = \frac{E_{\beta,0}}{4 \times 10^{10}\;\rho\;\text{MeV s}^{-1}} \\ &= 0.02 \left(\frac{E_{\beta,0}}{0.5\text{ MeV}} \right) M_5^{-1}\; v_2^3\; t_{\rm d}^3\;\text{days}, \end{aligned} \tag{3.20}$$

where $E_{\beta,0}$ is the initial β-particle energy.

Beta particles trapped in the ejecta fail to efficiently thermalize when $t_{\rm th} \gtrsim t_{\rm exp}$, which occurs at

$$t_{\rm ineff} \approx 7.4 \left(\frac{E_{\beta,0}}{0.5\text{ MeV}} \right)^{-1/2} M_5^{1/2}\; v_2^{-3/2}\;\text{days}. \tag{3.21}$$

For a typical initial energy, $t_{\rm ineff}$ is comparable to the rise time of the light curve,

$$\frac{t_{\rm ineff}}{t_{\rm peak}} \approx 1.7 \left(\frac{E_{\beta,0}}{0.5\text{ MeV}} \right)^{-1/2} v_2^{-1}. \tag{3.22}$$

If the magnetic field is radial or only slightly tangled, β-particles can escape the ejecta before they thermalize, and escape will significantly reduce the thermalization efficiency. The escape time is

$$t_{\rm esc} \simeq \frac{R_{\rm ej}(t)}{\lambda v_{\beta,\parallel}}, \tag{3.23}$$

where λR_{ej} is the coherence length of the magnetic field, $v_{\beta,\parallel}$ is the component of the β-particle velocity parallel to the field lines, and we have modeled the β's motion in a random field as a random walk of step size $\lambda R_{\rm ej}$. For a β-particle with $E_{\beta,0} = 0.5$ MeV and pitch angle 1 ($v_{\beta,\parallel} = v_\beta$), $t_{\rm esc}$ is less than $t_{\rm th}$ when

$$t \gtrsim \frac{3.5\ M_5^{1/2}\ v_2^{-1}}{\lambda^{1/2}}\ \text{ days.} \tag{3.24}$$

For radial fields ($\lambda = 1$), this is less than $t_{\rm peak}$, so escape is important for β-particle thermalization. In contrast, for disordered fields there is a degree of randomness above which β-particle escape cannot significantly impact the light curve. This limit is defined by the condition $t_{\rm th}(t_{\rm peak}) < t_{\rm esc}(t_{\rm peak})$. Again considering a 0.5 MeV β-particle, we find

$$t_{\rm th}(t_{\rm peak}) < t_{\rm esc}(t_{\rm peak}) \rightarrow \lambda \lesssim 0.8 v_2^{-1}. \tag{3.25}$$

Thus, high-energy β-particles are effectively trapped by even a slightly tangled magnetic field.

α-particles and fission fragments: Fission fragments and α-particles are emitted with greater energies than β-particles ($E_{\alpha,0} \simeq 6$ MeV; $E_{\rm ff,0} \simeq 100$ MeV), but have higher energy loss rates ($\dot{E}_\alpha(E_{\alpha,0}) \sim 5 \times 10^{11} \rho$ MeV s^{-1}; $\dot{E}_{\rm ff}(E_{\rm ff,0}) \sim 5 \times 10^{13} \rho$ MeV s^{-1}.) The efficiency of α-particle thermalization is similar to that of β particles, while fission fragments thermalize efficiently out to very late times:

$$\frac{t_{\rm ineff}}{t_{\rm peak}} \simeq \begin{cases} 1.8 \left(\dfrac{E_{\alpha,0}}{6\ \text{MeV}}\right)^{-1/2} v_2^{-1} & \alpha\text{-particles} \qquad (3.26) \\[2ex] 3.9 \left(\dfrac{E_{\rm ff,0}}{125\ \text{MeV}}\right)^{-1/2} v_2^{-1} & \text{fiss. fragments.} \qquad (3.27) \end{cases}$$

Unlike β-partices, both α's and fission fragments have velocities much lower than $v_{\rm ej}$, and so in general cannot escape the ejecta. However, because these particles are propagating through a steep velocity gradient, their speed relative to the background gas continually decreases. This reduces the kinetic energy of the particles as measured in the co-moving frame. Because the particles have a spiraling motion about magnetic field lines, their motion is never completely frozen out in the fluid frame. Still, these "frame-to-frame" effects can reduce thermalization by $\lesssim 15\%$.

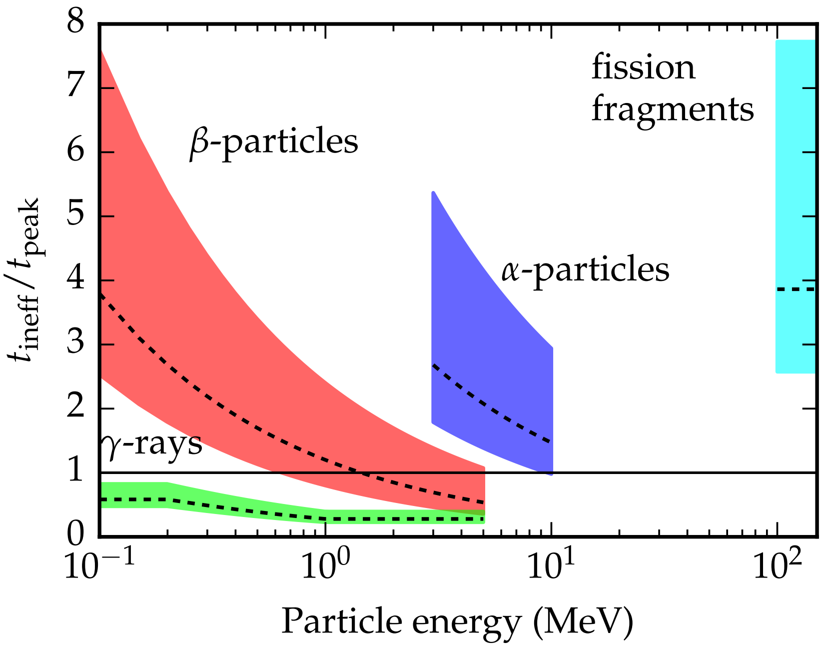

Figure 3.8: The ratio $t_{\mathrm{ineff}}/t_{\mathrm{peak}}$ for all particles, for v_{ej} in the range $0.1c - 0.3c$. Fission fragments, and to a lesser extent α-particles and low-energy β-particles, thermalize efficiently out to late times. Higher energy β's and γ-rays are expected to become inefficient on kilonova timescales. The width of the curves is due to the range of v_{ej} considered, since $t_{\mathrm{ineff}}/t_{\mathrm{peak}}$ varies inversely with v_{ej}. Curves for the fiducial velocity $v_{\mathrm{ej}}= 0.2c$ are over-plotted in dotted black lines.

3.4.2 Summary of thermalization timescales

While low-energy β-particles, α-particles, and especially fission fragments typically thermalize efficiently at $t = t_{\mathrm{peak}}$, the thermalization at peak of high-energy β-particles and γ-rays is not robust. Figure 3.8 plots the ratio of thermalization time to light curve peak for all particles as a function of initial energy for a range of v_{ej}. For α- and β-particles, we calculated $t_{\mathrm{ineff}}/t_{\mathrm{peak}}$ from Eq.s 3.26 and 3.22. The γ-ray curve was calculated from Eq. 3.19a for $E_\gamma \leq 200$ keV, 3.19b for $E_\gamma \geq 1$ MeV, and a simple linear interpolation for intermediate E_γ. For fission fragments, we modified Eq. 3.27 slightly to account for the positive slope of $\dot{E}_{\mathrm{ff}}$ in the range $E_{\mathrm{ff}} = 100 - 150$ MeV. This renders $\dot{E}_{\mathrm{ff}}$ approximately constant, so the fission fragment curve is essentially flat.

3.4.3 Analytic thermalization model

We develop an analytic expression for time-dependent thermalization efficiencies of massive particles under the following assumptions: first, that the radioactive energy generation rate evolves as $t^{-\alpha}$ with $\alpha = 1.0$ (close to the expected values $\alpha = 1.1 - 1.4$); second, that the density in the ejecta is spatially uniform; third, that energy loss rates are independent of particle energy, and depend only on ρ; and fourth, that all particles of a given type are emitted at a single energy E_0. Despite these simplifications, we find our model agrees fairly well with the detailed numerical calculations to be presented in §3.5.

The thermalization efficiency is defined as the ratio of energy emitted by radioactive processes to energy absorbed by the ejecta at any time t,

$$f(t) = \frac{\dot{E}_{\rm th}(t)}{\dot{E}_{\rm rad}(t)}. \tag{3.28}$$

We approximate the radioactive energy generation rate by $\dot{E}_{\rm rad} = \dot{\epsilon}_0(t_0/t)$ with $\dot{\epsilon_0} = 10^{11} M_{\rm ej}$ ergs s^{-1} and $t_0 = 1$ day. Assuming charged particle thermalization depends only on mass density (which declines like t^{-3} in a homologous flow) the energy loss is

$$\dot{E}_{\rm part}(t) = \psi\rho_0 \left(\frac{t}{t_0}\right)^{-3}, \tag{3.29}$$

where ρ_0 is the density at t_0, and ψ is a scaling factor such that $\psi\rho_0 = \dot{E}_{\rm part}(t_0)$, which will be unique to each particle type. The rate at which energy is thermalized, $\dot{E}_{\rm th}(t)$, is given by the number of live particles N multiplied by the rate at which they lose energy,

$$\dot{E}_{\rm th}(t) = N(t) \times \psi\rho_0 \left(\frac{t}{t_0}\right)^{-3}. \tag{3.30}$$

At any time t, the oldest live particle originates from an earlier time $t_{\rm i}$, defined by

$$E_{\rm part}(t) = E_0 - \int\limits_{t_{\rm i}}^{t} \psi\rho_0 \left(\frac{t'}{t_0}\right)^{-3} {\rm d}t' = 0, \tag{3.31}$$

which is satisfied by

$$t_{\rm i} = \left(\frac{\psi\rho_0 t_0^3 t^2}{2E_0 t^2 + \psi\rho_0 t_0^3}\right)^{1/2}. \tag{3.32}$$

The number of live particles at time t is then

$$N(t) = \frac{\dot{\epsilon}_0 t_0}{2E_0} \ln\left[1 + 2\left(\frac{t}{t_{\rm ineff}}\right)^2\right] \tag{3.33}$$

where $t_{\rm ineff}$ is the inefficiency timescale defined in the previous section.

It is now straightforward to calculate the ratio $f_{\rm p}$ of thermalized to emitted energy for a massive particle of type p,

$$f_{\rm p}(t) = \frac{\dot{E}_{\rm th}}{\dot{E}_{\rm rad}} = \frac{\ln\left[1 + 2\left(\frac{t}{t_{\rm ineff,p}}\right)^2\right]}{2\left(\frac{t}{t_{\rm ineff,p}}\right)^2}. \tag{3.34}$$

Eq. 3.34 can be used to estimate the thermalization efficiencies of massive particles, where the relevant timescales $t_{\rm ineff,p}$ are given by Eq.s 3.22 (β-particles), 3.26 (α-particles), and 3.27 (fission fragments).

For γ-rays, the thermalization efficiency is approximately equal to the interaction probability: $f_\gamma(t) \approx 1 - e^{-\tau}$. We can estimate the optical depth $\tau \approx \rho\kappa_\gamma R_{\rm ej}$ using $\bar{\kappa}_\gamma$, the γ-ray opacity averaged over the emission spectrum. Optical depth is related to $t_{\rm ineff,\gamma}$ by

$$\left(\frac{t_{\rm ineff,\gamma}}{t_0}\right)^2 = \rho_0\bar{\kappa}_\gamma R_0 = \tau_0$$

$$\rightarrow \tau(t) = \tau_0\left(\frac{t}{t_0}\right)^{-2} = \left(\frac{t_{\rm ineff,\gamma}}{t}\right)^2,$$

so

$$f_\gamma(t) = 1 - \exp\left[-\left(\frac{t}{t_{\rm ineff,\gamma}}\right)^{-2}\right] \tag{3.35}$$

Figure 3.9 shows our analytic thermalization functions for $M_{\rm ej} = 5\times10^{-3}M_\odot$, and $v_{\rm ej} = 0.2c$, using the expressions for $t_{\rm ineff}$ derived in §3.3. For massive particles, we used $E_{\beta,0} = 0.5$ MeV, $E_{\alpha,0} = 6$ MeV, and $E_{\rm ff,0} = 125$ MeV. For γ-rays, we take $\bar{\kappa} = 0.1$ cm^2 g^{-1}, which gives $t_{\rm ineff,\gamma} \approx 1.4$ days.

As we will see in §3.5, the approximate analytic expressions Eq.s 3.34 and 3.35 agree fairly well with our numerical results.

3.5 Numerical Results

In this section, we present numerical calculations of thermalization efficiencies as determined by modeling the 3-dimensional transport of γ-rays, fission fragments, and α- and β-particles in a magnetized expanding medium. Our calculations used the time-evolving emission spectra introduced in §3.2.5, accounted for the time-dependent partition of radioactive energy among different decay products, and incorporated the detailed, energy-dependent energy loss rates derived in §3.3. The flux tube approximation was used to model charged particle transport, allowing us to explore the sensitivity of our results to the architecture of the ejecta's magnetic field. Additional details of our transport method are given in the Appendix A.

3.5.1 Thermalization efficiencies

Figure 3.10 presents the numerically calculated thermalization efficiency, $f(t)$, of all particles for the fiducial ejecta model ($M_{\rm ej}$= $5\times10^{-3}M_\odot$ and $v_{\rm ej}$= $0.2c$.) Fission fragments thermalize most efficiently, having $f(t) \gtrsim 0.5$ out to $t \sim 15$ days. Alpha- and β-particle

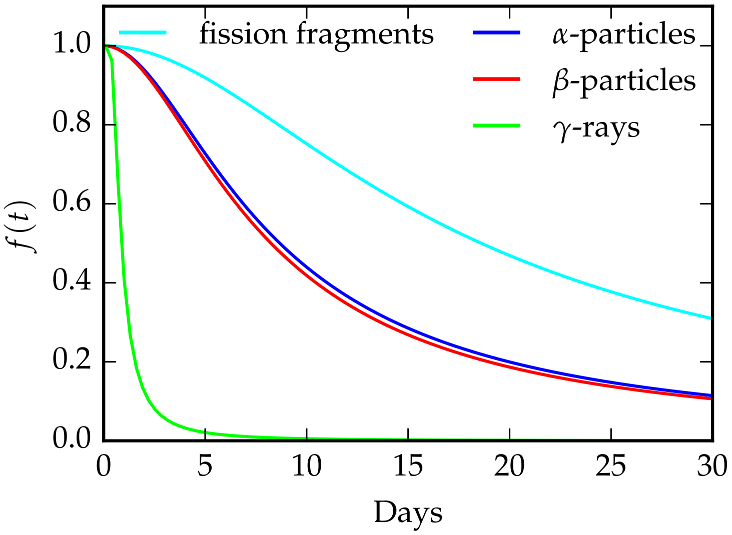

Figure 3.9: Analytic thermalization efficiencies, calculated with Eq.s 3.34 and 3.35. We use $t_0 = 1$ day, and $\rho_0 = 7.9 \times 10^{-15}$ cm^{-3}, corresponding to a uniform density ejecta with the same mass and energy as our fiducial model. For α's, β's, and fission fragments we take $E_0 = 6, 1,$ and 125 MeV, respectively.

thermalization is slightly lower, reaching $f(t) = 0.5$ around a week post-merger, while $f(t)$ for γ-rays is much lower, falling below 0.5 by $t \sim 1$ day.

For massive particles, we show $f(t)$ for radial (dotted lines), toroidal (solid lines), and lightly tangled ($\lambda = 0.25$; dashed lines) magnetic field geometries. The magnetic field configuration affects thermalization in three ways:

1. **Diffusion:** Radial or lightly tangled fields allow particles to diffuse outward into regions of lower density, and lead to lower $f(t)$.

2. **Escape:** Radial fields that allow charged particles to escape before they have completely thermalized will lower $f(t)$. This is most important for β-particles, which move faster than the ejecta.

3. **Frame-to-frame effects:** Particles in a homologous flow lose energy, as measured in the co-moving frame (cmf), as they move through the ejecta. These frame-to-frame losses reduce the amount of kinetic energy a particle has to thermalize, and therefore reduce $f(t)$. Radial fields and lightly tangled fields, which allow particles to move fairly freely through the ejecta, facilitate frame-to-frame effects. These losses are most important for α-particles and fission fragments, which have velocities of order v_{ej}, and thus have substantially different cmf energies in different regions of the ejecta.

In light of the above, it is not surprising that toroidal fields maximize $f(t)$; toroidal fields hold particles at one position in velocity space, preventing diffusion, escape, and frame-to-

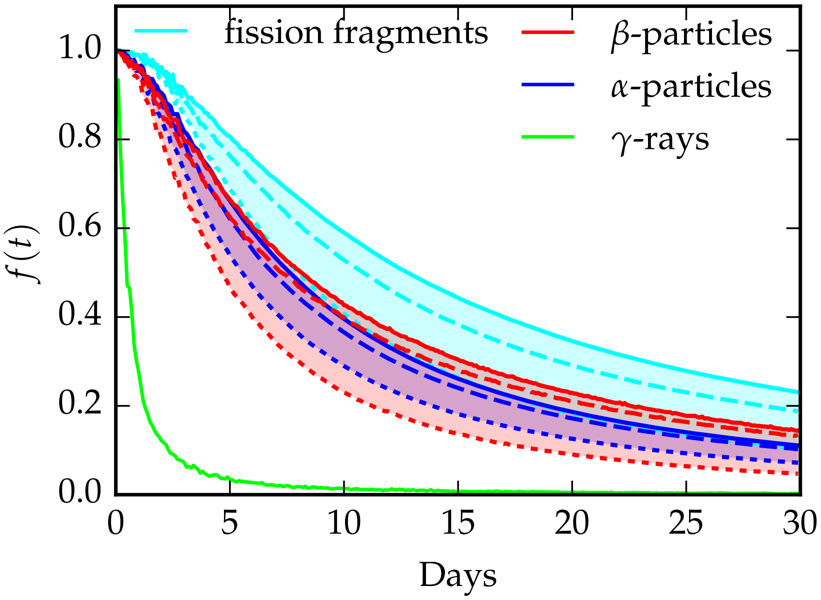

Figure 3.10: Thermalization efficiencies $f(t)$ for all particles in an ejecta with $M_{\rm ej} = 5 \times 10^{-3} M_\odot$, and $v_{\rm ej} = 0.2c$ (our fiducial model). Fission fragments thermalize most efficiently, followed by α-particles, β-particles, and γ-rays. For charged particles we plot $f(t)$ for radial (dotted lines), toroidal (solid lines), and moderately tangled ($\lambda = 0.25$; dashed lines) magnetic fields. Toroidal fields thermalize most efficiently, followed by random, then radial fields.

frame losses. Radial fields, in contrast, enhance all three of these effects and hence minimize $f(t)$. Thermalization in random fields falls between these two extremes. This behavior holds for all ejecta models studied.

While the trends shown in Figure 3.10—i.e., that $f_{\rm ff}(t) > f_\alpha(t) \approx f_\beta(t) > f_\gamma(t)$—are consistent across ejecta models, the values of $f(t)$ can vary significantly with $M_{\rm ej}$ and $v_{\rm ej}$. Figure 3.11 illustrates the variance and clarifies the dependence of $f(t)$ on the ejecta parameters. For each point ($M_{\rm ej}$, $v_{\rm ej}$) in parameter space, and for each particle type, we plot t_{50}—the time at which $f(t)$ drops to 50%. Cases in which $f(t = 30\,\text{days}) > 50\%$ are omitted from Figure 3.11.) To show how sensitive thermalization is to magnetic fields, we include results for radial (top panel) and toroidal (bottom panel) field geometries.

The thermalization of all particles increases with $M_{\rm ej}$ and decreases with $v_{\rm ej}$. The changes in efficiency are especially dramatic for massive particles. For the heaviest ejecta mass considered ($M_{\rm ej} = 5 \times 10^{-2} M_\odot$), massive particles thermalize efficiently out to late times regardless of $v_{\rm ej}$. The thermalization of γ-ray energy is low for all models tested.

Though the results shown are for the two-component composition described above, we find that the higher energy loss rates in the outer ejecta have only a small impact on thermalization. For radial fields, where the effect is most pronounced, the two-zone model results in an increase in total thermalization of $< 5\%$ relative to a one-zone model that assumes the entire ejecta has the "inner" ejecta composition. The $f(t)$ we calculate should be fairly insensitive to the exact division between inner and outer ejecta.

Effect of aspherical ejecta

The ejecta from a CO merger is likely to be aspherical, particularly in the case of NSBH merger, where most of the ejected mass is confined to the equatorial plane (e.g., Hotokezaka et al. 2013a). To estimate the effect on thermalization, we compare a spherical model to an oblate one, where both models have $M_{\rm ej}= 5 \times 10^{-3} M_\odot$ and $v_{\rm ej}= 0.2c$, radial magnetic fields, and a broken power law density profile with $(\delta, n) = (1, 10)$. For the oblate geometry, the density is a function of $\tilde{v}$, where

$$\tilde{v} = v\sqrt{a^{-2/3}\sin^2\theta + a^{4/3}\cos^2\theta}$$

is chosen so that isodensity contours are oblate spheroids of aspect ratio a.

Figure 3.12 compares the $f(t)$ for the oblate and spherical cases, and shows that massive particle thermalization increases with increasing asphericity. For an aspect ratio $a = 4$, the $f(t)$ for α's, β's, and fission fragments increase by a factor of ~ 1.5 relative to spherical ejecta. Gamma-ray thermalization is higher for the oblate geometry, but only slightly. The higher $f(t)$ are due to the higher density of the oblate ejecta, which more than compensates for the increased ease of escape in directions perpendicular to the equatorial plane. Figure 3.12 shows $f(t)$ only for radial magnetic fields, but we found similar increases for random and toroidal fields.

3.5.2 Total heating efficiency

To study the net heating efficiency, we convolve $f(t)$ for each decay product with the fraction that particle contributes to the total energy generation. The bottom panel of Figure 3.13 shows how the r-process decay

energy is divided among different particles, while the top panel shows the energy *thermalized* by each particle type, as a fraction of the total energy emitted across all decay channels. The $f(t)$ represented in Figure 3.13 are for a fiducial ejecta model with moderately tangled ($\lambda = 0.25$) magnetic fields. The total thermalization efficiency, which is simply a sum over particle types, is plotted in black. While γ's, α's, β's, and fission fragments all have $f(t) \approx 1$ at very early times, the initial *total* thermalization efficiency is less than one because a significant fraction of the β-decay energy is lost to neutrinos.

The net thermalization efficiency, in this model, drops below 0.5 by $t = 1$ day, and below 0.1 by $t \sim 10$ days. While β-particles and γ-rays dominate the energy production at all times, γ-rays thermalize inefficiently, and supply very little heating after $t \sim 1$ day. While α-decay produces less than $\sim 10\%$ percent of the total energy, the α-particles thermalize fairly efficiently, and so contribute a significant fraction of the total thermalized energy.

The total heating efficiency has the expected dependence on the ejecta parameters: greater masses and lower velocities lead to higher $f_{\rm tot}(t)$, as shown in Figure 3.14. Ther-

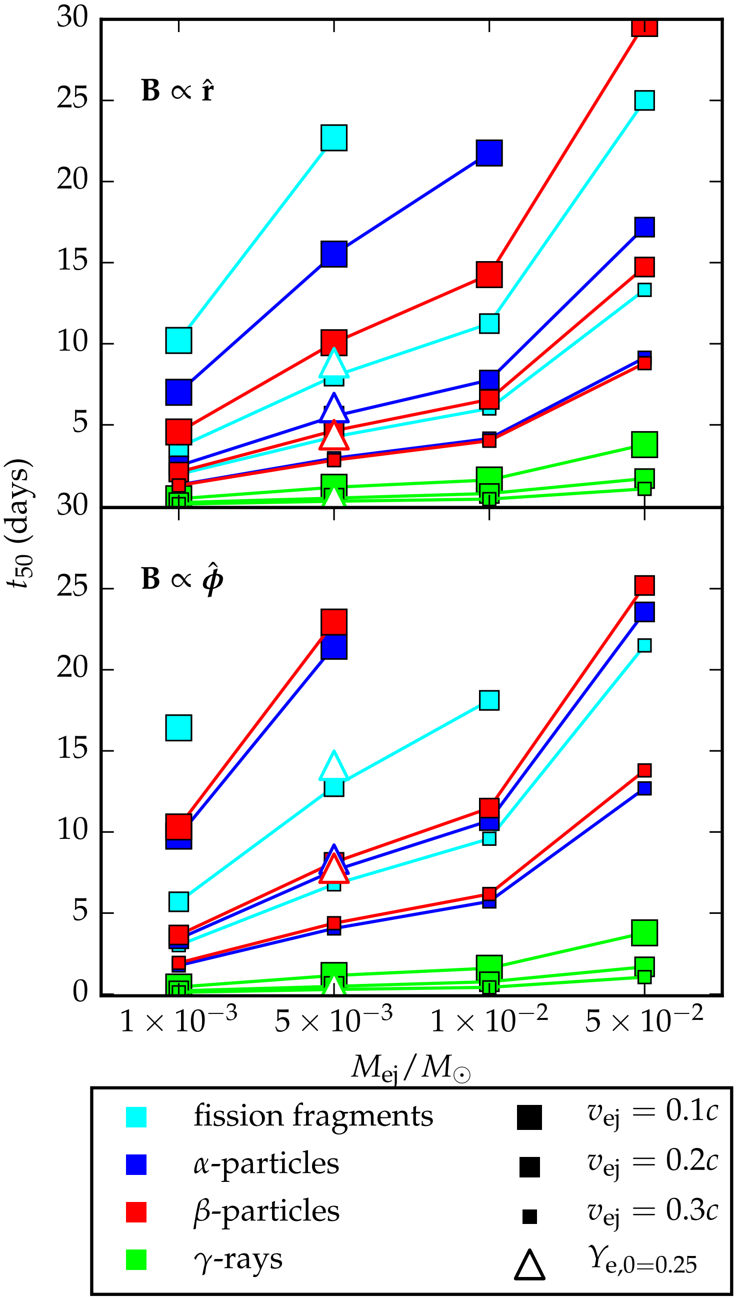

Figure 3.11: The time at which $f(t)$ drops below 50% (t_{50}) for all particles, for all $M_{\rm ej}$ and $v_{\rm ej}$ considered. Results for a radial (toroidal) magnetic field are shown in the top (bottom) panel. Thermalization increases with mass and decreases with velocity. Fission fragments thermalize most efficiently, followed by α-particles and β-particles, and finally γ-rays. Toroidal fields result in more robust thermalization of all massive particles.

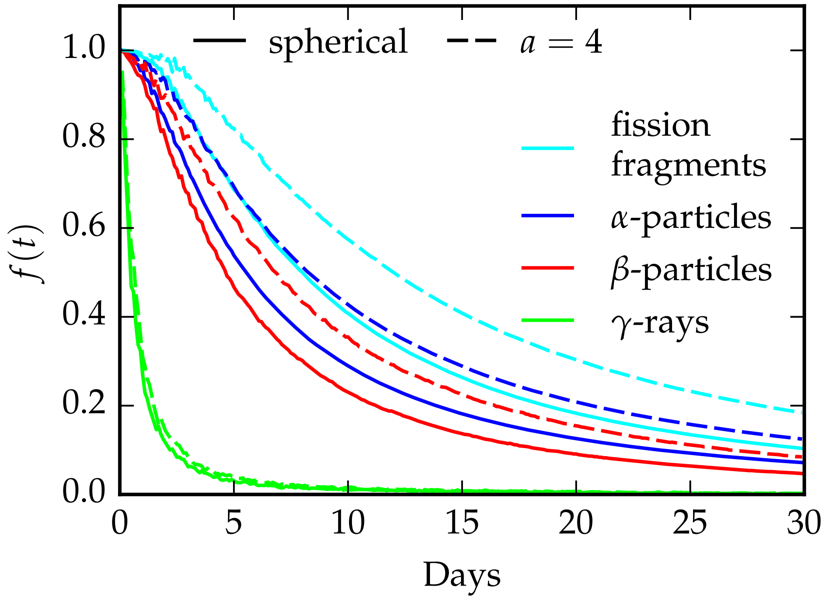

Figure 3.12: Thermalization efficiencies for oblate ejecta with aspect ratio $a = 4$, compared to the standard spherical geometry, for the fiducial mass and velocity and radial magnetic fields. Thermalization increases with increasing asymmetry. We found similar increases for random and toroidal fields.

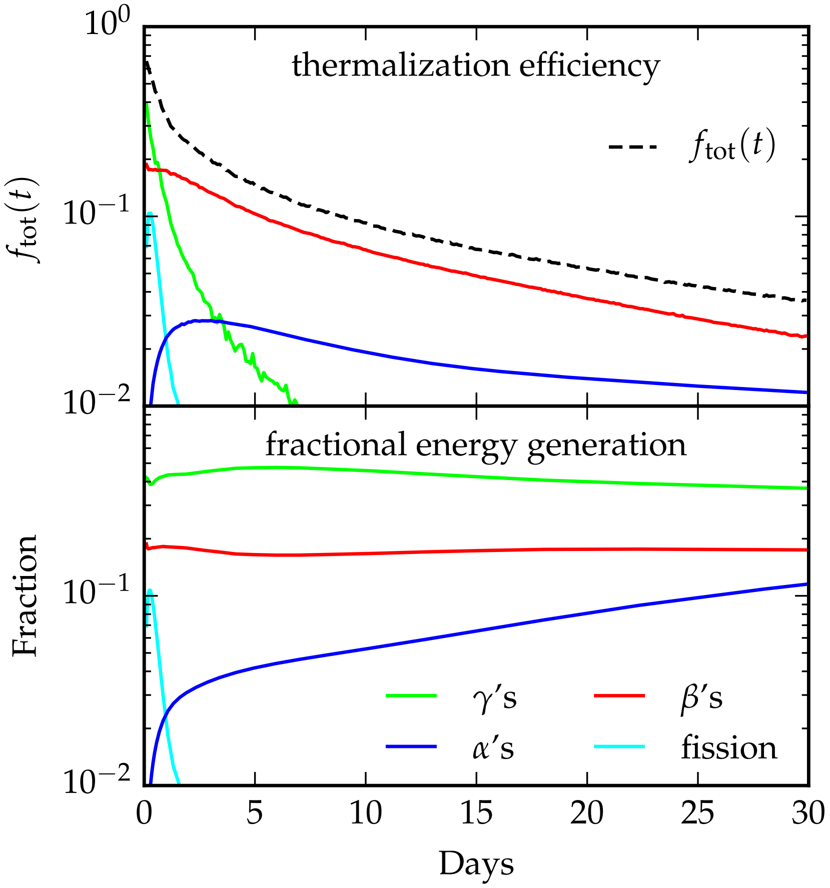

Figure 3.13: *Bottom panel:* The fractional energy generation associated with each type of particle, from r-process simulations using the FRDM mass model. The division of β-decay energy among β-particles, γ-rays, and neutrinos was calculated for our representative SPH trajectory with $Y_{\rm e,0} = 0.04$. *Top panel:* The fractions from the bottom panel, convolved with $f(t)$ for each particle, for the fiducial model with random magnetic fields. The total thermalization efficiency, $f_{\rm tot}$, plotted as a dashed black line, is the sum of the particle-specific curves. Beta- and α-particles supply most of the thermalized energy.

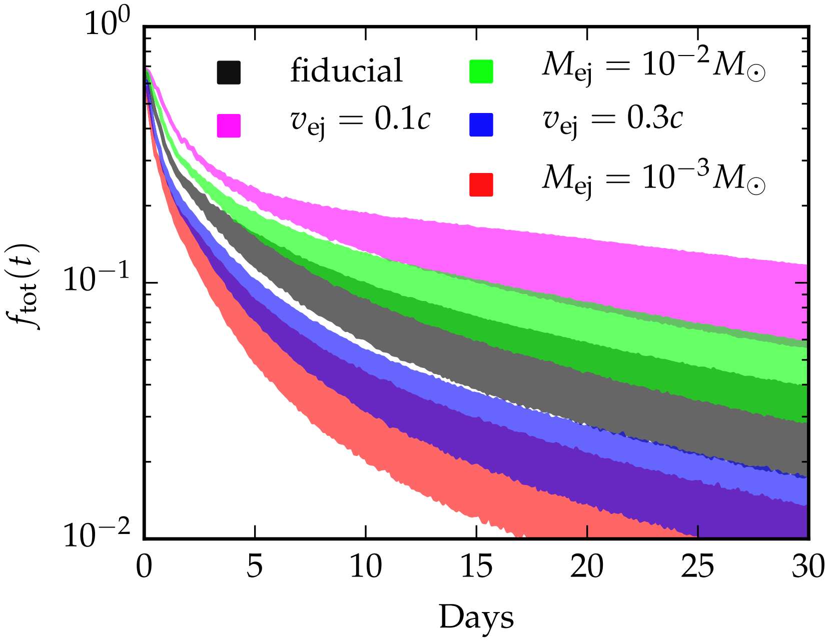

Figure 3.14: Total thermalization efficiencies for different ejecta models ($M_{\rm ej}$, $v_{\rm ej}$) using FRDM energy generation rates. The fiducial model is plotted in black. Other curves differ from the fiducial model in $M_{\rm ej}$ or $v_{\rm ej}$ only. The width of the curves reflects the variation in $f(t)$ for different magnetic field configurations; the curves are bounded on top by $f_{\rm tot}(t)$ for a toroidal field and on bottom by $f_{\rm tot}(t)$ for a radial field configuration.

malization for the low-mass and high-velocity models falls below 0.5 within a few days, and below 0.2 by $5 - 7$ days. The high-mass and low-velocity models thermalize much more efficiently, sustaining $f_{\rm tot}(t) > 0.5$ out to $t \lesssim 1$ week, and not falling below $f_{\rm tot}(t) = 0.2$ until $t \sim 15 - 20$ days. There is also variation within each model (up to a factor of ~ 2) due to uncertainties in the magnetic field.

Dependence on nuclear physics

The radioactive energy generation—and therefore the thermalization—depends on r-process yields, which in turn are sensitive to variations in nuclear physics models and astrophysical conditions. To explore this effect, we consider r-process yields computed for different mass models, and for different initial $Y_{\rm e}$ of the ejected matter.

The yields differ primarily in the amount of translead nuclei synthesized relative to lighter r-process elements. Mendoza-Temis et al. (2015) have shown that the production of translead nuclei is sensitive to nuclear physics inputs, in particular to neutron separation energies near $N = 130$. As discussed in §3.2.3, the production of translead nuclei also depends on initial electron fraction, decreasing as $Y_{\rm e,0}$ increases.

R-process yields could impact thermalization in two ways. First, different yields have different abundance-averaged compositional properties, and could give rise to different thermalization rates. Second, because nuclei heavier than lead decay mainly by fission and α-emission, while lighter nuclei undergo β-decay, the amount of translead material will alter the relative importance of α- and β-decay. Since all α-decay energy is transferred to energetic α-particles, which thermalize efficiently, while $\gtrsim 70\%$ of β-decay energy goes to γ-rays and neutrinos, which do not, enhanced α-decay may increase thermalization. Based on these arguments, we expect that differences in the amounts of translead nuclei will result in different $f_{\rm tot}(t)$, and therefore, differences in predicted kilonova light curves.

To explore the strength of these effects, we compare the thermalization efficiency for three different compositions: the reference r-process yields (based on the FRDM mass model); yields for the DZ31 mass model, which predicts increased production of translead nuclei (see Figure 3.1); and yields from a calculation using the FRDM model with $Y_{e,0} = 0.25$.

We found that the DZ31 model predicts a composition whose abundance-averaged properties and emission spectra are very similar to those predicted by the FRDM model. We therefore expect that the different yields found for the DZ31 model will not significantly change $f(t)$ for individual particles. In contrast, the high-$Y_{\rm e,0}$ composition has average compositional properties and emission spectra that depart from the reference case (FRDM, $Y_{\rm e,0} = 0.04$), so we calculate for this composition $f(t)$ of all individual decay products for our fiducial ejecta ($M_{\rm ej} = 5 \times 10^{-3} M_{\odot}$, $v_{\rm ej} = 0.2c$). The thermalization timescales, plotted in Figure 3.11 as open triangles, are similar to those for the standard low-$Y_{\rm e,0}$ composition. For both the DZ31 and high-$Y_{\rm e,0}$ cases then, impacts on $f_{\rm tot}(t)$ result from differences in the relative importance of each heating channel, not differences in how efficiently individual decay products thermalize.

Figure 3.15 compares $f_{\rm tot}(t)$ for the three cases studied. In the top panel, we show $f_{\rm tot}(t)$ and the contributions from each decay product, determined using energy generation rates from the DZ31 nuclear mass model abundances, for which α-decay dominates the energy production at late times. The middle panel shows an analogous calculation for the FRDM model with $Y_{\rm e,0} = 0.25$, which has negligible late-time α-decay. In the bottom panel, we compare $f_{\rm tot}(t)$ for these models with the fiducial FRDM model. The greater role of α-decay in the DZ31 model increases $f_{\rm tot}(t)$ by a factor of $\gtrsim 1.5$, mainly due to the fact that less energy is lost in neutrinos and γ-rays, which thermalize very inefficiently. In the fiducial composition α-decay and fission produce only a small fraction of the energy, so the effect of increasing $Y_{\rm e,0}$ is modest. A stronger effect might be seen for DZ31, which produces more translead nuclei when $Y_{\rm e,0}$ is low, and is therefore more likely to experience dramatic decreases in translead production when the initial electron fraction rises.

3.6 Effect on Kilonova Light curves

To determine the effect of thermalization on kilonova observables, we incorporated our results for $f_{\rm tot}(t)$ into the time-dependent Monte Carlo radiation transport code SEDONA

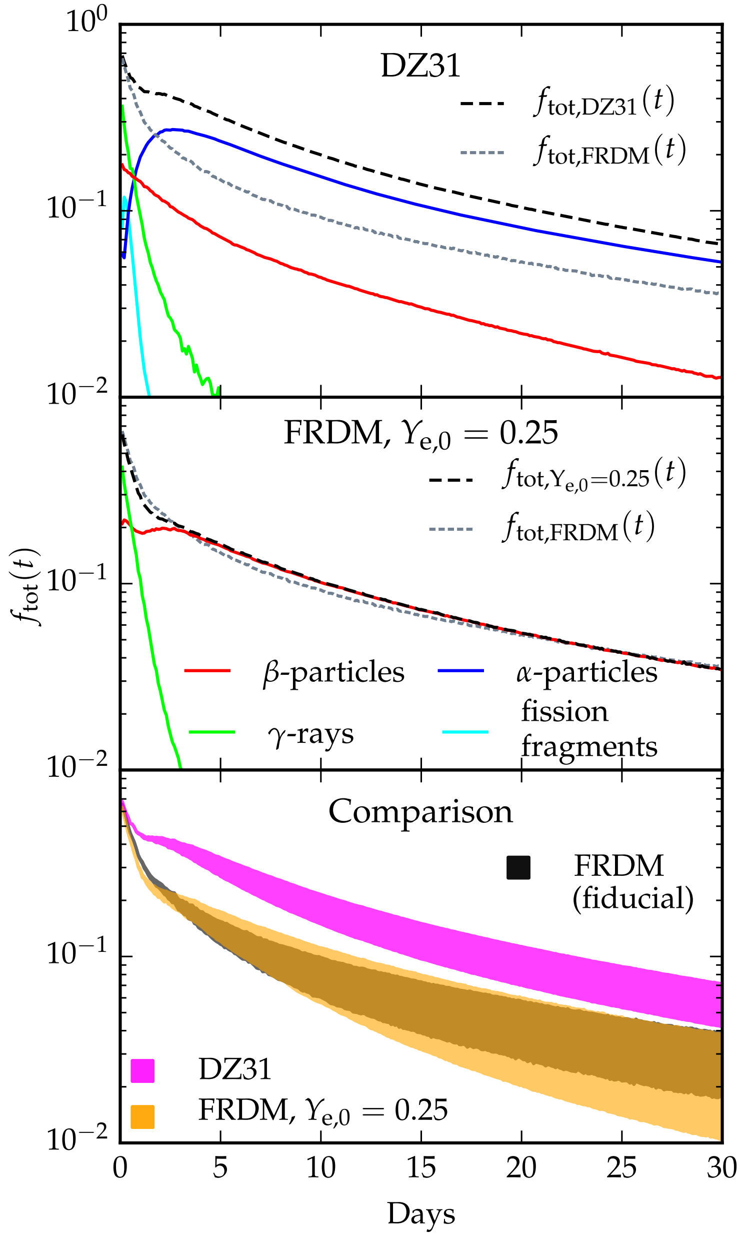

Figure 3.15: The effect of nuclear physics inputs on total thermalization efficiency. *Panels 1 and 2:* $f(t)$ (fiducial $M_{\rm ej}$, $v_{\rm ej}$; random fields) convolved with fractional energy generation rates for the DZ31 nuclear mass model (top panel) and a high-$Y_{\rm e,0}$ FRDM trajectory (middle panel). Solid lines show the fraction of emitted energy thermalized by each particle as a function of time, and $f_{\rm tot}(t)$ is plotted in black dashed lines. *Panel 3:* The range of $f_{\rm tot}(t)$ expected for each of the cases shown in Panels 1 and 2. We plot $f_{\rm tot}(t)$ for the low-$Y_{\rm e,0}$ FRDM composition in black for comparison. The widths of the curves are due to the range of possible magnetic field configurations.

Table 3.1: Analytic fit parameters for $f_{\mathrm{tot}}(t)$

Model		Coefficients								
$M/M_\odot$	v_{ej}/c	Random			Radial			Toroidal		
		a	b	d	a	b	d	a	b	d
1×10^{-3}	0.1	2.01	0.28	1.12	2.17	0.26	1.51	2.04	0.26	1.07
1×10^{-3}	0.2	4.52	0.62	1.39	4.75	0.76	1.68	4.63	0.55	1.39
1×10^{-3}	0.3	8.16	1.19	1.52	8.57	1.58	1.77	8.36	1.08	1.53
5×10^{-3}	0.1	0.81	0.19	0.86	0.91	0.12	1.28	0.81	0.19	0.79
5×10^{-3}	0.2	1.90	0.28	1.21	2.04	0.26	1.53	1.94	0.26	1.20
5×10^{-3}	0.3	3.20	0.45	1.39	3.36	0.48	1.63	3.26	0.41	1.39
1×10^{-2}	0.1	0.56	0.17	0.74	0.62	0.10	1.16	0.55	0.18	0.65
1×10^{-2}	0.2	1.31	0.21	1.13	1.43	0.17	1.46	1.34	0.19	1.11
1×10^{-2}	0.3	2.19	0.31	1.32	2.32	0.30	1.57	2.24	0.28	1.32
5×10^{-2}	0.1	0.27	0.10	0.60	0.26	0.07	0.85	0.27	0.10	0.54
5×10^{-2}	0.2	0.55	0.13	0.90	0.61	0.08	1.24	0.56	0.13	0.85
5×10^{-2}	0.3	0.95	0.15	1.13	1.01	0.12	1.39	0.96	0.14	1.11

(Kasen et al. 2006), and carried out light curve calculations. The calculations here resemble those of Barnes & Kasen (2013), but include thermalization effects.

3.6.1 Analytic fit to thermalization efficiency

For easy inclusion of thermalization in light curve simulations, we propose a simple analytic formula for $f_{\mathrm{tot}}(t)$ which provides a good fit to our detailed numerical calculations,

$$f_{\mathrm{tot}}(t) = 0.36 \left[\exp\left(-at\right) + \frac{\ln\left(1 + 2bt^{d}\right)}{2bt^{d}} \right], \tag{3.36}$$

where a, b, and d are fitting constants. The parameterized form of Eq. 3.36 is motivated by our approximate analytic solutions for $f(t)$ (Eq.s 3.34 and 3.35), with slight modifications to improve the quality of the fit and account for energy lost to neutrinos. Table 3.1 gives the best-fit parameters for all the ejecta models considered, for energy generation rates of the FRDM nuclear mass model. A comparison of Eq. 3.36 to numerical results is presented in Figure 3.6.1. For simplicity, Figure 3.6.1 shows results only for random magnetic fields. However, our model provides an equally good fit for radial and toroidal fields.

We found that, in the case of the FRDM mass model, compositions from high-$Y_{\mathrm{e},0}$ ejecta have thermalization profiles similar to compositions from initially neutron-rich ejecta. This suggests that our thermalization models may be appropriate for material ejected dynamically and from disk winds, regardless of the initial electron fraction. However, we note that the insensitivity of $f_{\mathrm{tot}}(t)$ to $Y_{\mathrm{e},0}$ may not be as robust for other nuclear mass models. The effect of $Y_{\mathrm{e},0}$ may be particularly pronounced for the DZ31 model, which produces large amounts of translead nuclei, and therefore predicts significant α-decay. Changes in $Y_{\mathrm{e},0}$ could inhibit

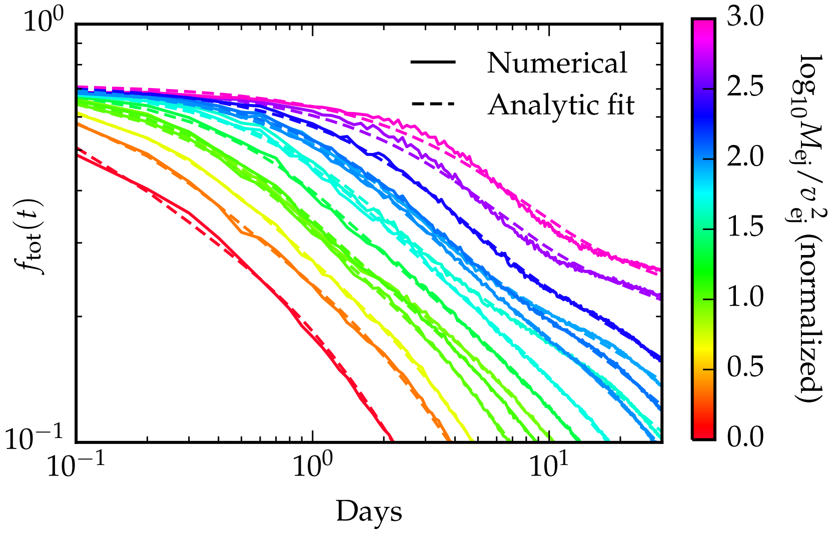

Figure 3.16: Numerical results for $f_{\rm tot}(t)$ (solid lines) compared to the analytic fit (dashed lines) given by Eq. 3.36 for random magnetic fields and all $(M_{\rm ej}, v_{\rm ej})$ considered. The lines are color-coded by the base-10 logarithm of the ratio $M_{\rm ej}/{v_{\rm ej}}^2$, which we have normalized to the minimum value found in our suite of models. Equation 3.36 fits results from radial and toroidal fields with similar success.

the production of these nuclei, decrease the role of α-decay, and thus alter thermalization efficiency. The effect on $f_{\rm tot}(t)$ would be much stronger than for the FRDM model, which does not produce many translead nuclei even for favorable $Y_{\rm e,0}$.

3.6.2 Light curves

The net thermalization efficiency, $f_{\rm tot}(t)$, has a significant impact on kilonova luminosity. Figure 3.17 compares bolometric light curves calculated using our derived $f_{\rm tot}(t)$ to those assuming 100% thermalization. We also show results for a treatment which propagates γ-rays, but assumes charged particle energy thermalizes instantly. This was the method used to estimate $f_{\rm tot}(t)$ in earlier SEDONA kilonova simulations, including Barnes & Kasen (2013).[1] (A similar simplification was invoked in the discussion of net heating by Hotokezaka et al. (2016).) For all radiation transport simulations, we have used the simplified composition and the boosted, synthetic r-process opacities of Kasen et al. (2013). We consider here only models with low $Y_{\rm e,0}$, which robustly produce r-process elements including Lanthanides and

---

[1] SEDONA's original treatment of thermalization assumed that β-decay generated 90% of the r-process decay energy, with fission accounting for the other 10%. Of the β-decay energy, 25% was taken to be lost to neutrinos, and the remaining 75% was split evenly between β-particles and γ-rays. The energy from β-particles and fission fragments was thermalized promptly, while the energy from γ-rays was converted into 1 MeV photons, which were propagated through the ejecta in a Monte Carlo transport scheme.

Actinides, making our choice of opacity appropriate. Models with higher initial electron fractions may fail to produce these heavy elements. The opacities for such models would be much lower, and the associated light curves would be shorter, brighter, and bluer (e.g. Metzger et al. 2010; Barnes & Kasen 2013; Kasen et al. 2015).

Figure 3.17 shows that our more accurate treatment of thermalization impacts predicted photometry for all ejecta models considered. Relative to earlier calculations with less sophisticated thermalization schemes, we find kilonova light curves peak slightly earlier, have lower luminosities at peak, and have much dimmer late-time luminosities. The effects of thermalization are most pronounced for less massive and higher velocity ejecta models, which are dimmer and fade more quickly than their slower, more massive counterparts.

The uncertainties complicating the calculation of $f_{\rm tot}(t)$, outlined in earlier sections, lead to uncertainties in light curve calculations. The most important of these are illustrated in the middle panel of Figure 3.17, which presents bolometric light curves for our fiducial ejecta model for all magnetic fields considered and for the DZ31 nuclear mass model. The effect of field configuration is straightforward; random or toroidal fields trap particles, enhance $f_{\rm tot}(t)$, and produce more luminous kilonovae relative to radial fields. Nuclear mass model plays a role by determining the yields of translead nuclei, and therefore the amount of energy produced by α-decay. Models, like DZ31, that derive a sizable fraction of their radioactive energy from α-decay, have a higher $f_{\rm tot}(t)$, and therefore greater bolometric luminosity. The luminosity increase for the DZ31 composition is a result both of higher $f_{\rm tot}(t)$ due to more α-decay, and to the greater absolute amount of energy produced by r-process decay for the DZ31 model relative to the FRDM model (see §3.2.4.) Ejecta geometry, which we have not explored in Figure 3.17, can also affect observed light curves, by altering $f_{\rm tot}(t)$ (see 3.5.1) and by introducing viewing angle dependence. Three dimensional kilonova simulations are needed to fully explore and document these uncertainties.

Though thermalization can impact kilonovae's bolometric luminosities substantially, it has little effect on their characteristic red colors, which are derived from a composition rich in Lanthanides. Figure 3.18 shows the broadband evolution of our fiducial ejecta for two treatments of thermalization, one which includes time-dependent $f_{\rm tot}(t)$, and one which relies on the simple γ-ray transport scheme of Barnes & Kasen (2013). Including $f_{\rm tot}(t)$ leads to dimmer light curves in all bands (a result of the kilonova's lower energy budget) but does not change the relative strengths of the broadband curves. The effect of thermalization on a kilonova's spectral energy distribution is therefore minor.

3.6.3 Implications for the kilonova accompanying GRB 130603B

An excess near infrared (NIR) flux discovered in the afterglow of the short gamma ray burst GRB 130603B has been widely interpreted as a kilonova (Tanvir et al. 2013; Berger et al. 2013). Tanvir et al. (2013) determined that the source of the flux had an absolute AB magnitude in the J-band of -15.35 at $t \sim 7$ days. Having incorporated $f_{\rm tot}(t)$ into kilonova light curve models, we can more confidently constrain the mass ejected in the kilonova associated with GRB 130603B.

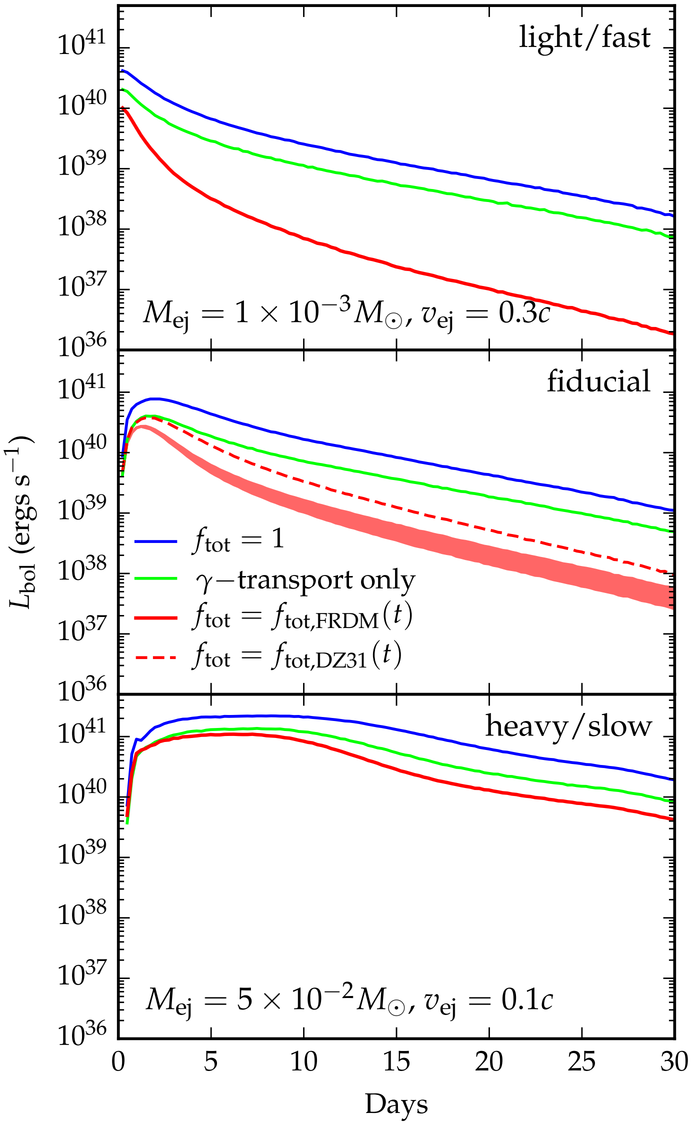

Figure 3.17: Synthetic bolometric light curves calculated with SEDONA for three different treatments of thermalization: full thermalization (blue curves); SEDONA's original thermalization scheme, which deposits charged particle energy but explicitly tracks the deposition of γ-ray energy (lime curves); and the time-dependent $f_{tot}(t)$ from our numerical simulations (red curves). Light curves in the top and bottom panels adopt $f_{tot}(t)$ given by random fields and the FRDM mass model. To illustrate the effect of uncertainties in $f_{tot}(t)$ on light curves, we plot for our fiducial model (middle panel), L_{bol} for a range of magnetic fields (thick red curve) and for the DZ31 mass model (red dashed curve). Accounting for time-dependent thermalization efficiencies has a significant impact on kilonova luminosity, particularly for models with lower masses and higher velocities. For our fiducial model, the predicted luminosity is lower by a factor of $\lesssim 2$ at peak, and by 10 days is lower by an factor of 5.

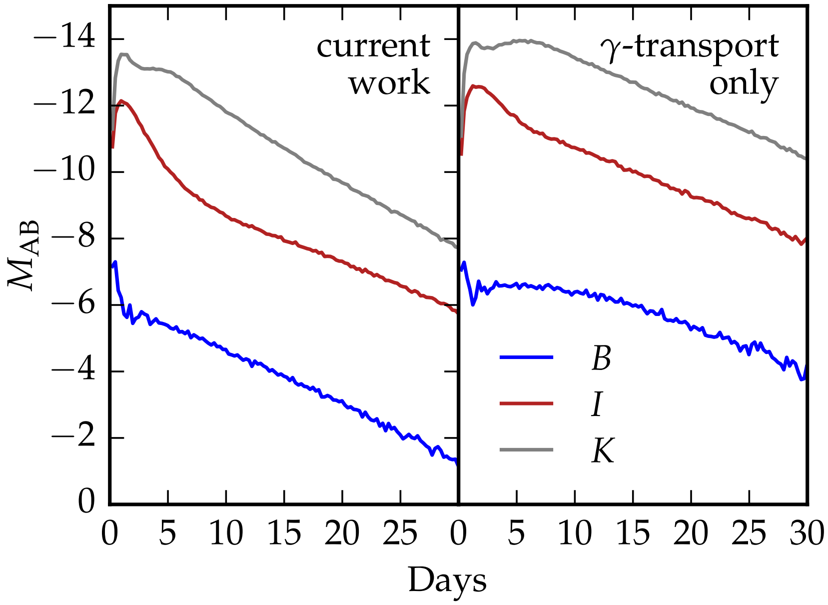

Figure 3.18: Select broadband light curves for our fiducial ejecta model for two treatments of thermalization: full $f_{\rm tot}(t)$ (left panel), and the cruder treatment employed in earlier kilonova calculations (right panel). The curves are dimmer in the newer models, reflecting the reduction in thermalized energy, but relationships between the light curves in the various bands is mostly unchanged, so the kilonova colors are preserved.

In Figure 3.19, we compare the detected flux to J-band light curves for various ejecta models, and find the observed flux is consistent with $5 \times 10^{-2} M_\odot \lesssim M_{\rm ej} \lesssim 10^{-1} M_\odot$. This mass is higher than what is typically predicted for the dynamical ejecta from a binary neutron star merger, suggesting that if the kilonova interpretation is correct, the progenitor of GRB 130603B was perhaps a neutron star-black hole merger, or that the mass ejected was significantly enhanced by post-merger disk winds.

Our mass estimate here is an improvement over earlier work which neglected detailed thermalization, and gives substantially different results. For example, Piran et al. (2014) suggested $M_{\rm ej} \sim 0.02 M_\odot$, less than half our new value. However, we have not accounted for viewing angle effects. If the ejected material is mainly confined to the equatorial plane, the emission will be brighter when the system is viewed face-on (Roberts et al. 2011), which would reduce the inferred mass somewhat. In an oblate ejecta, thermalization will also be more efficient, which could have a small impact on mass measurements. Finally, we note that different nuclear mass models predict different rates of radioactive heating and differing $f_{\rm tot}(t)$, which introduce additional uncertainties into our mass estimate. Radiation transport simulations in three dimensions with time-dependent thermalization models will better constrain $M_{\rm ej}$.

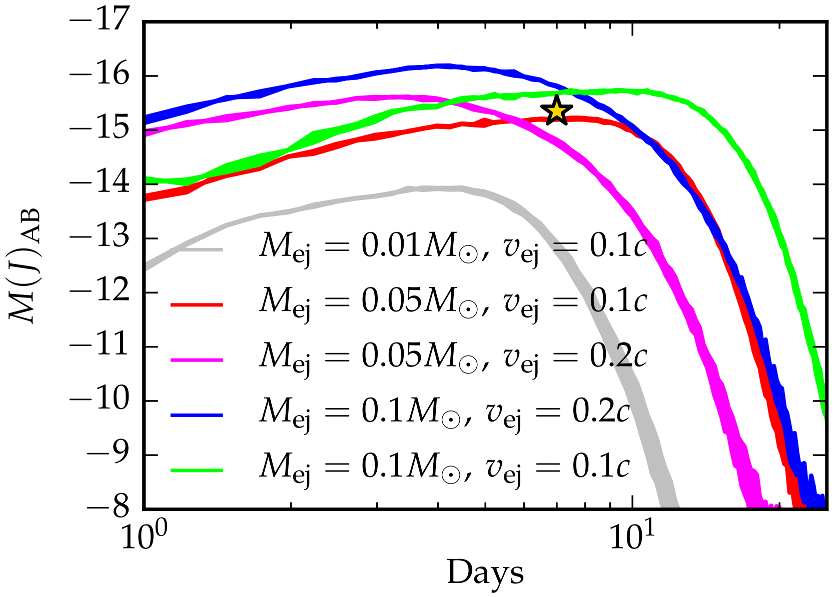

Figure 3.19: Absolute (AB) J-band light curves for several ejecta models. As in earlier figures, the width of the curves is produced by differences in $f_{\mathrm{tot}}(t)$ due to different magnetic field configurations. The excess IR flux (gold star) suggests an ejected mass between 5×10^{-2} and $10^{-1} M_\odot$.

3.6.4 Late-time light curve

Late time kilonova light curves may probe the history of r-process nucleosynthesis in CO mergers. At ~ 2 days after merger, fission ceases to be important, and α- and β-decay dominate the kilonova's energy supply. Energy from α-decay is transferred entirely to fast α-particles, which thermalize fairly efficiently out to late times. Beta particles thermalize with similar efficiency, but carry only a fraction ($\sim 25\%$) of the total β-decay energy, with the rest lost to neutrinos and γ-rays. A kilonova's late-time luminosity will therefore depend on the relative importance of α- versus β-decay. Because only nuclei with $200 \lesssim A \lesssim 250$ undergo α-decay, the late time kilonova luminosity may diagnose the presence of heavy elements in the ejecta, and therefore constrain the neutron-rich conditions required for heavy element formation.

We gauge the relative strength of late-time kilonova light curves for different $Y_{e,0}$ by estimating the percent of energy from the decay of r-process elements emitted as fission fragments, α-, and β-particles, time-averaged over $t = 10 - 100$ days. (Note that while all energy from α-decay emerges as α-particles, *β-particles* receive only 25-30% of the energy from *β-decay*.) The results for our representative SPH trajectory, for a range of $Y_{e,0}$ and two nuclear mass models, are shown in Figure 3.20. The curves suggest that systems with $Y_{e,0} \lesssim 0.17$ have more robust late-time heating, and are likely to exhibit late time light curves that are more luminous by a factor of up to ~ 2.

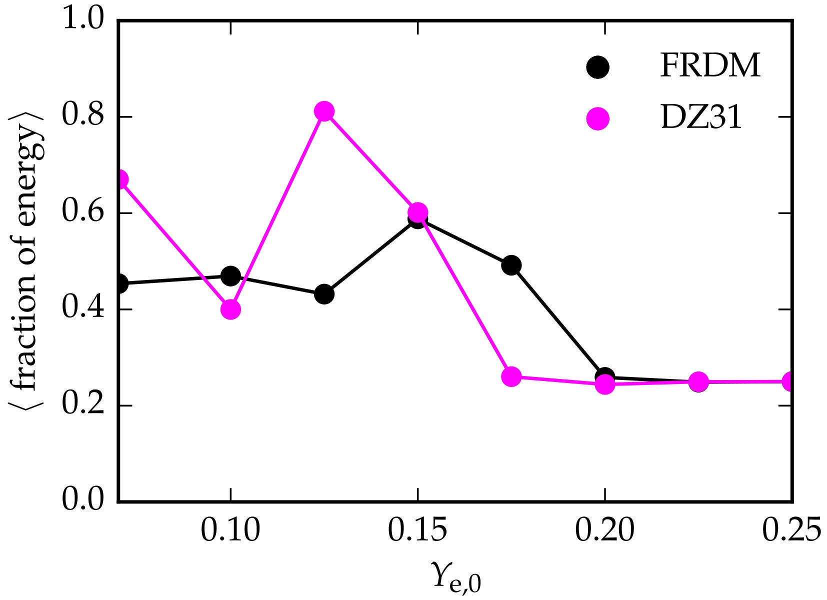

Figure 3.20: The time-averaged fraction of the r-process decay energy emitted as β- and α-particles and fission, as a function of initial Y_e. The data was taken from r-process calculations on our representative SPH trajectory, with $Y_{e,0}$ artificially altered. The lower the initial electron fraction is, the more energy from α-decays is available to drive a late time light curve.

If fission is more significant at late times than our calculation predicts (e.g., Hotokezaka et al. (2016) find that fission supplies $\gtrsim 10\%$ of the total energy out to late times) the dependence of the late-time light curve on $Y_{\rm e,0}$ could be much stronger. Fission fragments thermalize extremely efficiently well past maximum light. Since very neutron-rich conditions are needed to build up the heavy nuclei ($A \gtrsim 250$) that undergo fission, in a strongly fissioning ejecta, late-time luminosity could depend sensitively on $Y_{\rm e,0}$.

A key observable for probing the nuclear physics of CO mergers may be the ratio of the kilonova luminosity measured at peak brightness to that observed on the light curve tail. At peak, the luminosity is found to roughly equal the instantaneous energy deposition rate ("Arnett's Law", Arnett 1982). At $t \gg t_{\rm peak}$, when the ejecta becomes transparent, the emergent luminosity again tracks the energy deposition rate. Assuming the radioactive energy released by r-process material follows a power law, $\dot{\epsilon} \propto t^{-\eta}$, the ratio of peak luminosity to luminosity at some later time, $t_{\rm tail} > t_{\rm peak}$, is

$$\frac{L(t_{\rm peak})}{L(t_{\rm tail})} = \left(\frac{t_{\rm peak}}{t_{\rm tail}}\right)^{-\eta} \frac{f_{\rm tot}(t_{\rm peak})}{f_{\rm tot}(t_{\rm tail})}. \tag{3.37}$$

Assuming the decay index, η, is reasonably constrained, measuring this luminosity ratio provides some handle on the thermalization efficiency $f_{\rm tot}(t)$ and hence the presence of α-decaying or fissioning translead isotopes, which enhance $f_{\rm tot}(t)$ at late times. In general, this ratio will depend on $M_{\rm ej}$, $v_{\rm ej}$, and magnetic field configuration, as well as translead abundance. However, $M_{\rm ej}$ and $v_{\rm ej}$ can be constrained by other light curve properties, including rise time and peak brightness. In cases where these degeneracies can be untangled, the luminosity ratio may be a useful diagnostic of translead production.

As a simple test case, we consider light curves for our fiducial ejecta model calculated for the FRDM (low α-decay) and DZ31 (high α-decay) mass models. Setting $t_{\rm tail}/t_{\rm peak} = 5$, we find that $L_{\rm peak}/L_{\rm tail}$ is higher for the FRDM case by $\sim 10\%$, an effect due entirely to differences in translead production. While differences of this magnitude may be difficult to identify given other uncertainties, the effect of translead isotopes' decay will be stronger at later times, and for systems with high rates of late-time fission. If, as considered earlier, fission contributes 10% of the radioactive energy at late times, the peak-tail luminosity ratio will be enhanced by a factor of ~ 2 relative to our reference case, which has negligible late-time fission.

More detailed studies are needed to fully explore and clarify the relationship between light curves and composition, and we defer such an exploration to later work. Even if extracting constraints on the nuclear physics proves challenging, the luminosity ratio could provide information about $f_{\rm tot}(t)$, which would aid in understanding the ejecta's mass, energy, and magnetic fields.

3.7 Conclusion

We have shown that the radioactive energy from the decay of r-process material does not completely thermalize in the ejecta from CO mergers. For the first time, we have explicitly simulated the thermalization of all suprathermal r-process decay products in the heavy-element-rich kilonova ejecta. From these simulations, we derived time-dependent expressions for the net kilonova thermalization efficiency, $f_{\text{tot}}(t)$, for models spanning a range of expected ejecta masses and velocities. For most parameters studied, $f_{\text{tot}}(t)$ drops below 0.5 within five days after the merger. At 15 days after merger, $f_{\text{tot}}(t)$ may be as low as $0.01 - 0.1$. Thermalization therefore has a significant impact on the peak luminosity of kilonovae and the late time light curve decline rate.

We have also explored the dependence of $f_{\text{tot}}(t)$ on electron fraction and nuclear mass model, and outlined how variations in these parameters may systematically affect thermalization. In general, systems that favor the production of translead nuclei have higher thermalization efficiencies at late times. This is because a greater fraction of radioactive energy is emitted through α-decay and fission channels, which thermalize more efficiently than energy from β-decays, since less energy is lost to γ-rays and neutrinos.

We have presented updated radiation transport simulations that incorporate our new calculations of time-dependent thermalization, and find that thermalization has a significant effect on the predicted photometry of kilonovae. Compared to older models that neglected detailed thermalization, our new light curves peak earlier and at lower luminosities, and are much dimmer (by a factor of ~ 10) at late times ($\gtrsim 15$ days after peak). Our new models of kilonova with Lanthanide-rich r-process ejecta keep their characteristic red color, and are much more luminous in infrared (I-, J-, and K-) bands than in the optical.

Our results have consequences for detecting kilonovae, whether blindly, or as counterparts to gravitational wave events. While our new models retain the red color believed to be a defining kilonova signature, the rapid decline of $f_{\text{tot}}(t)$ poses a challenge to detection, and underscores the necessity of timely follow-up of GW triggers. Since $f_{\text{tot}}(t)$ is lower, and declines more quickly, in less massive systems, this is especially important for kilonovae generated by merging neutron stars, which are typically expected to be less massive than BHNS kilonovae by a factor of ~ 10.

The recent detection of the gravitational wave event GW150914 (Abbott et al. 2016c) spurred a slew of EM follow-up activities (Abbott et al. 2016b; Soares-Santos et al. 2016). While the GW signal turned out to be the result of a binary black hole merger, which is not expected to have an EM counterpart, the follow-up campaign offers a sense of the prospects of detecting a kilonova counterpart to future GW events. From a kilonova standpoint, some of the most promising observational efforts were carried out by the Dark Energy Camera (DECam), which had limiting (AB) magnitudes $i < 22.5$ and $z < 21.5$; the VLT Survey Telescope (VLS), which reached $r < 22.4$, and VISTA, with $J < 20.7$.

Had the GW trigger been due to a typical NSBH merger located 100 Mpc distant, the associated kilonova ($M_{\text{ej}} = 5 \times 10^{-2} M_{\odot}$; $v_{\text{ej}} = 0.2c$) could have been observed by DECam in i and z for $t \lesssim 7$ days; by VST in r for $t \lesssim 5$ days; and by VISTA in J for $t \lesssim 8$ days. The situation is less promising for a NS^2 merger ejecting less mass ($M_{\text{ej}} = 5 \times 10^{-3} M_{\odot}$; $v_{\text{ej}} = 0.2c$), which will be intrinsically dimmer and suffer from less efficient thermalization. To be visible to DECam in i (z) at peak, such a system would need to be closer than ~ 63 (~ 57) Mpc, while VISTA (VST) could only detect it at distances less than ~ 52 (~ 10)

Mpc.

This analysis highlights the importance of seeking optical counterparts at early times, before they fade below detection thresholds. It also suggests that observing strategies should focus on depth, rather than area, to improve the chances of detecting signals that are likely to be faint. Lastly, these findings emphasize the criticality of developing facilities with greater IR sensitivity. *Euclid* (Amendola et al. 2012) and *WFIRST* (Green et al. 2012), each which will have an H-band depth of ~ 25, could detect a typical NS^2 kilonova, located at 100 Mpc, out to $t \sim 15$ days.

Our calculation of time-dependent thermalization efficiencies for kilonovae constrains a key uncertainty in models of r-process transients. Additional work can further improve these models. We have focused on thermalization in the dynamical ejecta from compact object mergers, but the ideas developed here could—and should—be applied to study disk wind outflows, which may produce ejecta poor in Lanthanides and Actinides and potentially contribute a blue/optical component to kilonova light curves. Calculating heating efficiencies for the multiple components believed to make up a kilonova, and incorporating realistic models of $f_{\rm tot}(t)$ in three-dimensional radiation transport simulations of multi-component light curves would yield the best predictions to date of kilonovae's EM signatures.

Chapter 4

A GRB and Broad-lined Type Ic Supernova from a Single Central Engine

This chapter was adapted from a manuscript in preparation for sumbission for publication. It is included with the permission of the coauthors: Paul C. Duffell, Yuqian Liu, Maryam Modjaz, Federica B. Bianco, Daniel Kasen, and Andrew I. MacFadyen.

Unusually high velocities ($\gtrsim 0.1c$) and correspondingly high kinetic energies have been observed in a subset of Type Ic supernovae (so-called "broad-lined Ic" supernovae; SNe Ic-BL), prompting a search for a central engine model capable of generating such energetic explosions. A clue to the explosion mechanism may lie in the fact that all supernovae that accompany long-duration gamma-ray bursts belong to the SN Ic-BL class. Using a combination of two-dimensional relativistic hydrodynamics and radiation transport calculations, we demonstrate that the central engine responsible for long gamma-ray bursts can also trigger a SN Ic-BL. We find that a reasonable gamma-ray burst engine injected into a stripped Wolf-Rayet progenitor produces a relativistic jet with energy $\sim 10^{51}$ ergs, as well as a SN whose synthetic light curves and spectra are fully consistent with observed SNe Ic-BL during the photospheric phase. As a result of the jet's asymmetric energy injection, the SN spectrum and light curves depend on viewing angle. The impact of viewing angle on the spectrum is particularly pronounced at early times, while the viewing angle dependence for the light curves (~ 10 % variation in bolometric luminosity) persists throughout the photospheric phase.

4.1 Introduction

The discovery of the supernova (SN) 1998bw (Galama et al. 1998) in apparent conjunction with the long-duration gamma ray burst (GRB) 980425 suggested a connection between long GRBs and SNe. The relationship was more firmly established with the detection of SN 2003dh rising out of the afterglow of GRB 030329 (Stanek et al. 2003; Hjorth et al. 2003), and has since been cemented by additional observations of SNe coincident with long GRBs.

Notably, every SN linked to a GRB has been classified as a broad-lined SN Ic (Ic-BL; e.g., Woosley & Bloom 2006; Modjaz 2011; Cano et al. 2017a), a category of SNe whose broad spectral features indicate high photospheric velocities ($> 20,000$ km s^{-1}; Modjaz et al. 2016). The kinetic energies ascribed to these SNe are also high ($\sim 10^{52}$ ergs), though they depend on the model used to compute the SN explosion parameters (e.g., Mazzali et al. 2017).

The search for an engine powerful enough to explain SNe Ic-BL energetics is one facet of an investigation into the explosion mechanism for core-collapse supernovae (CCSNe) more generally. In the traditional core-collapse theory, neutrino irradiation from the newborn neutron star revives the stalled shock launched at core bounce, and explodes the star (Colgate & White 1966; Bethe & Wilson 1985). SNe Ic-BL complicate this picture, since even in the most optimistic simulations, the power supplied by neutrinos is insufficient to explain the high kinetic energies of these extreme SNe.

The link between SNe Ic-BL and long GRBs identified jets as a potential alternative source of explosive kinetic energy. However the association of GRBs with SNe only of the Ic-BL class raises the question of whether jets, if they do indeed serve as engines, operate only in unusually energetic SNe, or are far more common events that could power a broad range of supernova explosions depending on the engine parameters and the nature of the progenitor star (Sobacchi et al. 2017a,b; Piran et al. 2017). Understanding the role of jets in extremely energetic explosions is an important step toward understanding the diversity (or lack of diversity) of CCSNe explosion mechanisms.

While all GRB-SNe are Ic-BLs, SNe Ic-BL have also been observed without coincident GRBs. Some SNe Ic-BL must accompany GRBs that point away from the line of sight, and thus go undetected, but it is not clear what fraction of SNe Ic-BL without observed GRBs are explained by orientation effects. In particular, radio follow-up of some GRB-absent SNe Ic-BL found no evidence of highly relativistic material (Berger et al. 2002; Soderberg et al. 2006b; Corsi et al. 2016), suggesting that these SNe do not harbor off-axis GRBs.

A statistical analysis of SNe Ic-BL spectra (Modjaz et al. 2016) revealed that GRB-SNe have systematically broader features than those SNe Ic-BL for which no GRB was detected. There are three likely explanations for this trend.

The first is that SNe Ic-BL occur with *and* without coincident GRBs, but the GRB jet, when present, increases the kinetic energy of the ejecta, resulting in higher photospheric velocities and broader spectral features. If this interpretation is correct, many SNe Ic-BL without an observed coincident GRB truly are solo explosions (though some will host GRBs that go unobserved because they point away from the line of sight). In this case, the lower energies and narrower features of GRB-absent SNe Ic-BL observed by Modjaz et al. (2016) can be attributed to the fact that many of these SNe lack an energy-boosting GRB.

The second explanation is that the correlation between GRBs and high SN velocities is due to an as-yet undetermined third factor that produces both highly kinetic supernovae and relativistic jets. For example, it has been argued that rapidly rotating progenitors (e.g. Wheeler et al. 2002; Uzdensky & MacFadyen 2006; Burrows et al. 2007) may allow the formation of both GRBs and high-velocity SNe.

A third possibility is that the jet induces an asymmetric explosion. In this case, the SN spectrum and photometry depend on viewing angle, and some of the distinction between the spectra of SNe Ic-BL with and without observed GRBs is due to line-of-sight effects. Specifically, the anisotropic energy injection from the jet engine could accelerate ejecta on or near the jet axis to higher velocities than material located at lower lattitudes. An observer looking down the barrel of the jet would see broader lines—and would infer a faster photosphere and a higher kinetic energy—than an observer viewing the system from an off-axis vantage (e.g., Tanaka et al. 2007).

Aspherical explosions have long been invoked to explain some puzzling features of SNe Ic-BL photometry. Höflich et al. (1999) argued that a supernova with an oblate ejecta, if observed from a near-polar viewing angle, would appear to be more luminous than it truly was. They suggested that SN 1998bw, the canonical Ic-BL, did not have the unusually massive ejecta and high ^{56}Ni content and kinetic energy suggested by 1D models, but in fact fell within the range of normal Type Ic SNe. The authors speculated that an oblate ejecta could also produce broader spectral lines in the polar direction than the equatorial direction, but did not carry out radiation transport calculations to verify the theory.

Nakamura et al. (2001) and, more recently, Dessart et al. (2017) found that one-dimensional models are insufficient to explain the typical time evolution of Ic-BL photometry. The photospheric-phase light curves seem to require lower ejecta and ^{56}Ni masses and higher kinetic energies, while models of the late-time luminosity favor more a massive ejecta, lower amounts of ^{56}Ni, and lower kinetic energies. The schemes contrived to satisfy both the early- and late-time photometric constraints (e.g., the suggestion by Maeda et al. (2003) that the distribution of ^{56}Ni in the Ic-BL ejecta is bimodal, with a high-velocity component powering the rapid rise, and a low-velocity, high-density component sustaining the light curve at late times) are implausible for a spherically symmetric ejecta, but, as both authors suggest, may be accommodated by aspherical explosions.

The question of asymmetry in SNe Ic-BL is especially vital given the on-going debate as to the central engine of these explosions. Thompson et al. (2004) outlined how energy extracted from short-lived magnetars produced by a supernova could modify the supernova shock dynamics, resulting in a hyper-energetic explosion. The apparent clustering of the kinetic energies of observed SNe Ic-BL near the maximum rotational energy of a neutron star ($\sim 10^{52}$ ergs) led Mazzali et al. (2014) to suggest that magnetars are the kinetic energy sources of SNe Ic-BL, though there is open debate about how well a magnetar hypothesis explains the photometric properties of individual SNe Ic-BL (see, e.g., Wang et al. 2017; Cano et al. 2017b).

MacFadyen & Woosley (1999) propose an alternate scenario in which the SN ejecta is blown off a disk accreting onto the black hole produced by core collapse. It has also been argued that the SN is driven by a jet engine, which also launches a GRB (Maeda & Nomoto 2003; Sobacchi et al. 2017b; Piran et al. 2017).

Central engine models, especially the magnetar model, are often evaluated based on their ability to produce explosions with kinetic energies close to the (presumed) canonical Ic-BL value 10^{52} ergs. However, kinetic energies inferred from observations depend on parametrized 1D explosion models, which are not guaranteed to accurately map to explosions with significant asymmetry. Fully relativistic hydrodynamical calculations of the explosion evolution, along with multi-dimensional radiation transport simulations of the resulting ejecta, can help resolve the question of Ic-BL energetics, and facilitate the development of more reliable tools for diagnosing supernova energies. This may lay the foundation for a more rigorous assessment of various engine models.

This paper will explore these questions in the context of a single, jet-driven explosion model. We will evaluate the effect of a GRB jet engine on a progenitor star, absent any other source of explosive energy, and demonstrate that such an engine, as it tunnels through the progenitor, can transfer sufficient energy to the surrounding stellar material to unbind it, naturally producing a supernova with a high kinetic energy. Additional energy escapes through the tunnel drilled in the star, and is observed as an ultrarelativistic GRB jet.

We perform a two-dimensional special relativistic hydrodynamic (SRHD) calculation, making it possible to predict asymmetries in the ejecta. We find both the ejecta density profile and distribution of ^{56}Ni are aspherical. Two-dimensional radiation transport calculations allow us to track the effect of these asymmetries on the SN light curves and spectra. This is the first study to carry out an end-to-end (hydrodynamics and radiation) simulation of a jet-driven energetic SN in multiple dimensions.

The numerical tools used to simulate the hydrodynamics and radiation transport of the jet-SN system are outlined in § 4.2. We define our engine and stellar progenitor models in § 4.3. The resultant outflow is described in § 4.4. The synthetic light curves and spectra of the SN, including viewing-angle dependence, are presented and § 4.5.

4.2 Numerical Methods

We use a suite of advanced numerical tools to model the hydrodynamics and radiation of the jet-SN system, and to analyze the emergent spectra and light curves. This suite allows us to study multidimensional supernova dynamics at a level of accuracy and efficiency ordinarily unavailable beyond 1D.

Hydrodynamics: Hydrodynamical calculations are carried out using the JET code (Duffell & MacFadyen 2013), an efficient and accurate solver for the equations of relativistic fluid dynamics. JET employs a "moving mesh" technique (Duffell & MacFadyen 2011), which makes it effectively Lagrangian in the radial dimension, while accurately evolving multidimensional flows, especially flows which move radially outward. Among other advantages, the moving mesh makes it straightforward to evolve flows over large dynamic ranges.

We use JET to inject energy and momentum into the progenitor star, following the method outlined in Duffell & MacFadyen (2015), and assuming axisymmetry. This method, employed previously by Duffell & MacFadyen (2015) and Duffell et al. (2015) results in a robust evolution of the hydrodynamics, as the source terms are smooth functions which can be well-resolved, and the method does not require any special boundary conditions. The engine injects into the core (on length scales $\sim 10^8$ cm) highly relativistic material with an energy-to-mass ratio of 10^3.

The subsequent hydrodynamical evolution of the fluid is followed for the full duration of the jet engine and proceeds until the flow becomes homologous (i.e., the gas coasts on ballistic trajectories with $\mathbf{v}(\mathbf{r}, t) = \mathbf{r}/t$).

In actuality, the flow becomes homologous in stages, with the ultra-relativistic GRB jet reaching homology later than lower-velocity material. However, the supernova ejecta is only mildly relativistic ($v \lesssim 0.2c$), and radiation transport calculations of the supernova will be unaffected by any late-time non-homology in the GRB jet. We conclude the hydrodynamic phase when material with $v \lesssim 0.9c$ has reached homology, at which point the material comprising the supernova ejecta can safely be assumed to be homologous.

This generally occurs at $t \sim$ few hours in physical time or, equivalently, an expansion to $\sim 10^3$ times the initial radius of the progenitor star. Throughout the hydrodynamic phase, the material is relativistically hot and extremely optically thick, so the dynamical effects of radiation are fully contained in the choice of adiabatic index.

The hydrodynamic calculation is used to determine the mass density profile of the ejecta and to approximate the synthesis of radioactive ^{56}Ni. Our model does not include a detailed nuclear reaction network, so we estimate the production of ^{56}Ni with a simple temperature condition. Any zone in which the temperature exceeds 5×10^9 K is assumed to burn to pure ^{56}Ni. The ^{56}Ni mass fraction is advected along with the flow, allowing synthesized ^{56}Ni to spread through the ejecta. The synthesis and subsequent decay of ^{56}Ni release energy, but the energy is negligible compared to the thermal and kinetic energies of the fluid during the hydrodynamical phase. We therefore assume that nuclear energy release is not important for the hydrodynamical evolution of the system. (The decay of ^{56}Ni is the source of luminosity for the supernova, and radioactive energy *is* included in the radiation transport stage of the calculation.)

Radiation Transport: We perform radiation transport with SEDONA (Kasen et al. 2006), a time-dependent multi-wavelength, multi-dimensional Monte Carlo radiation transport code that has been used extensively to model radioactively-powered transients, in particular SNe. Radiation transport is performed on a two-dimensional axisymmetric grid constructed from the low-velocity region of the ejecta structure output by JET. We take as the boundaries of the grid $v_s = |v_z| = 0.2c$. We found that extending the grid to higher velocities had no appreciable effect on the results of the radiation transport.

SEDONA evolves the density and temperature of the ejecta, and accounts for radioactive heating by the decay of ^{56}Ni and ^{56}Co, and cooling by expansion. The ionization and excitation states in the ejecta are determined assuming local thermodynamic equilibrium (LTE), and detailed wavelength-dependent opacities are calculated from the atomic line lists of Kurucz & Bell (1995a,b). Line opacity is assumed to be completely absorptive. SEDONA synthesizes a full spectral time series, from which we construct the emergent light curves and spectra of the supernova.

Spectral Analysis: We analyze our synthetic spectra using state-of-the-art tools developed for the most statistically rigorous study of observed GRB-SNe to date. We compare our synthetic spectra to the average spectra of SNe Ic-BL computed by Modjaz et al. (2016) at different phases, allowing us to test the agreement of the model with the full diversity of SNe Ic-BL, rather than simply comparing to individual objects. The velocities implied by the model spectra are determined with template-fitting methods (see Modjaz et al. 2016, Appendix A) that have been used extensively to characterize the spectra of observed SNe Ic-BL. We also perform spectral analysis with the Supernova Identification code (SNID; Blondin & Tonry 2007), using a full library of SNID spectral templates supplied in part by Liu & Modjaz (2014); Modjaz et al. (2016); Liu et al. (2016b,a). SNID allows us to determine statistically the spectroscopic category that best describes our model, and to find observed supernovae that best match the synthetic model spectra.

4.3 Progenitor and Engine Models

Stellar Progenitor Model: SNe Ibc are generally assumed to be the explosions of stripped-envelope Wolf-Rayet (WR) stars, or of stars in binary systems whose masses are lower than expected for WR stars. (However, whether the WR progenitor scenario can explain SNe Ic-BL is a topic of active research; see Dessart et al. (2017) for a full discussion.) In this work, we use an analytic progenitor model that reasonably approximates the major features of a WR star. Future work will use detailed WR progenitor models evolved with the stellar evolution software MESA (Paxton et al. 2015).

We assume that the innermost regions of the progenitor collapse to a compact object. We therefore remove from the computational grid material interior to $r_{\rm cav} = 1.5 \times 10^{-3} R_\odot \approx 1000$ km. The mass of the excised material is $\sim 1.4 M_\odot$. For numerical tractability, the density in the cavity region is set to 10^{-3} times the density at the cavity boundary.

The material at $r > r_{\rm cav}$ is assumed to be unaffected by the collapse, and thus to maintain the pre-collapse stellar density profile. The density of this material, $\rho_{\rm init}$, is a function of radius only,

$$\rho_{\rm init}(r) = \frac{0.0615 M_0}{R_0^3} (R_0/r)^{2.65} (1 - r/R_0)^{3.5}. \tag{4.1}$$

Above, $R_0 = 1.6 R_\odot$ is the radius to which the stellar atmosphere extends, and $M_0 = 2.5 M_\odot$ sets the mass of the material outside the cavity. Including the mass of the central remnant ($\sim 1.4 M_\odot$), our model suggests a pre-collapse stellar mass of $\lesssim 4 M_\odot$.

The analytic progenitor model is shown in Figure 4.1. For comparison, we also show the density profile, for $r > r_{\rm cav}$, of a WR star evolved with MESA, which we have scaled so that the mass exterior to $r_{\rm cav}$ totals 2.5 $M_\odot$, as in our model. While actual WR stars will not follow these simple scaling laws, the qualitative features of the density profile outside the Fe core are unlikely to change dramatically with stellar mass, and the core collapse, in our calculation, is imposed *a priori*, rather than generated self-consistently, and so is insensitive to assumptions about the core density structure. One disadvantage of this approach is that it

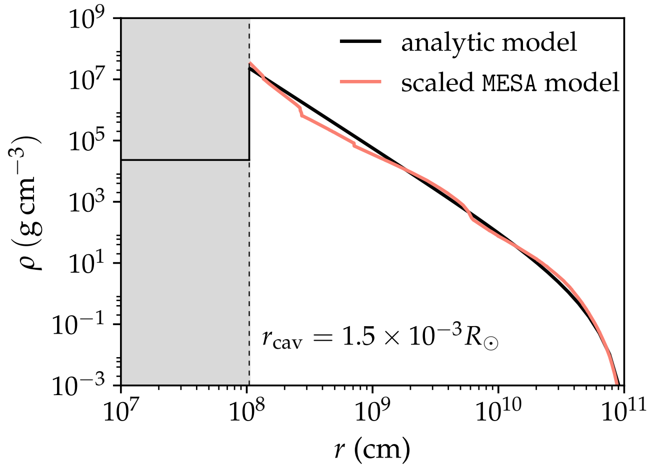

Figure 4.1: The analytic density profile of the progenitor star after core collapse (solid black curve). We assume the collapse of the core leaves behind a cavity of radial extent $r_{\rm cav}$. The density in this region is set to a low, constant value. For comparison, we also plot the scaled density profile, for $r > r_{\rm cav}$, of a stripped-envelope star evolved with MESA (red curve). The analytic model captures the major qualitative features of the MESA result.

does not rigorously determine the density in the innermost regions where most of the ^{56}Ni is synthesized. This introduces an additional uncertainty into our estimate of ^{56}Ni production, which is discussed further in § 4.4 .

Table 4.1 presents the composition, as mass fractions, of the progenitor star. Oxygen dominates, as might be expected for a stripped-envelope Carbon-Oxygen star. The ejecta composition, modulo ^{56}Ni, is taken to be spatially uniform; in zones containing ^{56}Ni, the composition is scaled to accommodate the ^{56}Ni content, while preserving the relative mass fractions of all non-radioactive species. Future work will use more realistic compositions that better reflect compositional inhomogeneities found in detailed studies of evolved stars and core-collapse SNe progenitors (e.g., Arnett & Meakin 2011; Couch et al. 2015; Chatzopoulos et al. 2016).

Jet Engine Model: The GRB engine model is defined by the total energy injected, $E_{\rm eng}$; the engine half-opening angle, $\theta_{\rm eng}$; and the characteristic timescale of the engine, $t_{\rm eng}$. While $t_{\rm eng}$ is often assumed to be greater than or equal to the burst duration, we find in § 4.4 that a short engine can produce a GRB of duration $\tau_{\rm GRB} > t_{\rm eng}$. Rather than cutting the jet luminosity off instantaneously, we allow it to decay exponentially over the timescale $t_{\rm eng}$,

$$L_{\rm eng}(t) = \frac{E_{\rm eng}}{t_{\rm eng}} \times \exp[-t/t_{\rm eng}]. \tag{4.2}$$

The engine is symmetric about the equatorial plane, so $E_{\rm eng}$ is the sum of the energy injected along the positive and negative z-axis.

Table 4.1: Model Summary

Progenitor Parameters			*Engine Parameters*		
M_{tot}[a]	M_{CR}	$M(r > r_{\mathrm{cav}})$[b]	E_{eng}	t_{eng}[c]	θ_{eng}[d]
$3.9 M_\odot$	$1.4 M_\odot$	$2.5 M_\odot$	1.8×10^{52} erg	1.1 s11.5°	
		Progenitor Composition			
He: 6.79e-3	C: 2.27e-2	N: 2.91e-5	O: 9.05e-1	Ne: 1.37e-2	Mg: 8.46e-3
Si: 2.69e-2	S: 1.04e-2	Ar: 1.60e-3	Ca: 6.63e-4	Ti: 5.11e-7	Fe: 3.50e-3

[a] The mass of the evolved progenitor star just prior to core collapse.

[b] The mass remaining after the core has been excised.

[c] This relatively short-duration engine generates a GRB of longer duration. See Section 4.4 and Table 4.2 for details.

[d] The eventual opening angle of the GRB jet is narrower than θ_{eng} (see Table 4.2), due to recollimation processes that act on the jet as it tunnels through the star.

We focus on one engine model with $E_{\mathrm{eng}} = 1.8 \times 10^{52}$ ergs, $\theta_{\mathrm{eng}} = 11.5°$, and $t_{\mathrm{eng}} = 1.1$ s. (Note that the engine duration and opening angle are different from the GRB duration and the opening angle of the GRB jet, as discussed below.) These parameters were found to produce a SN and a GRB roughly consistent with observations; future work will more fully explore the dependence of the GRB and SN on the engine parameters.

4.4 Gas Dynamics

The jet propagation and ^{56}Ni production are illustrated in Figure 4.2. The engine injects energy into the center of the star, creating a hot, high-pressure region that tunnels along the z-axis toward the surface of the progenitor, which is marked by a dashed white line in the top two panels.

As the head of the jet burrows outward, the energy from the engine is redistributed throughout the star. Recollimation shocks confine the most relativistic material to a narrow region near the z-axis (see Panel 1), and shocks emanating from the hot, high-pressure region surrounding the z-axis push against the cold stellar material off-axis, accelerating it to high, but non-relativistic, velocities (Panel 2). As the engine heats the stellar material to temperatures exceeding 5×10^9 K, ^{56}Ni is synthesized. The highest temperatures occur near the center of the star. The ^{56}Ni forged at small radii is then entrained by the relativistic flow propagating along the pole and deposited in a narrow cone about the z-axis.

The relatively short duration of the engine (1.1 s) allows our model to produce a fairly high amount of ^{56}Ni (0.24 $M_\odot$). The energy scale of the engine is constrained by the observed kinetic energies of SNe Ic-BL. A shorter engine injects this energy in a concentrated burst,

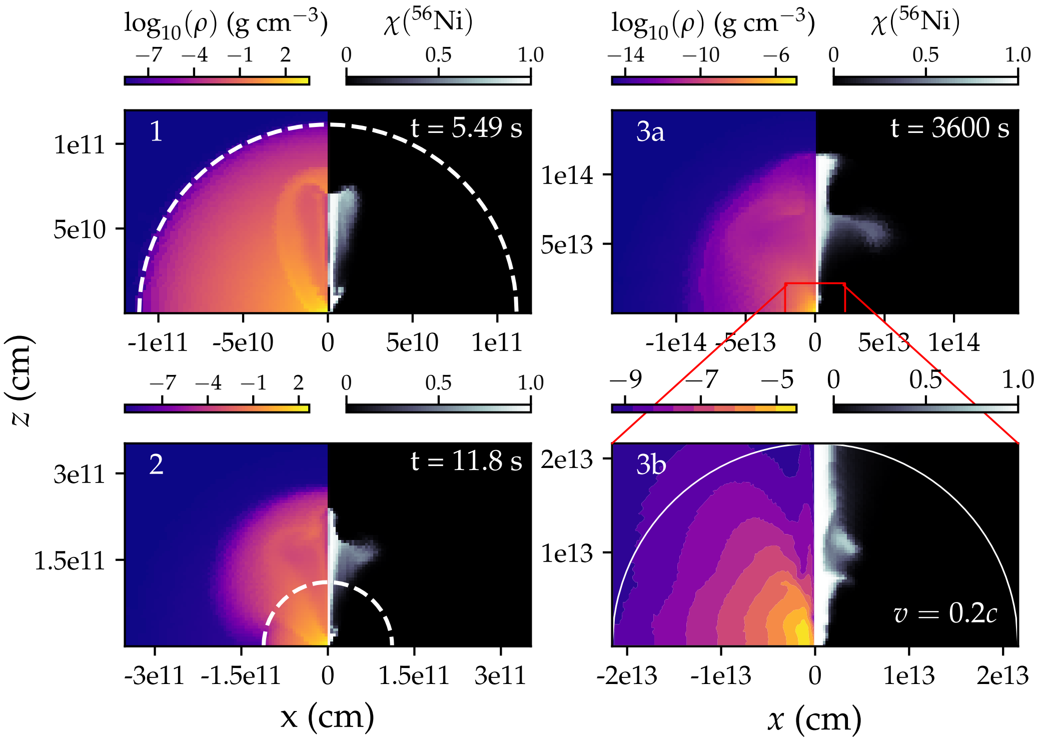

Figure 4.2: The gas dynamics of the jet. The left (right) side of each panel shows mass density (^{56}Ni mass fraction). The pre-explosion progenitor radius is plotted in Panels 1 and 2 as a dashed white line. The engine burrows through the progenitor (Panel 1), disrupts it, and eventually breaks out (Panel 2). Energy is transferred to off-axis material by lateral shocks. In Panel 3a, the system is homologous. The most relativistic material has erupted as a GRB jet, but much of the matter reached lower velocities (a few $\times\, 0.1c$), forming the supernova explosion. We perform our radiation transport calculations on material inside the red box of Panel 3a, which is defined by v_s, $|v_z| \leq 0.2c$. Panel 3b zooms in on this region, and shows density contours to emphasize the ejecta geometry. The white line in Panel 3b shows $v = 0.2c$.

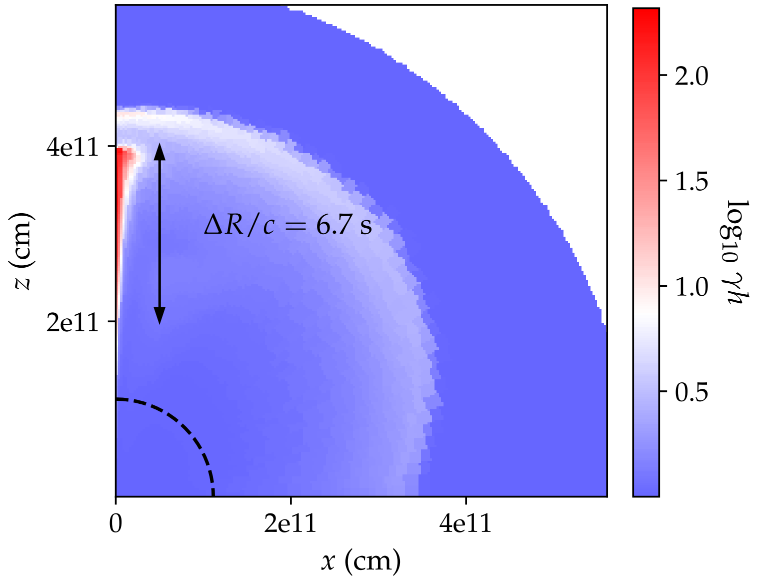

Figure 4.3: The terminal Lorentz factor, γh of the material, at $t = 17.3$ s. At this time, the jet has broken out of the star (the initial stellar radius is plotted as a black dashed line) and the spatial scale of material with high γh is no longer evolving. The extent of material with $\gamma h \gtrsim 10$ suggests a GRB duration of $\lesssim 7$ s, a factor of > 5 greater than $t_{\rm eng}$. The flow does not attain Lorentz factors quite as large as shown above at late times (the peak late-time Lorentz factor is 72) because the most relativistic parts of the flow are eventually decelerated by internal collisions.

and drives up temperatures deep in the interior of the star before these inner layers can react to the energy injection and expand to lower densities. In our model, the densities in the zones that satisfy $T_{\rm max} \geq 5 \times 10^9$ K are high enough that a non-negligible amount of ^{56}Ni is synthesized, though the exact amount will be sensitive to the densities at very small radii, and will depend on the progenitor structure and the physics of the core collapse. Models with longer-lived jets may have difficulty synthesizing similar quantities of ^{56}Ni; for example, the jets of Chen et al. (2017) have a duration of ~ 20 s, but produce only $0.05 M_\odot$ of ^{56}Ni.

The importance of high engine luminosities/short engine timescales for significant ($\gtrsim 0.1 M_\odot$) ^{56}Ni production was pointed out by Maeda & Nomoto (2003). Here, we demonstrate that a short-duration engine can also produce an extended relativistic stream consistent with a long-duration GRB. Figure 4.3 shows γh, the local Lorentz factor multiplied by the specific enthalpy of the fluid. We have scaled h by c^{-2} to convert it to a dimensionless quantity. The product γh is fixed for an expanding fluid element. The dimensionless h approaches 1 as the flow evolves, so the Lorentz factor γ asymptotes to the initial value of γh. The timescale for prompt γ-ray emission is set by the width of the relativistic (high γh) jet, which is fixed soon after the jet escapes the star. If all the relativistic material were shocked instantly, an observer would detect a pulse lasting $\tau_{\rm GRB} = \Delta R/c$, where ΔR is the jet's radial thickness.

It is generally assumed that $\Delta R = ct_{\rm eng}$, based on the idea that the engine emits over its duration a stream of relativistic material moving at c. However, this picture does not take into account the process of the jet pushing its way through the stellar envelope, or the effects of the high-pressure cocoon supporting the jet. At the point of breakout, the engine has created a stream of relativistic material extending from the engine to surface of the star, a distance $\Delta R = R_0 = 1.1 \times 10^{11}$ cm. This stream flows through a low density tunnel drilled by the jet head as it propagates through the star. The tunnel sits inside a cocoon whose pressure, just before the jet head emerges from the star, is in rough equipartition with the jet's kinetic energy density. After jet breakout, this pressure is converted into kinetic energy, increasing the size of the relativistic stream. Once the cocoon pressure has dropped, the evolution of the stream ends. At this point, the relativistic stream has $\Delta R \approx 2 \times 10^{11}$ cm, corresponding to a GRB of duration $\tau_{\rm GRB} \approx 6.7$ s. Figure 4.3 shows the radial width of the relativistic material explicitly.

By the time homology is achieved (about an hour after the engine is initiated), the system has formed two distinct high-energy components. The first is a highly relativistic GRB jet, which can be seen at the outer edge of the ejecta in Panels 2 and 3a of Figure 4.2. The GRB jet produced for our choice of engine and progenitor has a half-opening angle of 2.9° after breaking out of the star, an estimated duration of $\lesssim 7$ seconds, and peak (average) Lorentz factor of 72 (40). (Figure 4.3 shows γh values somewhat higher than this peak. This is because internal collisions eventually decelerate the most relativistic components of the flow; see Duffell & MacFadyen 2015). Recollimation shocks confine the highly-relativistic material in a narrow column; as a result, the GRB jet has an opening angle narrower than that of the engine. The jet and counter-jet each have $\sim 2 \times 10^{51}$ ergs of kinetic energy, or roughly 10% of the total engine energy.

The second component is a fairly isotropic SN explosion dominated by lower-velocity ($v \lesssim 0.2c$) material, which is demarcated by a red box in Panel 3a and detailed in Panel 3b. The SN ejecta has a mass of 1.9 $M_\odot$ and a kinetic energy of 7.4×10^{51} ergs. (Some of the engine energy is spent accelerating material that is not part of the GRB jet and has densities too low and velocities too high to contribute to the supernova ejecta, so the energy in the GRB jets and the SN sum to less than $E_{\rm eng}$.) The properties of the GRB and SN are summarized in Table 4.2.

The SN ejecta is shown in detail in Panel 3b. There is a pronounced highly prolate component surrounding the z-axis, and a more mildly prolate component at larger length scales, but overall the deviations from isotropy are minor. The distribution of ^{56}Ni, which is concentrated along the jet axis, exhibits far more anisotropy, though we note that jet instabilities not captured in 2D might alter the distribution of ^{56}Ni further, possibly affecting the supernova. Our model produces $0.24 M_\odot$ of ^{56}Ni, though ^{56}Ni production depends sensitively on the parameters of the engine (see above), a theme that will be explored in future work.

Table 4.2: SN and GRB Properties

GRB Properties		
τ_{GRB}[a]	E_{jet}	$\theta_{\mathrm{jet},1/2}$
6.7 s	2×10^{51} ergs	2.9°
SN Properties		
t_{rise}	L_{peak}	$M(^{56}\mathrm{Ni})$
17.5 days	6×10^{42} erg s^{-1}	$0.24 M_{\odot}$

[a] GRB duration is estimated as described in § 4.4

4.5 Supernova Observables

We perform two-dimensional radiation transport calculations on the supernova ejecta using the time-dependent multi-wavelength transport code SEDONA (Kasen et al. 2006). To assess the effects of viewing angle, we calculate light curves and spectra for seven evenly-spaced bins in $\mu = \cos\theta$, $\mu \in [-1, 1]$. The spectra and light curves shown here are averages within the bins.

4.5.1 Bolometric Light Curves

Figure 4.4 shows the bolometric luminosity of our model supernova for a range of viewing angles. (Due to the symmetry about the equatorial plane, resolving the emission into seven bins in μ produces only four distinct light curves, and only four are presented.) For comparison, we also plot bolometric light curves for three SNe Ic-BL: 1998bw, which accompanied GRB 980425 (Galama et al. 1998); 2006aj, which was coincident with GRB 060218B (Mirabal et al. 2006; Campana et al. 2006; Modjaz et al. 2006; Pian et al. 2006; Soderberg et al. 2006a; Sollerman et al. 2006); and 2002ap, which had no observed GRB and no indications of any relativistic outflow (Berger et al. 2002). These pseudobolometric light curves were constructed by Prentice et al. (2016), based on data from references therein.

The synthetic light curves reach a peak bolometric luminosity of $\sim 6 \times 10^{42}$ ergs s^{-1} at $t = 17.5$ days. This is slightly lower than the average peak luminosity of SNe Ic-BL reported by Prentice et al. (2016) ($\log L_{\mathrm{peak}} = 43 \pm 0.21$), but as shown in Figure 4.4, still falls well within the range of observed Ic-BL light curves. The width and general shape of the light curves are also consistent with observations. However, our model has a longer rise time than many observed SNe Ic-BL. The SNe we show in Figure 4.4 rise to peak at ~ 15 days (1998bw), ~ 9 days (2006aj), and ~ 12 days (2002ap), and the rise times of SNe Ic-BL calculated by Prentice et al. (2016) average to 12.7 ± 2.2 days.[1] A different choice of engine

---

[1] We calculate a weighted average of the values of "t_{p} from $t_{-1/2}$" (their Table 7) for SNe identified in their Table 1 as Type Ic-BL or GRB-SNe, for which such a value was given.

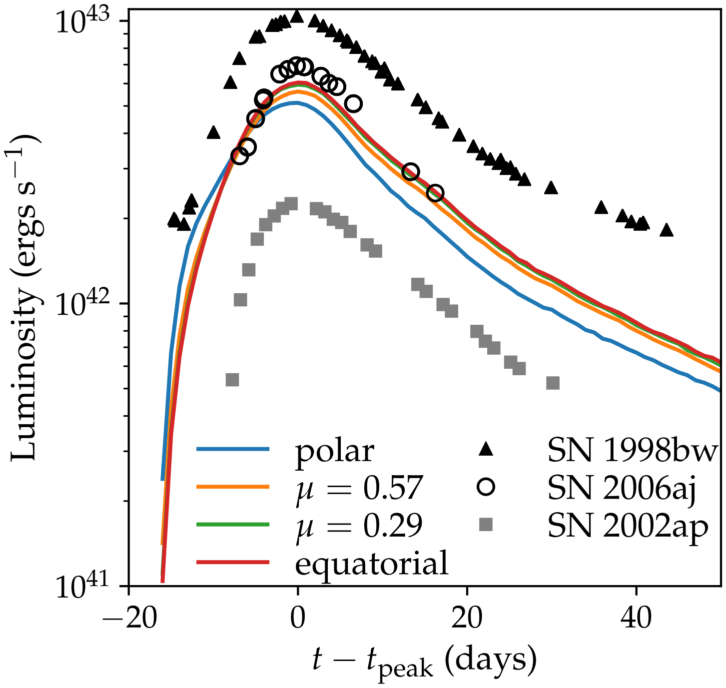

Figure 4.4: Bolometric light curves of the model, for a range of viewing angles, compared to reconstructed bolometric light curves for three SNe Ic-BL from Prentice et al. (2016). The peak luminosities and widths of the model light curves are consistent with observations, though our model has a longer rise time than most observed SNe Ic-BL. The effect of viewing angle is modest, with observers near the pole seeing luminosities $\lesssim 10\%$ lower than viewers along the equator.

and/or progenitor may resolve the rise time discrepancy. A full parameter space study is planned to investigate the effects of engine and progenitor properties on SN observables.

Surprisingly, orientation has little effect on either rise time or luminosity. The anisotropic distribution of ^{56}Ni does not produce a strong viewing-angle dependence for the observed luminosity because the majority of the ^{56}Ni resides deep in the interior of the ejecta. (In our model $\sim 88\%$ of the ^{56}Ni mass is located at velocities less than $0.05c$.) The small amount of ^{56}Ni at higher velocities imparts to the polar light curve a slightly higher luminosity at very early times ($t \lesssim 5$ days), but has a negligible effect on the light curve otherwise.

The energy radiated by the bulk of the ^{56}Ni must be reprocessed by the intervening material before it passes through the photosphere and escapes the ejecta. The mild viewing-angle dependence our model exhibits is produced not bu the distribution of ^{56}Ni, but by the structure of the photosphere. As suggested by the density profile shown in Panel 3b of Figure 4.2, the photosphere is mildly prolate. The projected area of the photosphere is larger for an observer near the equator than for one close to the pole, and as a result an observer on the equator sees a slightly higher luminosity.

4.5.2 Spectra

The time evolution of the supernova spectrum is shown in Figure 4.5 for polar (blue curves) and equatorial (red curves) viewing angles. In all figures, the spectra are plotted as normalized flux per Å, F_λ.

Both viewing angles produce spectra whose flux at early times is concentrated at wavelengths 3500 Å$\lesssim \lambda \lesssim$ 5500 Å. As time progresses, the flux is redistributed redward and emission for $\lambda \lesssim$ 5000 Å becomes less pronounced.

For phases greater than 10 days, the spectra exhibit excess flux at 8500 Å, associated with an emission line of CaII. This is due to the assumption of LTE in the radiation transport calculation, which is known to over-estimate the ionization fraction of Ca (Kasen 2006).

The effect of viewing angle is more obvious for the spectra than for the light curves. The differences are particularly pronounced prior to bolometric peak. At phases -10 and -5 days, the spectra for the polar viewing angle show broader and bluer features than the equatorial spectra, especially at UV/blue wavelengths (3000 Å $\leq \lambda \leq$ 5000 Å). This reflects the asphericity of the photosphere, which forms at a slightly higher velocity along the poles than near the equator.

For $t > t_{\rm rise}$, the flux at UV wavelengths is suppressed for the polar spectra relative to the equatorial spectra, which have more prominent features in the range 4000 Å $\lesssim \lambda \lesssim$ 5000 Å, and are bluer overall. These discrepancies are due to the presence of explosively-synthesized ^{56}Ni/Co/Fe along the pole, which has numerous strong bound-bound transitions in the UV and increases the line opacity.

In order to identify the characteristic velocity scales of the model and compare them with those of observed SNe Ic-BL, we measured for the polar spectrum at maximum light the velocity of the Fe II triplet (i.e., Fe II $\lambda\lambda\lambda$ 4924, 5018, 5169 Å) using the methods and code described in Modjaz et al. (2016), which were also used to analyze the largest dataset to date of observed SNe Ic-BL with and without GRBs. These template-fitting and broadening procedures properly account for the line-blending that occurs at the observed high velocities of SNe Ic-BL.

We find that the Fe feature complex is blueshifted by $v_{\rm blue} = -18,900^{+4,200}_{-4,100}$ km s^{-1}. We also calculate the "convolution velocity," $v_{\rm conv}$, which represents the full width at half maximum (FWHM) of the Gaussian kernel that, when convolved with the narrow-lined SN Ic template, reproduces the width of the SN Ic-BL Fe II feature. For our model, $v_{\rm conv} = 15,000^{+7,500}_{-14,800}$ km s^{-1}. For comparison, the spectra of observed SNe Ic-BL (with and without GRBS) have an average $v_{\rm blue}$ of $-21,000 \pm 8,200$ km s^{-1} (at maximum light), and a median $v_{\rm conv}$ of $\sim 8,000 - 9{,}000$ km s^{-1} (over all phases).

Thus, the model spectra are in good agreement with observed spectra, though we note that the error bars for the model's $v_{\rm conv}$ are quite large, reflecting some tension in the fitting algorithm. The source of this tension is the shape of the Fe II feature. In normal SNe Ic, the triplet appears as a double trough with a pronounced bump in the center. In SNe Ic-BL, the central bump is often washed out by strong line blending (see Appendix A of Modjaz et al. 2016). In our model, the "W" shape of the triplet is suppressed, but the total width of the

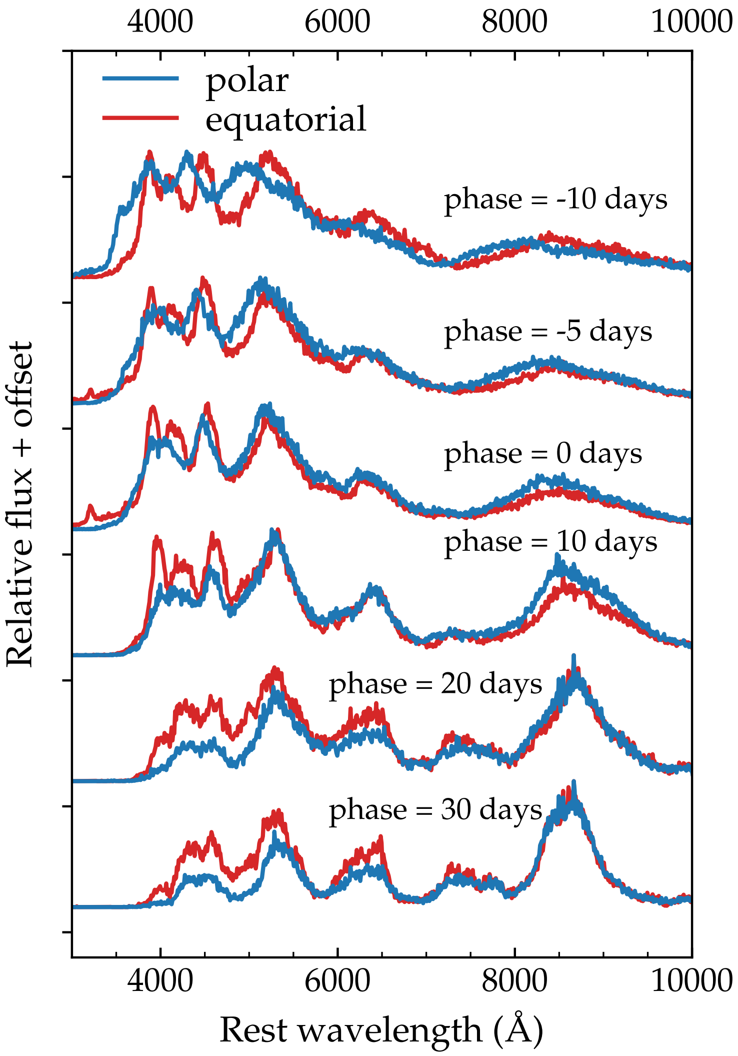

Figure 4.5: The time-evolution of the spectra from our model supernova for polar (blue curves) and equatorial (red curves) viewing angles. Phases are relative to maximum light.

blended feature is lower than for a typical SN Ic-BL. The fitting scheme favors higher $v_{\rm conv}$ to broaden away the central bump, but requires lower values to better capture the overall width, resulting in large uncertainties. Overall, however, the best-fit values of $v_{\rm blue}$ and $v_{\rm conv}$ are consistent, within error bars, with those of observed SNe Ic-BL.

Figures 4.6 and 4.7 compare our model's (polar) spectrum to data, and further demonstrate the commonalities between the model and observed SNe Ic-BL. In Figure 4.6, we present the spectrum of the model at peak and ten days after peak, alongside spectra of observed SNe Ic-BL, both with and without coincident GRBs, at comparable phases. Figure 4.7 shows the time evolution of the polar model spectrum, with the continuum removed, relative to the average flattened spectra for SNe Ic-BL with associated GRBs calculated by Modjaz et al. (2016). The continuum subtraction of the model was carried out using the same data-driven procedure applied to observed spectra. (See Modjaz et al. 2016 and Liu et al. 2016b for details.) To concentrate on the comparison of the spectral line features of our model with those of the statistical data set of SNe Ic-BL with associated GRBs, we have scaled the average spectra. We also analyze the synthetic polar spectrum using SNID. References for spectra in Figure 4.6 are given in Table 4.3.

Table 4.3: Summary of Comparison Spectra

SN	*Classification*	*References*[a]
1998bw	Ic-BL, with GRB	G98, P01
2002ap	Ic-BL, w/o GRB	SNID[b] (G02, F03), M14
2003dh	Ic-BL, with GRB	S03, M03, K03, K04, D05
2006aj	Ic-BL, with GRB	M06, P06, M14
2013cq	Ic-BL, with GRB	X13

[a] References: G98— Galama et al. (1998); P01 — Patat et al. (2001); G02 — Gal-Yam et al. (2002); F03 — Foley et al. (2003); M14 — Modjaz et al. (2014); S03 — Stanek et al. (2003); M03 — Matheson et al. (2003); K03 — Kawabata et al. (2003); K04 — Kosugi et al. (2004); D05 — Deng et al. (2005); M06 — Modjaz et al. (2006); P06 — Pian et al. (2006); X13 — Xu et al. (2013);

[b] SNID — in SNID release version 5.0 with templates-2.0 by Blondin & Tonry (2007), with original references in parenthesis

The model successfully reproduces the major characteristics of Ic-BL spectra, which result from the blending of highly Doppler-broadened line profiles. The similarity of the model spectra to observations and to mean spectra can be seen in Figures 4.6 and 4.7. SNID also classified the model spectra as belonging to the Ic-BL class, though the individual spectra SNID matched to the model at different phases, summarized in Table 4.4, tended to be GRB-absent SNe Ic-BL, which Modjaz et al. (2016) showed to have systematically narrower lines than GRB-SNe. However, Figure 4.7 shows that the line widths of the model are generally comparable to the mean spectra of SNe Ic-BL with associated GRBs, so the interpretation of the SNID matches is not straightforward. What is clear is that the model

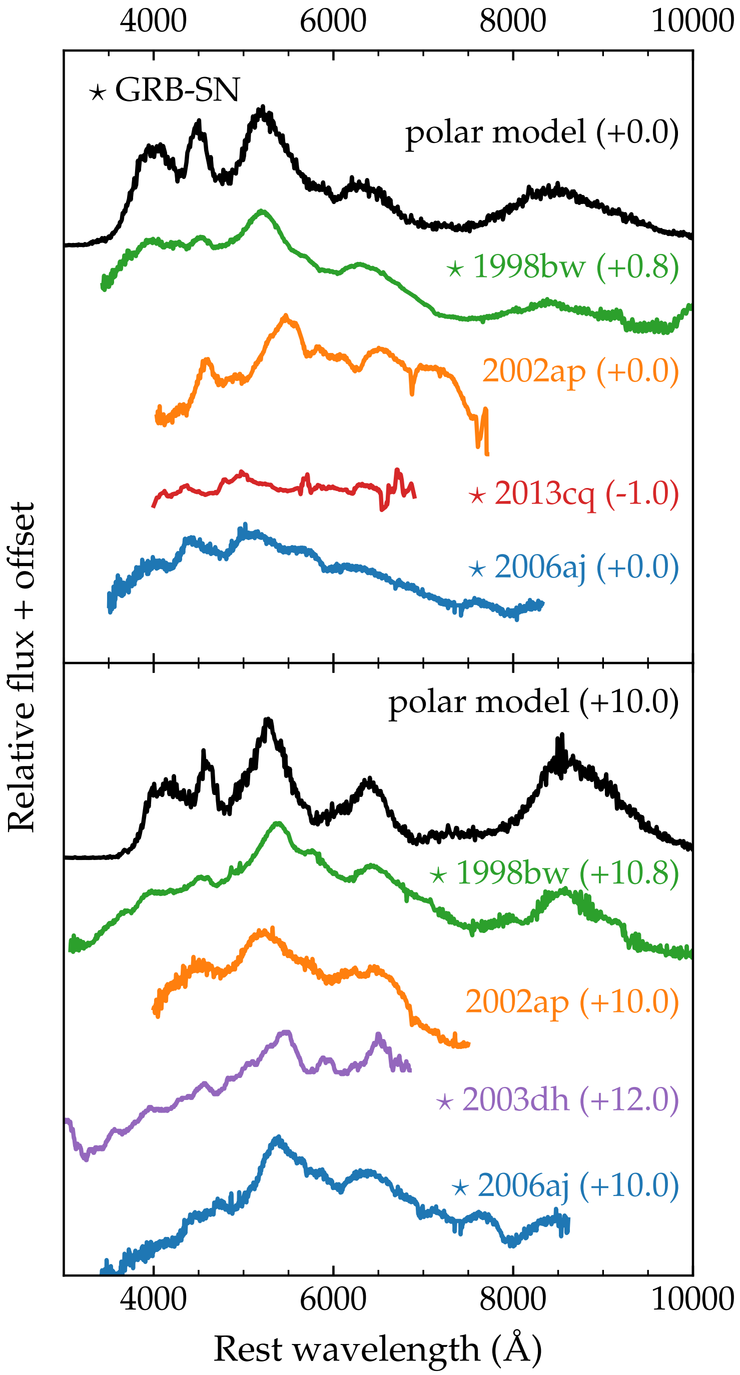

Figure 4.6: The spectrum of our model (seen pole-on) at peak and ten days after peak, compared to observed SNe Ic-BL at similar phases. SNe with a confirmed corresponding GRB are marked with a star. Our model has line widths comparable to SNe classified as Ic-BL, though it is bluer than some of the observed SNe, and has more prominent features in the UV.

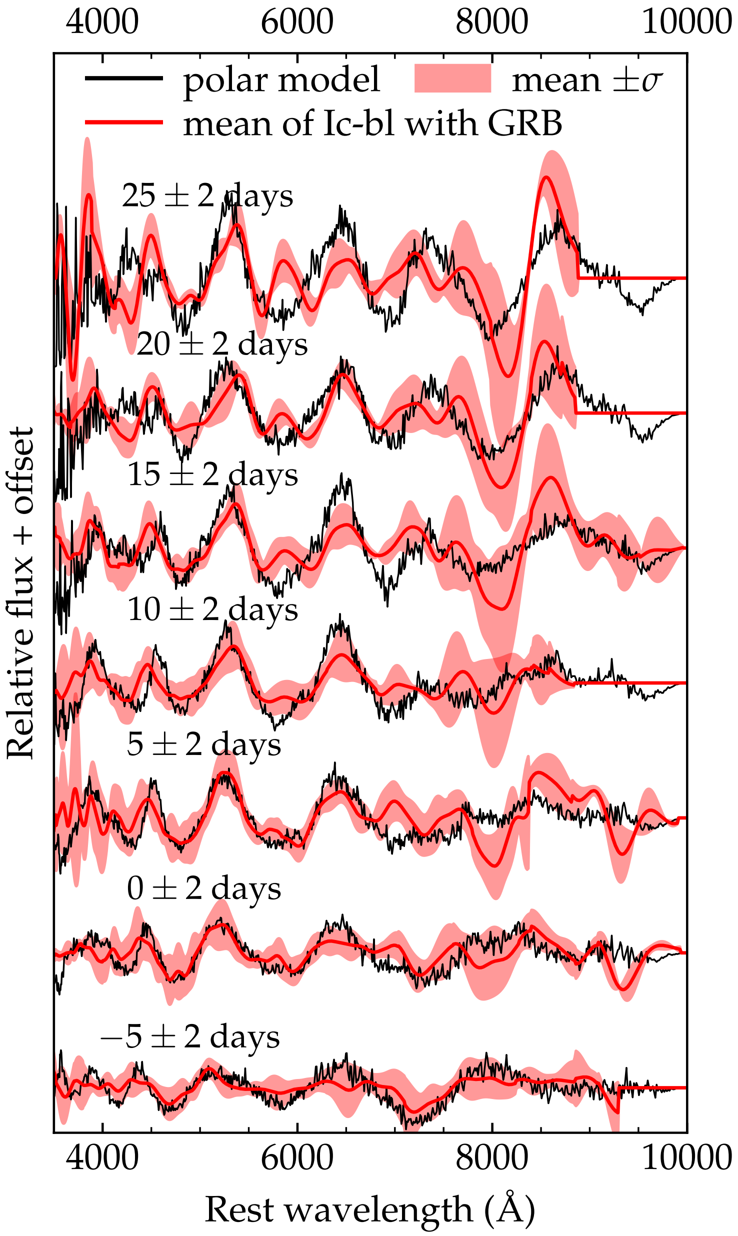

Figure 4.7: The polar model spectrum at multiple phases compared to average spectra of SNe Ic-BL with a coincident GRB, as calculated by Modjaz et al. (2016). All spectra are continuum-subtracted using the methods of Modjaz et al. (2016) and Liu et al. (2016b). The averages are plotted as red curves, and the light red bands show the region within one standard deviation of the mean. Our model generated spectra with stronger features than the average spectra, so we scaled average spectra and the standard deviations by a factor of 3 to allow an easier comparison of the widths of the absorption features in the two cases.

belongs unambiguously to the Ic-BL category based on its broad lines and strong line-blending.

Table 4.4: Best-match spectra from SNID

Polar model	**SNID match**		
Phase	*SN*	*Phase*	*Classification*
-5 days	2007ru	−3 days	Ic-BL, w/o GRB
+0 days	PTFgzk	−1 day	Ic-BL w/o GRB
+0 days	2012bz	+1 days	Ic-BL with GRB
+10 days	2007I	> 10 days[a]	Ic-BL w/o GRB

[a] SN 2007I has no confirmed light-curve peak, so the phase of that supernova's spectrum is not precisely known.

As shown in Figures 4.6, the model spectra are bluer than most of the observed SNe. The strengths of individual spectral features are also not always well captured. In particular, the model exhibits prominent spikes in the blue and UV that are mostly absent from observed SNe. Narrow Fe features at these wavelengths were also present in the spectra of Dessart et al. (2017), who carried out a systematic survey of one-dimension Ic-BL models using the 1D non-LTE transport code CMFGEN (Hillier & Dessart 2012). In particular, their model r6e4BH, which has an ejecta mass and energy close to our model's, appears at phase 8.3 days to be similarly spiky for $\lambda \lesssim 5000$ Å (their Figure 3).

The over-pronounced blue and UV features are also apparent when comparing to average Ic-BL spectra. While the model and the mean spectra have absorption features of similar width, the model's features are much stronger than the means'; the averages (red lines) and standard deviations (light red bands) in Figure 4.7 were scaled by a factor of 3. This suggests that the energetics of the model are roughly correct, but the composition, which we have not rigorously investigated here, may need to be adjusted to improve agreement with observation. For example, incorporating a more realistic spatially-dependent composition could improve the situation.

4.6 Discussion and Conclusion

We have used sophisticated numerical SRHD calculations, radiation transport, and data analysis techniques to investigate the possibility that a GRB engine, absent any additional energy source, can produce both a narrow, highly relativistic jet and a more isotropic supernova explosion with the spectral characteristics typical of GRB-SNe. This study provides an end-to-end description of a jet-driven core-collapse event.

We have shown that a GRB engine injected into a stripped-envelope star not only produces a long-duration GRB, it can also transfer enough energy to the stellar material to unbind it, resulting in a supernova explosion. The engine also heats a portion of the ejected material to high enough temperatures that the synthesis of ^{56}Ni is favored by nuclear statistical equilibrium.

Our fiducial GRB engine and progenitor models trigger a SN typical of SNe Ic-BL. The SN's bolometric light curves have luminosities and shapes that are generally consistent with observed SNe Ic-BL. The model spectra have the broad absorption features that underpin the Ic-BL classification. We considered only a single engine-progenitor pair for this study. However, a broader parameter survey is planned for the future, and it may identify systems that better match average SNe Ic-BL properties, or that mimic individual unusual Ic-BL events (e.g. 1998bw).

We have also explored the effect of asymmetry on the Ic-BL observables. Our model creates a mildly asymmetric ejecta that imparts a slight viewing-angle dependence to the light curves, and a moderate dependence to the spectra. At very early times, spectral features observed along the pole are broadened and blue-shifted relative to spectra observed from an equatorial vantage. However, this difference fades with time, and it is not clear whether an observer located on-axis would infer a meaningfully higher photospheric velocity or kinetic energy than an observer near the equator.

We have established that a single engine can produce the observed properties of both a long GRB and highly kinetic SN. However, much remains to be done. Future work (in prep.) will explore in more detail the effects of progenitor models and engine parameters on both the relativistic jet and the supernova produced, and delineate how the the production of ^{56}Ni, the kinetic energy of the explosion, the degree of asphericity in the ejecta, and the breadth of the lines depend on these parameters. We will also extend our calculations to late times to see whether the aspherical ejecta geometries produced in jet-driven explosions can self-consistently explain both the early- and late-time spectra and light curves of SNe Ic-BL.

Bibliography

Abadie, J., Abbott, B. P., Abbott, R., et al. 2010, Phys. Rev. D, 82, 102001

Abbott, B. P., Abbott, R., Abbott, T. D., et al. 2016a, Physical Review Letters, 116, 241103

—. 2016b, ArXiv e-prints, arXiv:1602.08492 [astro-ph.HE]

—. 2016c, Physical Review Letters, 116, 061102

Amendola, L., Appleby, S., Bacon, D., et al. 2012, ArXiv e-prints, arXiv:1206.1225 [astro-ph.CO]

Arnett, W. D. 1979, ApJ, 230, L37

—. 1982, ApJ, 253, 785

Arnett, W. D., & Meakin, C. 2011, ApJ, 733, 78

Arnould, M., Goriely, S., & Takahashi, K. 2007, Phys. Rep., 450, 97

Audi, G., Wang, M., Wapstra, A., et al. 2012, Chinese Physics C, 36, 1287

Badnell, N. R. 2011, Computer Phys. Commun., 182, 1528

Barnes, J., & Kasen, D. 2013, ApJ, 775, 18

Barnes, J., Kasen, D., Wu, M.-R., & Martínez-Pinedo, G. 2016, ApJ, 829, 110

Baron, E., Hauschildt, P. H., Nugent, P., & Branch, D. 1996, MNRAS, 283, 297

Bauswein, A., Goriely, S., & Janka, H.-T. 2013, ApJ, 773, 78

Bauswein, A., Stergioulas, N., & Janka, H.-T. 2015, ArXiv e-prints, arXiv:1503.08769 [astro-ph.SR]

Berger, E., Fong, W., & Chornock, R. 2013, ApJ, 774, L23

Berger, E., Kulkarni, S. R., & Chevalier, R. A. 2002, ApJ, 577, L5

Berger, M., Coursey, J., Zucker, M., & Chang, J. 2005, ESTAR, PSTAR, and ASTAR: Computer Programs for Calculating Stopping-Power and Range Tables for Electrons, Protons, and Helium Ions (version 1.2.3), [Online] Available: http://physics.nist.gov/Star, [13-Feb-2015] National Institute of Standards and Technology, Gaithersburg, MD.

Berger, M., Hubbell, J., Seltzer, S., et al. 2010, XCOM: Photon Cross Section Database (version 1.5), [Online] Available: http://physics.nist.gov/xcom, [02-Oct-2014] National Institute of Standards and Technology, Gaithersburg, MD.

Berger, M. J., & Seltzer, S. M. 1964, NASA Special Publication, 3012

Bethe, H. A., & Wilson, J. R. 1985, ApJ, 295, 14

Biémont, E., Palmeri, P., & Quinet, P. 1999, Ap&SS, 269, 635

Blondin, S., & Tonry, J. L. 2007, ApJ, 666, 1024

Bloom, J. S., Holz, D. E., Hughes, S. A., et al. 2009, ArXiv e-prints, arXiv:0902.1527 [astro-

ph.CO]
Blumenthal, G. R., & Gould, R. J. 1970, Reviews of Modern Physics, 42, 237
Burrows, A., Dessart, L., Livne, E., Ott, C. D., & Murphy, J. 2007, ApJ, 664, 416
Campana, S., Mangano, V., Blustin, A. J., et al. 2006, Nature, 442, 1008
Cano, Z., Wang, S.-Q., Dai, Z.-G., & Wu, X.-F. 2017a, Advances in Astronomy, 2017, 8929054
Cano, Z., Izzo, L., de Ugarte Postigo, A., et al. 2017b, ArXiv e-prints, arXiv:1704.05401 [astro-ph.HE]
Chan, K.-W., & Lingenfelter, R. E. 1993, ApJ, 405, 614
Chatzopoulos, E., Couch, S. M., Arnett, W. D., & Timmes, F. X. 2016, ApJ, 822, 61
Chen, K.-J., Moriya, T. J., Woosley, S., et al. 2017, ApJ, 839, 85
Chevalier, R. A., & Soker, N. 1989, ApJ, 341, 867
Colgate, S. A., & White, R. H. 1966, ApJ, 143, 626
Corsi, A., Gal-Yam, A., Kulkarni, S. R., et al. 2016, ApJ, 830, 42
Couch, S. M., Chatzopoulos, E., Arnett, W. D., & Timmes, F. X. 2015, ApJ, 808, L21
Dalal, N., Holz, D. E., Hughes, S. A., & Jain, B. 2006, Phys. Rev. D, 74, 063006
Darbha, S., Metzger, B. D., Quataert, E., et al. 2010, MNRAS, 409, 846
Deng, J., Tominaga, N., Mazzali, P. A., Maeda, K., & Nomoto, K. 2005, ApJ, 624, 898
Dessart, L., Hillier, D. J., Yoon, S.-C., Waldman, R., & Livne, E. 2017, ArXiv e-prints, arXiv:1703.08932 [astro-ph.SR]
Duffell, P. C., & MacFadyen, A. I. 2011, ApJS, 197, 15
—. 2013, ApJ, 775, 87
—. 2015, ApJ, 806, 205
Duffell, P. C., Quataert, E., & MacFadyen, A. I. 2015, ApJ, 813, 64
Duflo, J., & Zuker, A. P. 1995, Phys. Rev. C, 52, R23
Eastman, R. G., & Pinto, P. A. 1993, ApJ, 412, 731
Eichler, D., Livio, M., Piran, T., & Schramm, D. N. 1989a, Nature, 340, 126
—. 1989b, Nature, 340, 126
Eichler, M., Arcones, A., Kelic, A., et al. 2015, ApJ, 808, 30
Fernández, R., Kasen, D., Metzger, B. D., & Quataert, E. 2015, MNRAS, 446, 750
Fernández, R., & Metzger, B. D. 2013, MNRAS, 435, 502
Foley, R. J., Papenkova, M. S., Swift, B. J., et al. 2003, PASP, 115, 1220
Freiburghaus, C., Rosswog, S., & Thielemann, F.-K. 1999, ApJ, 525, L121
Friend, D. B., & Castor, J. I. 1983, ApJ, 272, 259
Gal-Yam, A., Ofek, E. O., & Shemmer, O. 2002, MNRAS, 332, L73
Galama, T. J., Vreeswijk, P. M., van Paradijs, J., et al. 1998, Nature, 395, 670
Goriely, S., Bauswein, A., & Janka, H.-T. 2011, ApJ, 738, L32
Goriely, S., Bauswein, A., Janka, H.-T., et al. 2014, in American Institute of Physics Conference Series, Vol. 1594, American Institute of Physics Conference Series, ed. S. Jeong, N. Imai, H. Miyatake, & T. Kajino, 357
Goriely, S., Bauswein, A., Just, O., Pllumbi, E., & Janka, H.-T. 2015, "MNRAS", 452, 3894
Goriely, S., Chamel, N., & Pearson, J. M. 2010, Phys. Rev. C, 82, 035804

Goriely, S., Demetriou, P., Janka, H.-T., Pearson, J. M., & Samyn, M. 2005, Nuclear Physics A, 758, 587

Gould, R. J. 1975, ApJ, 196, 689

Green, J., Schechter, P., Baltay, C., et al. 2012, ArXiv e-prints, arXiv:1208.4012 [astro-ph.IM]

Grossman, D., Korobkin, O., Rosswog, S., & Piran, T. 2014, MNRAS, 439, 757

Harry, I. W., & Fairhurst, S. 2011, Phys. Rev. D, 83, 084002

Heiter, U., Barklem, P., Fossati, L., et al. 2008, Journal of Physics Conference Series, 130, 012011

Heitler, W. 1954, Quantum theory of radiation

Hillier, D. J., & Dessart, L. 2012, MNRAS, 424, 252

Hjorth, J., Sollerman, J., Møller, P., et al. 2003, Nature, 423, 847

Hoeflich, P., Mueller, E., & Khokhlov, A. 1993, A&A, 268, 570

Höflich, P., Wheeler, J. C., & Wang, L. 1999, ApJ, 521, 179

Holz, D. E., & Hughes, S. A. 2005, ApJ, 629, 15

Hotokezaka, K., Kiuchi, K., Kyutoku, K., et al. 2013a, Phys. Rev. D, 87, 024001

—. 2013b, Phys. Rev. D, 87, 024001

Hotokezaka, K., & Piran, T. 2015, MNRAS, 450, 1430

Hotokezaka, K., Wanajo, S., Tanaka, M., et al. 2016, MNRAS, 459, 35

Huba, J. D. 2013, NRL Plasma Formulary (Palm Springs, CA: Wexford College Press)

Hulse, R. A., & Taylor, J. H. 1975, ApJ, 195, L51

Jack, D., Hauschildt, P. H., & Baron, E. 2011, A&A, 528, A141

Jackson, J. D. 1999, Classical electrodynamics, 3rd edn. (John Wiley & Sons, Inc.)

Janka, H.-T., Eberl, T., Ruffert, M., & Fryer, C. L. 1999, ApJ, 527, L39

Just, O., Bauswein, A., Ardevol Pulpillo, R., Goriely, S., & Janka, H.-T. 2015, ArXiv e-prints, arXiv:1504.05448 [astro-ph.SR]

Karp, A. H., Lasher, G., Chan, K. L., & Salpeter, E. E. 1977, ApJ, 214, 161

Kasen, D. 2006, ApJ, 649, 939

Kasen, D., Badnell, N. R., & Barnes, J. 2013, ApJ, 774, 25

Kasen, D., Fernández, R., & Metzger, B. D. 2015, MNRAS, 450, 1777

Kasen, D., Thomas, R. C., & Nugent, P. 2006, ApJ, 651, 366

Kasliwal, M. M., & Nissanke, S. 2014, ApJ, 789, L5

Kawabata, K. S., Deng, J., Wang, L., et al. 2003, ApJ, 593, L19

Kim, C., Perera, B. B. P., & McLaughlin, M. A. 2015, MNRAS, 448, 928

Kiuchi, K., Cerdá-Durán, P., Kyutoku, K., Sekiguchi, Y., & Shibata, M. 2015, Phys. Rev. D, 92, 124034

Kiuchi, K., Kyutoku, K., Sekiguchi, Y., Shibata, M., & Wada, T. 2014, Phys. Rev. D, 90, 041502

Kochanek, C. S., & Piran, T. 1993, ApJ, 417, L17

Korobkin, O., Rosswog, S., Arcones, A., & Winteler, C. 2012, MNRAS, 426, 1940

Kosugi, G., Mizumoto, Y., Kawai, N., et al. 2004, PASJ, 56, 61

Kurucz, R., & Bell, B. 1995a, Atomic Line Data (R.L. Kurucz and B. Bell) Kurucz CD-ROM No. 23. Cambridge, Mass.: Smithsonian Astrophysical Observatory, 1995., 23

Kurucz, R. L., & Bell, B. 1995b, Atomic line list

Kyutoku, K., Ioka, K., Okawa, H., Shibata, M., & Taniguchi, K. 2015, Phys. Rev. D, 92, 044028

Lattimer, J. M., & Schramm, D. N. 1974, ApJ, 192, L145

—. 1976, ApJ, 210, 549

Law, N. M., Kulkarni, S. R., Dekany, R. G., et al. 2009, PASP, 121, 1395

Lee, W. H. 2001, MNRAS, 328, 583

Li, L.-X., & Paczyński, B. 1998, ApJ, 507, L59

Lippuner, J., & Roberts, L. F. 2015, ApJ, 815, 82

Liu, M., Wang, N., Deng, Y., & Wu, X. 2011, Phys. Rev. C, 84, 014333

Liu, Y., & Modjaz, M. 2014, ArXiv e-prints, arXiv:1405.1437 [astro-ph.SR]

Liu, Y.-Q., Modjaz, M., & Bianco, F. B. 2016a, ArXiv e-prints, arXiv:1612.07321 [astro-ph.HE]

Liu, Y.-Q., Modjaz, M., Bianco, F. B., & Graur, O. 2016b, ApJ, 827, 90

LSST Science Collaborations. 2009, arXiv:0912.0201

Lucy, L. B. 2005, A&A, 429, 19

MacFadyen, A. I., & Woosley, S. E. 1999, ApJ, 524, 262

Maeda, K., Mazzali, P. A., Deng, J., et al. 2003, ApJ, 593, 931

Maeda, K., Mazzali, P. A., & Nomoto, K. 2006, ApJ, 645, 1331

Maeda, K., & Nomoto, K. 2003, Nuclear Physics A, 718, 167

Matheson, T., Garnavich, P. M., Stanek, K. Z., et al. 2003, ApJ, 599, 394

Mazzali, P. A., McFadyen, A. I., Woosley, S. E., Pian, E., & Tanaka, M. 2014, MNRAS, 443, 67

Mazzali, P. A., Sauer, D. N., Pian, E., et al. 2017, MNRAS, 469, 2498

Mendoza-Temis, J. d. J., Wu, M.-R., Langanke, K., et al. 2015, Phys. Rev. C, 92, 055805

Metzger, B. D., Bauswein, A., Goriely, S., & Kasen, D. 2015, MNRAS, 446, 1115

Metzger, B. D., & Berger, E. 2012, ApJ, 746, 48

Metzger, B. D., Piro, A. L., & Quataert, E. 2008, MNRAS, 390, 781

Metzger, B. D., Martínez-Pinedo, G., Darbha, S., et al. 2010, MNRAS, 406, 2650

Meyer, B. S., Mathews, G. J., Howard, W. M., Woosley, S. E., & Hoffman, R. D. 1992, ApJ, 399, 656

Milne, P. A., The, L.-S., & Leising, M. D. 1999, ApJS, 124, 503

Mirabal, N., Halpern, J. P., An, D., Thorstensen, J. R., & Terndrup, D. M. 2006, ApJ, 643, L99

Modjaz, M. 2011, Astronomische Nachrichten, 332, 434

Modjaz, M., Liu, Y. Q., Bianco, F. B., & Graur, O. 2016, ApJ, 832, 108

Modjaz, M., Stanek, K. Z., Garnavich, P. M., et al. 2006, ApJ, 645, L21

Modjaz, M., Blondin, S., Kirshner, R. P., et al. 2014, AJ, 147, 99

Möller, P., Nix, J. R., Myers, W. D., & Swiatecki, W. J. 1995, Atom.Data Nucl.Data Tabl., 59, 185

Nakamura, T., Mazzali, P. A., Nomoto, K., & Iwamoto, K. 2001, ApJ, 550, 991

Nakar, E., & Piran, T. 2011, Nature, 478, 82

Narayan, R., Paczynski, B., & Piran, T. 1992, ApJ, 395, L83
Nissanke, S., Holz, D. E., Dalal, N., et al. 2013a, ArXiv e-prints, arXiv:1307.2638 [astro-ph.CO]
Nissanke, S., Kasliwal, M., & Georgieva, A. 2013b, ApJ, 767, 124
Oechslin, R., Janka, H.-T., & Marek, A. 2007, A&A, 467, 395
Paczynski, B. 1986, ApJ, 308, L43
Palmeri, P., Quinet, P., Wyart, J.-F., & Biémont, E. 2000, Phys. Scr, 61, 323
Pannarale, F., & Ohme, F. 2014, ApJ, 791, L7
Patat, F., Cappellaro, E., Danziger, J., et al. 2001, ApJ, 555, 900
Paxton, B., Marchant, P., Schwab, J., et al. 2015, ApJS, 220, 15
Perego, A., Rosswog, S., Cabezón, R. M., et al. 2014, MNRAS, 443, 3134
Peters, P. C., & Mathews, J. 1963, Phys. Rev., 131, 435
Pian, E., Mazzali, P. A., Masetti, N., et al. 2006, Nature, 442, 1011
Pinto, P. A., & Eastman, R. G. 2000, ApJ, 530, 757
Piran, T., Korobkin, O., & Rosswog, S. 2014, ArXiv e-prints, arXiv:1401.2166 [astro-ph.HE]
Piran, T., Nakar, E., Mazzali, P., & Pian, E. 2017, ArXiv e-prints, arXiv:1704.08298 [astro-ph.HE]
Prentice, S. J., Mazzali, P. A., Pian, E., et al. 2016, MNRAS, 458, 2973
Price, D. J., & Rosswog, S. 2006, Science, 312, 719
Pritychenko, B., Běták, E., Kellett, M. A., Singh, B., & Totans, J. 2011, Nuclear Instruments and Methods in Physics Research A, 640, 213
Quinet, P., & Biémont, E. 2004, At. Data Nucl. Data Tables, 87, 635
Roberts, L. F., Kasen, D., Lee, W. H., & Ramirez-Ruiz, E. 2011, ApJ, 736, L21
Rosswog, S. 2005, ApJ, 634, 1202
Rosswog, S., Davies, M. B., Thielemann, F.-K., & Piran, T. 2000, A&A, 360, 171
Rosswog, S., Liebendörfer, M., Thielemann, F.-K., et al. 1999, A&A, 341, 499
Rosswog, S., Thielemann, F. K., Davies, M. B., Benz, W., & Piran, T. 1998, in Nuclear Astrophysics, ed. W. Hillebrandt & E. Muller, 103
Rybicki, G. B., & Lightman, A. P. 1986, Radiative Processes in Astrophysics
Schenter, G. K., & Vogel, P. 1983, Nuclear Science and Engineering, 83, 393
Schiwietz, G., & Grande, P. L. 2001, Nuclear Instruments and Methods in Physics Research B, 175, 125
Schutz, B. F. 1986, Nature, 323, 310
Schutz, B. F. 2002, in Lighthouses of the Universe: The Most Luminous Celestial Objects and Their Use for Cosmology, ed. M. Gilfanov, R. Sunyeav, & E. Churazov, 207
Segré, E. 1977, Nuclei and Particles, 2nd edn. (Benjamin-Cummings Pub Co)
Sekiguchi, Y., Kiuchi, K., Kyutoku, K., & Shibata, M. 2015, Phys. Rev. D, 91, 064059
Sekiguchi, Y., Kiuchi, K., Kyutoku, K., Shibata, M., & Taniguchi, K. 2016, ArXiv e-prints, arXiv:1603.01918 [astro-ph.HE]
Seltzer, S. M., & Berger, M. J. 1986, Atomic Data and Nuclear Data Tables, 35, 345
Soares-Santos, M., Kessler, R., Berger, E., et al. 2016, ArXiv e-prints, arXiv:1602.04198
Sobacchi, E., Granot, J., & Bromberg, O. 2017a, ArXiv e-prints, arXiv:1705.00792 [astro-

ph.HE]

Sobacchi, E., Granot, J., Bromberg, O., & Sormani, M. C. 2017b, ArXiv e-prints, arXiv:1705.00281 [astro-ph.HE]

Sobolev, V. V. 1960, Moving envelopes of stars

Soderberg, A., Berger, E., & Schmidt, B. 2006a, IAU Circ., 8674

Soderberg, A. M., Nakar, E., Berger, E., & Kulkarni, S. R. 2006b, ApJ, 638, 930

Sollerman, J., Jaunsen, A. O., Fynbo, J. P. U., et al. 2006, A&A, 454, 503

Stanek, K. Z., Matheson, T., Garnavich, P. M., et al. 2003, ApJ, 591, L17

Stubbs, C. W. 2008, Classical and Quantum Gravity, 25, 184033

Surman, R., McLaughlin, G. C., & Hix, W. R. 2006, ApJ, 643, 1057

Surman, R., McLaughlin, G. C., Ruffert, M., Janka, H.-T., & Hix, W. R. 2008, ApJ, 679, L117

Tanaka, M., & Hotokezaka, K. 2013, ApJ, 775, 113

Tanaka, M., Maeda, K., Mazzali, P. A., & Nomoto, K. 2007, ApJ, 668, L19

Tanvir, N. R., Levan, A. J., Fruchter, A. S., et al. 2013, Nature, 500, 547

Taylor, J. H., Wolszczan, A., Damour, T., & Weisberg, J. M. 1992, Nature, 355, 132

Thompson, T. A., Chang, P., & Quataert, E. 2004, ApJ, 611, 380

Uzdensky, D. A., & MacFadyen, A. I. 2006, ApJ, 647, 1192

Wanajo, S., Sekiguchi, Y., Nishimura, N., et al. 2014, ApJ, 789, L39

Wang, L. J., Yu, H., Liu, L. D., et al. 2017, ApJ, 837, 128

Wang, M., Audi, G., Wapstra, A., et al. 2012, Chinese Physics C, 36, 1603

Weisberg, J. M., & Taylor, J. H. 1981, General Relativity and Gravitation, 13, 1

Weisberg, J. M., & Taylor, J. H. 2005, in Astronomical Society of the Pacific Conference Series, Vol. 328, Binary Radio Pulsars, ed. F. A. Rasio & I. H. Stairs, 25

Wheeler, J. C., Meier, D. L., & Wilson, J. R. 2002, ApJ, 568, 807

Woosley, S. E., & Bloom, J. S. 2006, ARA&A, 44, 507

Woosley, S. E., Wilson, J. R., Mathews, G. J., Hoffman, R. D., & Meyer, B. S. 1994, ApJ, 433, 229

Xu, D., de Ugarte Postigo, A., Leloudas, G., et al. 2013, ApJ, 776, 98

Ziegler, J. F. 1980, The Stopping and Rangles of Ions in Matter, Vol. 5, Handbook of Stopping Cross-Sections for Energetic Ions in All Elements (Pergamon Press)

Appendix A

Transport Methods for Radioactive Decay Products

This appendix describes our numerical method for calculating detailed thermalization efficiencies using a 3-dimensional (3D) particle transport scheme.

A.1 Grid

We carry out our calculation on a 3D Cartesian grid of 100^3 zones. The ejecta is assumed to have a broken power-law density profile and a two-zone composition, as described in §3.2. The grid is initialized at $t = 0.1$ days, and advanced in time every 0.1 days.

In each time step, the grid emits $N_{\rm pack}$ particle packets with co-moving frame (cmf) kinetic energy $E_{\rm pack}$ equal to $E_{\Delta t}(t)/N_{\rm pack}$, where $E_{\Delta t} = M_{\rm ej} \int_{\Delta t} \dot{\epsilon}(t) {\rm d}t$ is the total radioactive energy emitted by the ejecta over the course of the time step. The probability of emission in any zone is proportional to zone mass. Packets are emitted at random positions within the zone, with random initial directions, at a time selected from a flat distribution $[t, t + \Delta t)$. Each packet represents $N_{\rm part}$ particles of energy $E_{\rm part}$, where the particle's initial cmf energy is sampled from the time-dependent spectra of Figure 3.3. Particles are transported through the grid until their cmf energy falls below a threshold energy ~ 1000 times less than the typical energy at emission. At this point, particles deposit their residual kinetic energy and are removed from the grid.

A.2 Gamma rays

Gamma ray packets are propagated through the grid in small steps in typical Monte Carlo fashion (e.g. Lucy 2005; Kasen et al. 2006.) A propagating photon packet can reach the end of the current grid time step, leave the zone it is in, or interact with an atom. The outcome that occurs on the shortest timescale is selected. The timescales for the first two processes are straightforward, and the timescale for interaction is given by

$$\Delta t_{\rm atom} = -\frac{1}{c\rho\kappa_{\rm tot}} \ln(1-z), \tag{A.1}$$

where $\kappa_{\rm tot} = \kappa_{\rm C} + \kappa_{\rm PI}$ is the sum of of Compton and photoionization opacities, ρ is the mass density, and z is a random number sampled from $[0, 1)$. The relative weights of $\kappa_{\rm C}$ and $\kappa_{\rm PI}$ determine whether the γ-ray packet Compton scatters or photoionizes.

During a Compton scatter, a photon undergoes some angular displacement, with the differential cross section and change in energy given by the Klein-Nishina formula. Energy lost by the photon packet is transferred to a non-thermal electron, which also acquires a momentum opposite to that of the post-scatter photon. The electron is then transported through the grid, as described in the next section.

In a photoionization, some of the photon's energy thermalizes promptly, but the rest is transferred to a non-thermal photoelectron. In general, photoelectrons are ejected from the inner shells of the ionized atoms, and acquire energies equal to the γ-ray energy less the photoelectron's binding energy, $E_{\rm B}$. Outer shell atomic electrons cascade down to fill the vacancy created by the ionization, releasing photons whose energies sum to $\sum E = E_{\rm B} - \Delta E_{\rm atom}$, where $\Delta E_{\rm atom}$ is the difference in the atom's total energy before and after the ionization and cascade. The ejected photoelectron will travel through the grid until it thermalizes and recombines with an ambient atom. Since the thermalized electron will attach to the atom's valance shell, the energy released upon recombination will be low, of order $\Delta E_{\rm atom}$.

We assume that all photoelectrons originate from inner shells of heavy elements, so $E_{\rm B} \gg \Delta E_{\rm atom}$. The energy released in the post-ionization cascade is then $E_{\rm B} - E_{\rm atom} \approx E_{\rm B}$. This energy thermalizes immediately. The photoelectron receives the remainder of the γ-ray energy, $E_\gamma - E_{\rm B}$, and a momentum parallel to the initial γ-ray momentum. It is propagated until it dissipates its kinetic energy.

Since the cross section for photoionization peaks at $E_\gamma \sim E_{\rm B}$, we estimate representative binding energies for the r-process composition by locating local maxima in the aggregate photoionization opacity curve. For each photoionization, we select the minimum binding energy such that $E_\gamma^{\rm cmf} > E_B$. If $E_\gamma^{\rm cmf} \gtrsim 0.1$ MeV, and there are no identifiable peaks that satisfy this criterion, we set $E_{\rm B} = 0.9 E_\gamma^{\rm cmf}$.

A.3 Massive particles

Massive particles lose energy continuously, so are not suited to a discrete Monte Carlo treatment. Instead, a massive particle packet is transported through the grid until it reaches the border of its zone, the grid time step ends, or (in the case of disordered fields) the magnetic field changes direction. The change in the particle's cmf energy is calculated from the particle's initial cmf energy, and the zone conditions and elapsed time, both measured in the cmf. The particle energy is then adjusted.

For α-particles and fission fragments, all energy lost is assumed to be thermalized and promptly deposited on the grid. In the case of β-particles, energy loss via Bremsstrahlung can be significant, and a non-negligible fraction of the β-particle energy can be converted to photons of fairly high energies, which will not immediately thermalize. To account for this possibility, we differentiate β-particle energy lost to plasma and ionization/excitation—which we assume thermalizes instantly—from energy lost to Bremsstrahlung, which we assume does not. At the end of each time step, thermalized energy $\Delta E_{\rm th}$ is deposited in the grid, and $E_{\rm part}$ and $E_{\rm pack}$ are adjusted accordingly. The probability that the β-packet is converted to a γ-packet is given by the ratio of the energy lost to Bremsstrahlung during the preceding time step to the particle energy after thermalization: $P_{\beta\rightarrow\gamma} = \Delta E_{\rm Br}/(E^{\rm cmf}_{\beta,{\rm i}} - \Delta E_{\rm th})$, and random number sampling determines the outcome. If the packet remains a β-packet, $E_{\rm part}$ is decremented by $\Delta E_{\rm Br}$, while $E_{\rm pack}$ remains the same (i.e., $N_{\rm pack}$ is updated.) If conversion to a γ-packet is selected, a new direction of propagation is set randomly in the co-moving frame. The cmf energy of the new γ-ray is selected from a flat probability distribution in the range $(0, E^{\rm cmf}_{\beta,{\rm i}} - \Delta E_{\rm th}]$, which approximates the fairly flat Bremsstrahlung spectrum of relativistic β-particles (Jackson 1999). The value of $N_{\rm pack}$ is then adjusted to preserve total post-thermalization packet energy.

A.3.1 Influence of magnetic fields

Charged particles have Larmor radii much smaller than the coherence length of the magnetic field, so we track their motion along field lines without resolving oscillations about the guiding center. The motion of a particle with mass m and kinetic energy E can then be described by the average velocity

$$\langle \mathbf{u} \rangle = v(E)\mu\hat{\mathbf{B}}, \tag{A.2}$$

where v is the total velocity of a particle with kinetic energy E, $\hat{\mathbf{B}}$ is the unit vector directed along $\mathbf{B}$, and μ is the cosine of the angle (the "pitch angle") between the particle's total velocity and the velocity of its guiding center, which is aligned with $\mathbf{B}$. This $\langle \mathbf{u} \rangle$ is the particle velocity we use to boost between the co-moving and center-of-explosion frames, and to update particle position at the end of a time step.

We explore three classes of magnetic fields: radial ($\mathbf{B} \propto \hat{\mathbf{r}}$), toroidal ($\mathbf{B} \propto \hat{\boldsymbol{\phi}}$), and random. For radial and toroidal fields, the magnetic field direction at any location in the ejecta can be determined trivially, and updating the direction of $\langle \mathbf{u} \rangle$ at the end of each time step is straightforward.

For tangled fields, we randomly choose a unique $\hat{\mathbf{B}}$ for each particle upon emission. We assume the field changes on a length scale $\lambda R_{ej}(t)$, where λ is a model parameter, and at the beginning of each time step we calculate the timescale for the particle to experience a significant change in $\hat{\mathbf{B}}$:

$$\Delta t_{\rm B} = \frac{\lambda R_{\rm ej}(t)}{|\langle \mathbf{u} \rangle|} \ln(1 - z), \tag{A.3}$$

where z is a random number between 0 and 1. If Δt_{B} is less than the time for a particle to leave a zone or end the grid time step, the magnetic "scattering" action is selected, the particle position and energy are updated, and a new field direction is chosen at random. The re-orientation preserves energy and the magnitude of the momentum in the cmf. This is reasonable, because these discrete scatters are standing in for smoother and more gradual field gradients. However, it also leads, on average, to energy losses in the center of explosion frame, which decrease thermalization efficiency. This can be thought off as the particles transferring their energy to the bulk kinetic energy of the ejecta, rather than the thermal background. It is a small effect.

The propagation of a particle along field lines depends on total velocity and μ. Particles are emitted on the grid with a random direction defined by the unit vector $\hat{\mathbf{D}}$, so μ is $\hat{\mathbf{D}} \cdot \hat{\mathbf{B}}$. In the case of radial fields, μ evolves to preserve the magnetic adiabatic invariant $(1-\mu^2)/B$. This evolution encourages outward motion. Inward-moving particles encounter ever-stronger fields, and decrease their inward velocity in response, eventually "mirroring" off the field and beginning to travel outward. Particles streaming outward move into weaker magnetic fields, so their pitch angle increases and they stream out even faster.

We include magnetic beaming and mirroring only for radial fields, where changes to the pitch angle facilitate particle escape and can be meaningful for thermalization. Particles in toroidal fields are confined to one region of velocity space; changes in their pitch angle cannot promote outward motion and so cannot affect thermalization. While particles in random fields could experience beaming and mirroring, they may also undergo pitch angle scattering—interactions with small fluctuations in the field that can change pitch angle, and would act to isotropize μ, counter to beaming and mirroring. We assume the two effects balance out, and hold pitch angle constant for particles in random and toroidal fields.

A.3.2 Fission fragment transport

As discussed in §3.2.2, at late times, fission fragments may have Larmor radii comparable to the magnetic field coherence length. This could affect the transport, especially for disordered fields, where field lines in close proximity may have very different orientations. In such a system, the guiding center approximation breaks down, and the motion of the particle must be resolved. We estimate the importance of this effect by modeling fission fragment transport in a tangled field as a random walk of the fragment itself (as opposed to its guiding center). In this simple scheme, fission fragments travel in straight lines and re-orient randomly on length scales of $r_{\mathrm{L}} = r^{\mathrm{ff}}_{\mathrm{L,max}} = 1.0 \times 10^{-2} v_2 t_{\mathrm{d}} R_{\mathrm{ej}}$. This path stands in for the more complicated looping trajectory we would see when $r_{\mathrm{L}} \sim \lambda R_{\mathrm{ej}}$. We carried out a simulation of fission fragment transport in this limit for the fiducial ejecta model, and found only negligible variation in $f_{\mathrm{ff}}(t)$ relative to the flux-tube approximation. The difference was was apparent only at late times, when fission contributes little to the energy generation. We therefore conclude that detailed models of fission fragment transport are unnecessary.